Electron Microscopy Based Characterization of Resistive Switches

Submitted in partial fulfillment of the requirement for
The degree of
Doctoral of Philosophy
in
Materials Science and Engineering

Jonghan Kwon

B.S., Materials Science and Engineering, Korea University
M.S., Materials Science and Engineering, Ohio State University

Carnegie Mellon University
Pittsburgh, PA

September 2016

Abstract

Resistive Random Access Memory (RRAM) has emerged as a leading candidate for non-volatile memory storage. RRAM devices typically consist of a metal/insulator/metal (MIM) structure and exhibit switching of the device resistivity state (low-to-high, high-to-low) by application of electrical bias. It is now widely accepted that shunting and rupturing of local conductive paths (filaments) directly determines the resistance state. The size and composition of these filaments are very much an open question, but are usually attributed to high local concentrations of oxygen vacancies. Although there has been a huge body of research conducted in this field, the fundamental nature of the conductive path and basic switching/failure mechanisms are still under debate. This is largely due to a lack of structural analysis of existing filament size and composition in actual devices. Since the non-volatile nature and device reliability issues (i.e. retention and endurance) are directly related to the irreversible structural transformations in the device, microstructural characterization is essential for eventual commercialization of RRAM. In this study, I investigated oxygen vacancy defect dynamics under electric filed essential for resistive switching and aim to identify size, location, and chemical nature of the conductive filaments in RRAM devices by using a variety of devices and materials characterization methods: *in situ* transmission electron microscopy (TEM), high-resolution TEM (HRTEM), scanning TEM (STEM)-electron energy loss spectroscopy (EELS), electron holography, rapid thermal annealing (RTA), transient thermometry, and electro-thermal simulation.

I adopt an *in situ* electrical biasing TEM technique to study microstructural changes occurring during resistive switching using a model TiO_2-based RRAM device, and confirmed the device is switchable inside of the TEM column. I observed extension and contraction of {011} and {121}-type Wadsley defects, crystallographic shear faults, associated with resistive switching. More specifically, emission and adsorption of oxygen vacancies under different polarity of electrical biases at the fault bounding dislocations were identified. The motion of Wadsley defects was used to track oxygen vacancy migration under electric field. Also, the microstructural changes that occur when the device experiences low electric field (~10^4 V/cm) was reported, akin to *read disturb.*

Crossbar type RRAM device stacks consisting of TiN/a-$HfAlO_x$/Hf/TiN were investigated to estimate filament size, filament temperature, and its chemical footprint using HRTEM, transient thermometry and numerical simulation. In each of the switched devices, a single crystallite ~ 8-16 nm in size embedded in an amorphous $HfAlO_x$ matrix was found. The $HfAlO_x$ crystallization temperature (T_c) of 850 K was determined by combining RTA and HRTEM imaging. In parallel, the filament size has been determined by transient thermometry. The temperature profile extracted from these measurements suggested that the peak filament temperature was > 1500 K at the center, with the hot zone ($T > T_c = 850$ K) extending to a radius of 7 nm around the filament. These results were consistent with the HRTEM observations of the crystallite size. The potential filament location (crystallite) in the switching devices was analyzed by STEM-EELS and identification of the filament chemical nature identification has been attempted.

Acknowledgements

First of all, I would like to thank my advisors, Prof. Marek Skowronski and Prof. Yoosuf Picard for their guidance and support throughout my Ph.D. They have kept encouraging me to step forward at a time with invaluable advices and great care. Their work ethics and attitudes toward research have always inspired me, and enable me to get through all the hard works and become an independent scientist. It was a great honor that I have them as my Ph.D. advisors and it was unforgettable experience to work with them at Carnegie Mellon University.

There are many peoples who helped me for last several years. I thank all my Ph.D. committee members, Prof. James Bain, Prof. Laughlin, and Prof. Davis for their insightful comments and feedbacks in the course of completing my dissertation. Thanks to Tom Nuhfer and Adam Wise for help with technical supports and advises. I would also thank past and present colleagues at Carnegie Mellon University, Dr. Ranga Kamaladasa, Dr. Mohamed Abdelmoula, Dr. Mina Abadier, Wenhao Chen, Dasheng Li, Darshil Gala, Jonathan Goodwill, Phoebe Yeoh, Yuanzhi Ma. Very special thanks to Dr. Abhishek Sharma for all his effort and help to develop and improve my dissertation. He is one of my best friends and an enthusiastic scientist always gives me a strong motivation.

Lastly, I would like to thank my parents and brother for their unlimited support and encouragement for me to pursue this degree. Whenever I have faced hardships and sufferings, their encouragements have always provided me strength to overcome and proceed toward next step. Love you all.

This work was supported by NSF Grant No. DMR1409068 and SRC Contract No. 2012-VJ-2247. Also, I acknowledge use of Materials Characterization Facility at Carnegie Mellon University supported by grant MCF-677785.

Table of Contents

List of Figures

1 Introduction

The recent trends in electronic devices such as cell phones and laptops are to make them lighter, smaller, and faster with lower energy consumption. Along with these developments, non-volatile memory storage technologies have also seen active development. Recently, charge-storage type memory, such as flash memory, has achieved great success in terms of market size (> 25 billion USD) and the superior performance (scalability: 16 nm, write/read time: 10 μs, endurance: 10^4, retention: ~ years).[1,2]. However, it has been reported that the current Si-based flash technology is approaching its physical limits in scalability, write speed, and endurance for future applications in nonvolatile memory devices.[3]

There are various emerging non-volatile memory technologies: ferroelectric random-access memory (FeRAM)[4], spin-transfer torque magnetoresistive RAM (STT-MRAM)[5], phase change RAM (PCRAM)[6] and resistive RAM (RRAM)[7,8]. Among these, RRAM has received increasing interest because it has a simple metal-insulator-metal (MIM) structure and shows promise in overcoming scaling limit in current flash technology. It is expected that RRAM devices can achieve <5 nm device size, <10 ns write speed, >10 years retention time, and ~1 pJ energy consumption per switching cycle.[1,3]

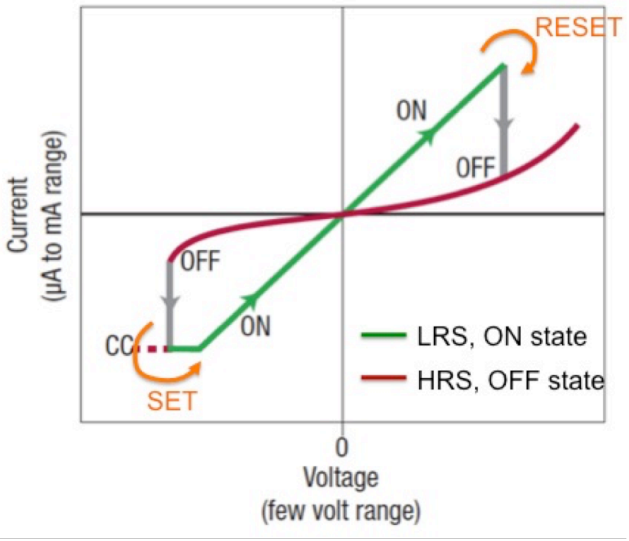

Figure 1.1 A typical current (I) – voltage (V) switching curve in a TiO_2-based resistive switching device showing resistance changes during bias sweep. The SET (OFF to ON state) and RESET (ON to OFF state) transitions occur at different polarities of applied voltage. CC stands for compliance current.[7]

Resistive switching refers to electrical resistance changes in an oxide functional layer from an OFF state where the oxide is in a high resistance state (HRS) to an ON state where the oxide is in a low resistance state (LRS). These changes occur under an applied bias (see Figure 1.1).[7] When a SET or RESET voltage is reached, the device transitions from HRS to LRS or LRS to HRS, respectively. It is widely accepted that local conductive filament (see Figure 1.2) is created during a one-time conditioning process of as-fabricated oxide layer (called electroforming or forming). Shunting and rupturing of the filament between the two electrodes can modulate the device resistances during subsequent voltage sweeps.

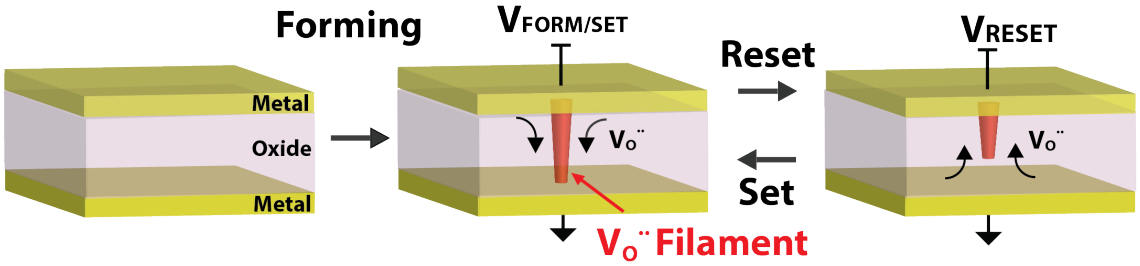

Figure 1.2 A schematic diagram showing the filamentary switching model in a metal/insulator/metal (MIM) structure (after Waser *et al*. [7])

1.1 Motivation for current study

Although the observations of resistance change in oxides date back to the 1960s, full-scale research for memory application started in the 1990s with various metal oxides such as $SrTiO_3$, NiO, and TiO_2.[9] Since then, an ample amount of research has been conducted to investigate the nature of resistive switching and improve device performance. Quite surprisingly, however, the nature of the conductive paths and basic switching mechanisms are still under debate. Therefore, several challenging issues remain before RRAM can be commercially available: improving switching endurance, long-term thermal stability and uniformity.[10]. A variety of switching models have been suggested and tested by different groups by using various electrical testing methods [11–17] and numerical simulations [11,18–23]. A question then, arises as to why the basic understanding in RRAM is still lacking despite most groups providing experimental supports to back up their models. The reason is that there have been reported only indirect experimental results in terms of structural and chemical analysis of the conducting filaments. Size,

shape, atomic structure, chemical composition, and distribution of the conductive paths, all of which are essential to understanding RRAM, are still largely unknown.

1.2 Objectives and hypotheses

The primary goal of this study is to identify the above-mentioned characteristics of the conductive filaments and reveal the elementary processes for resistive switching in transition metal oxide (TiO_x, TaO_x, $HfAlO_x$)-based RRAM devices by using various electron microscopy techniques. The hypotheses of the study are "resistance change of RRAM devices is mediated by creation, redistribution, and agglomeration of oxygen vacancies" and "the current flow during resistive switching occurs through a localized conductive pathway in the functional oxide layer". In order to test the hypotheses, both *in situ* and *ex situ* transmission electron microscopy (TEM) techniques will be adopted, and also both model single-crystal and actual thin-film RRAM devices will be investigated.

It is believed that motion of oxygen vacancies play a key role in resistive switching by acting to form and rupture conductive filaments during switching.[7,21,24,25] It is well known that oxygen vacancies act as shallow donors and can increase electrical conductivity of oxides.[26] Also, oxygen vacancies are charged and can migrate under the influence of electrical bias.[27,28] Although there have been reports using TEM to demonstrate the correlation between oxygen vacancy and resistive switching, only the indirect evidences have been reported.[29–32] In the current study, using an *in situ* biasing TEM approach, a direct oxygen vacancy mediated resistance change in a RRAM device will be demonstrated.

In addition, further detailed oxygen vacancy defect dynamics will be examined. Accepting the concept of vacancy mediated resistance change in RRAM devices, one can categorize resistive switching processes into three elementary steps that are essential for resistive switching: 1) creation and 2) migration of oxygen vacancies, 3) and their coalescence into aggregates (and dissolution of aggregates). The formation of such aggregates realizes the necessary conductive pathway for LRS (ON state) in the case of TiO_2. In order to achieve this, *in situ* biasing TEM experiments will be performed with model single-crystal TiO_2-based RRAM devices. Particularly for this study, a constant and relatively low bias will be applied to the specimen such that the three elementary processes will be demonstrated at low temperature where thermal reduction of oxides does not occur. Since vacancy creation is expected to occur as a result of applied electric field (electrochemical reaction) rather than Joule heating,[8,14,24] maintaining low temperature during biasing is critical.

Another important goal of the current study is to investigate the conductive filament size and switching temperature in thin film RRAM devices. It is expected that localized Joule heating-induced phase changes (e.g. local crystallization) could occur in functional oxides during resistive switching. Thus, one can determine the potential filament location by comparing as-fabricated and switched devices. Also more importantly, the filament temperature during resistive switching can be estimated by transient thermometry. $HfAlO_x$-based RRAM devices will be examined by using cross-sectional TEM techniques. The cross-sectional TEM specimens will be prepared from as-fabricated and

switched devices and any structural change (e.g. crystallization) will be tracked by high-resolution TEM (HRTEM) imaging. Also, the crystallization temperature of the functional oxide layer will be determined by observing degree of crystallization with HRTEM imaging at different annealing temperatures. In addition to the microstructural analysis, transient thermometry[11,33] will be performed to estimate the filament temperature during switching together with numerical simulations. The chemical makeup of the filament will also be assessed by using scanning TEM electron energy-loss spectroscopy (STEM-EELS).

Lastly, two on-going projects investigating the switching mechanisms and filament chemical nature will be discussed with some preliminary data. First is an *in situ* biasing electron holography experiment to capture electrostatic potential and/or charge distribution around the conductive filament in functional oxide layers while electric field is applied to RRAM devices.[34,35] The filament location, size, and/or its distribution (single or multiple filaments) can be affected by inherent Joule heating due to current flow through localized conductive pathways during resistive switching. Thereby, observed microstructural changes such as crystallization may be aftereffects of switching instead of its cause. Thus, tracking microstructural change by conventional TEM imaging techniques may not be able to discern the filament structure and location. Alternatively, mapping the electrostatic potential and/or charge distribution in the devices while electric field is applied *in situ* can be the most effective way to understand the filament size and position.

The on-going project is chemical analysis on plan-view oriented RRAM devices. Given that a cylindrical shape filament is embedded within a functional oxide layer in a RRAM device (see Figure 1.2), tracking the switching related chemical changes (oxygen vacancy concentration) around the filament with the cross-sectional orientation might be difficult due to the presence of the unchanged oxide surrounding the filament in the electron beam path. On the other hand, if the electron beam path is parallel to the conductive filament (i.e. electron beam is parallel to the cylindrical axis of the filament), the chance to observe the chemical change can be significantly higher with this plan-view orientation than with the cross-sectional orientation view. This idea has been developed in order to design and fabricate TaO_x-based RRAM devices so that chemical changes associated with resistive switching can be investigated by STEM-EELS analysis.

This thesis starts with background chapter introducing the details regarding the resistive switching phenomena, its mechanisms, current technological status and future development directions. The chapter 3 and 4 discuss about the fundamental defect dynamics essential for the resistive switching by using model TiO_2-based single crystal RRAM devices with *in situ* electrical biasing TEM. The chapter 5 describes filament size and switching temperature estimation in thin film $HfAlO_x$-based RRAM devices via HRTEM analysis and transient thermometry. The following chapter 6 demonstrates on-going research works and future plans. The last chapter summarizes the key concepts and findings in this document.

2 Background

In general, RRAM devices refer to non-volatile memory devices whose resistance can be modulated by application of external electrical stimuli.[7,25,36] Since the 1990s, the number of published studies on RRAM research has skyrocketed and a variety of different types of switching devices have been proposed, fabricated and characterized. Those devices use different metal-insulator-metal (MIM) systems; different functional materials: $SrTiO_3$[37,38], TiO_2[14], HfO_2[15,20], Ta_2O_5[3,11], NiO[39], ZnO[40] and different electrode materials: Pt, Au, TiN, Cu, Au. Depending on the different MIM combinations, remarkably different device characteristics and switching mechanisms have been reported. Although a universal switching mechanism may not exist, there are widely accepted switching models; one category is “filamentary switching" mechanism and its opposite is “interfacial switching mechanism (or non-filamentary switching mechanism)”.[41] If the switching takes place in a local manner (resistance change is independent on device size), it is called filamentary switching. If the resistance change is depending on the device size, on the other hand, it is called interfacial switching.

2.1 Filamentary switching mechanism

It is reported that the device resistance change (ON/OFF ratio) does not depend on the device size, thus indicating that current conduction occurs through a local conductive path.[15,42] Based on a device scaling experiment, the conductive filament size is estimated to be below 10 nm.[43] Also, localized morphological/chemical changes associated with resistive switching have been reported using a variety of characterization tools.[14,29,31,32,44–46] Based on these observations, filamentary switching mechanism has

been proposed and widely accepted for the type of transition metal-oxides ($HfAlO_x$, TaO_x) in the field of resistive switching.

Jeong *et al*.[24] proposed that resistive switching takes place due to the presence of localized conductive filaments based on the observation of nonhomogeneous local oxygen distribution. These filaments in the functional layer act to connect and disconnect the two electrodes within the MIM structure under applied biases, thus acting to modulate the device resistance. The filaments themselves are distinguished from the surrounding matrix through local differences in composition and/or structure, often as an agglomeration of point defects.[14] For example, Magnéli phases (Ti_nO_{2n-1}) formation, oxygen-deficient phases, has been observed in TiO_2-based RRAM devices.[29,47] It is well known that oxygen vacancies are point defects that are charged, highly mobile and can participate in current conduction in metal oxide systems.[7,13,24] Although it is reported that the metal interstitials in transition metal oxides can also contribute to increase the conductivity of the oxides,[12] majority of RRAM studies have demonstrated oxygen vacancies are the primary defect that constitutes conductive filaments.[14,24,48]

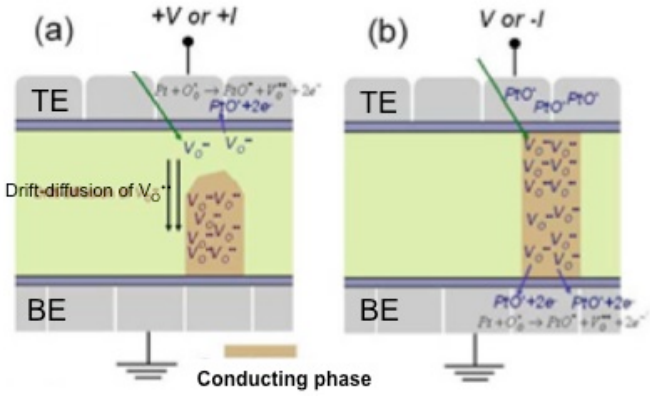

Figure 2.1 Schematic diagrams illustrating conductive filamentary switching model in Pt-TiO_2-Pt system. (a) Migration of positively charged oxygen vacancy towards the BE can form partial conductive Magnéli phases during the electroforming process and (b) subsequent opposite bias complete the formation of the conductive filament.[24]

Figure 2.1 is a schematic diagram showing oxygen vacancy motion and formation of a conductive filament in a Pt/TiO_2/Pt RRAM device under applied bias. In a typical submicron-scale TiO_2 RRAM device with ≤ 100 nm functional layer thickness, initially very resistive TiO_2 oxide layers in MΩ range undergo a sudden resistance drop to the kΩ range during an electroforming event. The electroforming can be defined as an initial resistance decrease caused by creation of oxygen vacancies and formation of conductive filament under an applied voltage.[24] When a positive bias is applied to the top electrode (TE) as shown in Figure 2.1(a), oxygen vacancies are assumed to form at the TE/TiO_2 interface by an electrochemical reaction (Equation 2.1).[7] Since oxygen vacancies are positively charged defects, pre-existing and newly created oxygen vacancies drift and diffuse toward the negative biased bottom electrode (BE), where they accumulate and

form a partial filament as depicted in Figure 2.1(a). The partial filament is assumed to form because an additional resistance drop is observed when the opposite bias is applied.

$$O_o \rightarrow V_O^{\cdot\cdot} + 2e^- + 1/2\, O_2. \qquad \textbf{Equation 2.1}$$

When a negative bias is applied to the TE as depicted in Figure 2.1(b), positively charged oxygen vacancies can be created at the BE/TiO_2 interface, and would migrate towards the TE. Again, these additional oxygen vacancies can accumulate and form a continuous conductive filament connecting the two electrodes, resulting in further lowering the oxide resistance significantly (see Figure 2.1(b)). This process is called SET. The following opposite polarity bias acts to rupture the filament by creating a gap at the TE, thus leading to a resistance increase for the TiO_2 layer or RESET process. Subsequent alternate bias can induce formation and rupture of the filaments so that the resistance of the TiO_2 oxide layer can be modulated. Note that alternate polarities of biases are applied to make the device switch. This is called "bipolar" switching due to the polarity dependency for this switching process. If the switching is not dependent on polarity of applied bias, the switching process is called "unipolar".

Although the presence of the gap in the filament at a high resistance state (HRS) is commonly accepted, the filament configuration at a low resistance state (LRS) is still debatable. According to Szot *et al.*[14], a 1-2 nm gap is present between the filament and the electrode at LRS, and electrons tunnel through the gap. On the other hand, Jeong *et*

al.[24] suggested that a complete filament connects the two electrodes at LRS and Ohmic-like current conduction occurs.

Further detailed descriptions of SET and RESET processes are provided by Nardi *et al*.[15] Assuming resistive switching takes place by ion migration, there are three driving factors that can affect switching characteristics; local electric field, oxygen vacancy concentration, and temperature gradient due to Joule heating. The SET transition consists of two processes; vertical gap filling (nucleation of filament) and lateral increase in filament area (growth). The gap width is dependent on the RESET voltage. The higher the RESET voltage, the larger the gap width as well as the larger the device resistance. During the RESET process, a gap is formed at a critical electric field and temperature could cause the onset of ion migration. Because of high resistivity in the gap, opening the gap leads to less current flow and lower temperature which leads to slower the ion migration. This negative feedback process controls the RESET transitions.

2.2 Non-filamentary switching mechanism (Interfacial switching mechanism)

On the other hand, it is reported that some transition metal oxides (TiO_2,[49] TaO_x/TiO_2[50]) and complex oxides such as $Pr_{0.7}Ca_{0.3}MnO_3$, [51] $La_{1.65}Sr_{0.35}CuO_4$,[52] and Nb-doped $SrTiO_3$[53] based-RRAM structure exhibits electrode area dependent low / high resistance states as seen in Figure 2.2. This is interpreted as the conduction occurs over the entire device area.[51]

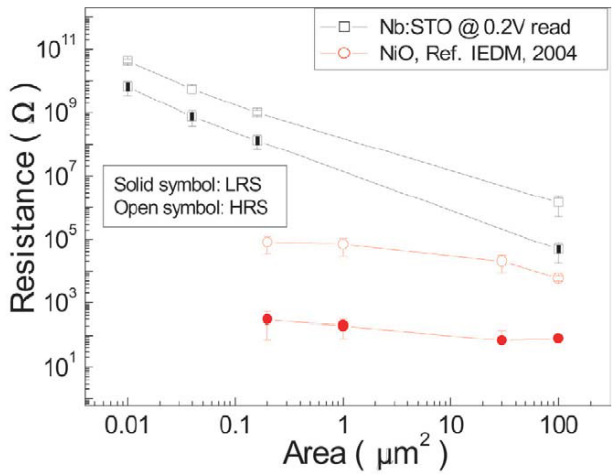

Figure 2.2 Electrical resistance versus memory cell area profile of Nb-doped $SrTiO_3$ (Nb:STO) and NiO. The resistance of NiO is independent of the cell area, indicative of filamentary switching. On the other hands, the resistance of Nb:STO shows linear dependence on the cell area, suggesting the resistive switching takes place over the entire area of the cell.[41]

The origin of the resistance change in this type of switching is attributed to the Schottky-like barrier modulation. It is reported that a conventional Schottky contact model (i.e. barrier changes (height and width) depending on the work function of metals and the electron affinity of semiconductors) cannot explain this type of resistive switching.[54] Rather, it is believed that an interface-state-induced band bending and interfacial reactions at the metal/electrode interface can cause the resistive switching.[54,55] In this model, the barrier change does not depend on the work function but on a net charge in the interface states. This alternative switching mechanism is often called “interfacial switching” or “non-filamentary switching”.[56]

2.3 Classification of RRAMs

A number of different MIM structures exhibiting resistive switching have been reported and there has been an effort to categorize the various types of RRAM devices. Waser *et al*.[13] suggested three subgroups: electrochemical metallization memory effect (ECM), thermochemical memory effect (TCM), and valence change memory effect (VCM). All three are due to local (filamentary) changes. Note that the grouping does not exhaust all the possible RRAM types, but it provides a general idea of different types of resistive switches.

To begin with, a MIM stack with an electrochemically active metal electrode (e.g. Ag) and an inert electrode (e.g. Pt) gives rise to a resistive switching effect that is called "electrochemical metallization memory (ECM)". When an electric bias is applied to such a device, Ag is ionized by electrochemical reactions and drifts toward the counter electrode through the insulating layer (I), forming a dendritic conductive pathway connecting the two electrodes (LRS). Subsequent opposite polarity bias retracts the dendritic filaments and results in HRS. This type of resistive switch is also called "conductive bridge RAM (CBRAM)".[7]

Secondly, in some transition metal oxide-based RRAMs such as Pt/TiO_2/Pt[29] and Pt/ZnO/Pt ,[57] switching is attributed to the thermo-chemical memory effect (TCM). In this case, RESET is caused by a thermal dissolution of the filament due to excessive Joule heating. Since the mechanism does not rely on the polarity of applied bias, this kind of RRAM device typically shows unipolar switching behavior. Due to the nature of the

high temperature operation, this type of device may have inherent limitations for device functionality in terms of uniformity and/or endurance.[9]

The last proposed switching process is valence change memory effect (VCM). For this effect, resistance modulation is attributed to reduction/oxidation (redox) –based ionic migration under applied electrical field (Equation 2.1). Many transition metal oxide RRAM structures fall into this category such as $SrTiO_3$, TiO_2, $Hf(Al)O_x$, and Ta_2O_5 sandwiched by inert electrodes such as Pt, Au, and TiN. The detailed switching mechanism for this type of resistive switches has already been described in Chapter 2.1. The present study will focus on VCM type RRAMs where resistive switching, from now on throughout the document, refers to redox reactions and oxygen vacancy motion to induce resistance changes.

2.4 Structural / chemical changes in RRAM devices while resistive switching

It has been proposed that resistive switching can occur purely be electronic mechanisms such as charge trapping and detrapping.[58] This mechanism, however, cannot be applicable to resistive switching due to its non-volatile characteristic of the resistance state. Thus, it is rather believed that the resistance change in RRAM devices is associated with some permanent structural changes in the functional oxide layer involving ion migration (e.g. oxygen vacancies) that can alter the electrical properties of functional materials. On the other hand, it is reported that fast switching (~ns) and long retention (~10 years) cannot be achieved simultaneously because the diffusion coefficient (D) and

drift mobility of isolated oxygen vacancies (μ_q) are proportional to each other based on Einstein's relation (Equation 2.2):

$$D = {\mu_q k_B T}/{q} \qquad \textbf{Equation 2.2}$$

(μ_q: mobility of vacancies, k_B: Boltzmann constant, T: temperature, q: unit charge of carriers). This discrepancy has been referred to in the resistive switching field as the "voltage-time dilemma".[23,58] It can be resolved if non-linear oxygen vacancy motion exists within high electric fields, which can accelerate switching speed [59]. Alternatively, if oxygen vacancies form agglomerates that are found to be stable, this would help to explain long retention times.[60]

Wadsley defects and Magnéli phases in TiO_2 are examples of oxygen vacancy agglomerates. It is well known that the off-stoichiometry (oxygen deficiency) in TiO_2 can be accommodated by the formation of the Wadsley defects that act to remove oxygen planes from the crystal structure as illustrated in Figures 2.3.[61–64] When oxygen vacancies are accumulated, they can aggregate along certain crystallographic shear planes; typically {011}, {121} and {132} for rutile TiO_2.[61] These crystallographic shear plane defects are called Wadsley defects.[61–63] Wadsley defects can arrange themselves in a periodic fashion and, at sufficiently high density, result in the formation of Magnéli phases, Ti_nO_{2n-1} (n is an integer, $4 \leq n \leq 9$), which are oxygen-deficient phases of rutile TiO_2.[61–63] Rutile is the most common natural form of TiO_2. Most studies regarding Magnéli phases use vacuum annealed rutile crystals to induce the Magnéli phase

formation.[61,63,65] Thus, temperature is an important factor to induce the rutile to Magnéli phase transformation. Oxygen atoms can escape the system by thermal desorption, thus leaving oxygen vacancies behind.[66,67] Temperature further facilitates this process by enhancing migration processes. Bursill and Hyde[61] have conducted an extensive microstructural study on vacuum annealed TiO_2 single-crystals. Figure 2.4(a) is a bright-field (BF) transmission electron microscopy (TEM) image, showing Wadsley defects in multiple orientations (differently oriented Wadsley defects are marked as numbers 1 to 4) and Figure 2.4(b) is a selected area diffraction pattern (SADP) obtained from '2' in Figure 2.4(a), depicting streaking along <011> direction corresponding to the presence of <011>-oriented Wadsley defects. The satellite reflections along <132> direction in the SADP in Figure 2.4(c) indicate the presence of <132>-type Wadsley defects.

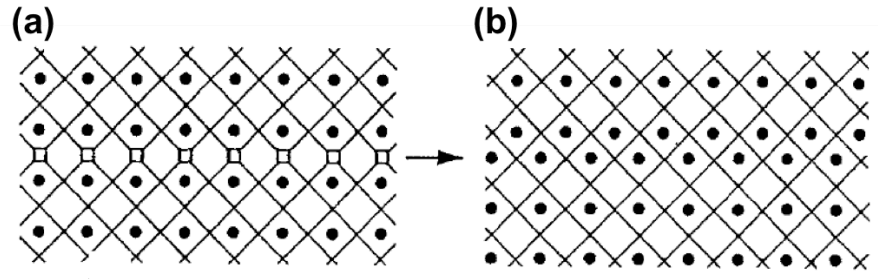

Figure 2.3 Schematic illustration of how oxygen vacancies agglomerate to form a shear plane (Wadsley defect).[64] The black circles represent the metal atoms and the oxygen atoms are located at the intersections of the mesh while the squares represent the oxygen vacancies.[64] When (a) oxygen vacancies align in a crystallographic plane, the result is (b) the elimination of oxygen vacancies and the formation of a planar defect by shearing the structure.

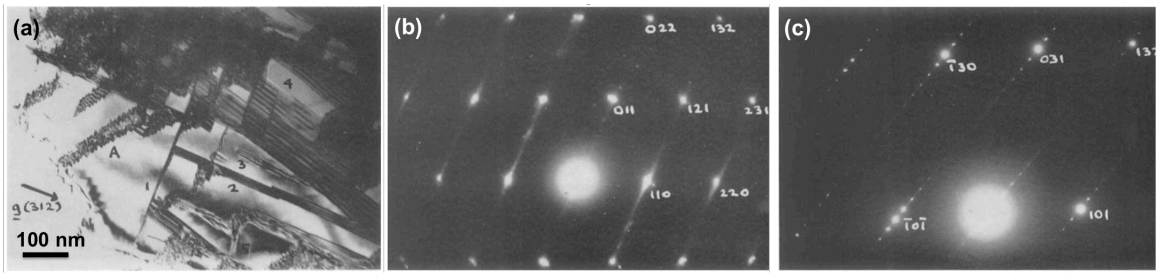

Figure 2.4 BF TEM micrograph and electron diffraction patterns of reduced single-crystal TiO_2. (a) BF TEM image showing Wadsley defects in multiple orientations, (b) SADP obtained from '2' in (a), depicting steaks along <011> directions. (c) An example of electron diffraction pattern of Magnéli phases. The satellite reflections along <132> direction correspond to the presence of Ti_nO_{2n-1} (n=19) Magnéli phases.[61]

Many attempts have been made to identify the formation of vacancy agglomerates in TiO_2-based resistive switching devices by using a variety of characterization methods. Kwon *et al*.[29] and Strachan *et al*.[47] showed Ti_4O_7 Magnéli phase formation in $Pt/TiO_2/Pt$ unipolar switching devices using transmission electron microscopy (see Figure 2.5). Szot *et al.*[14] also reported Magnéli phase formation in single-crystal TiO_2 by using X-ray diffraction. Additionally, ionic migration and agglomeration has also been indicated to occur in other metal-oxide devices. Privitera *et al.*[68] demonstrated the presence of a metallic oxygen deficient Hf-rich phases in HfO_x-based resistive switches with scanning TEM high-angle annular dark field (STEM HAADF) and electron energy loss spectroscopy (EELS). Also, Celano *et al.*, used conductive-AFM and provided the three-dimensional characterization of the conductive filament in HfO_x based devices.[69] Miao *et al.*[30] reported oxygen deficient Ta-rich channel surrounded by a nanocrystalline

Ta_2O_5 in $Ta/TaO_x/Pt$ RRAM device by using a synchrotron-based nanobeam X-ray fluorescence measurement. Recently, oxygen deficient conducting channels have been reported in TaO_x-based RRAM device with an *in situ* biasing TEM characterization and EELS.[32]

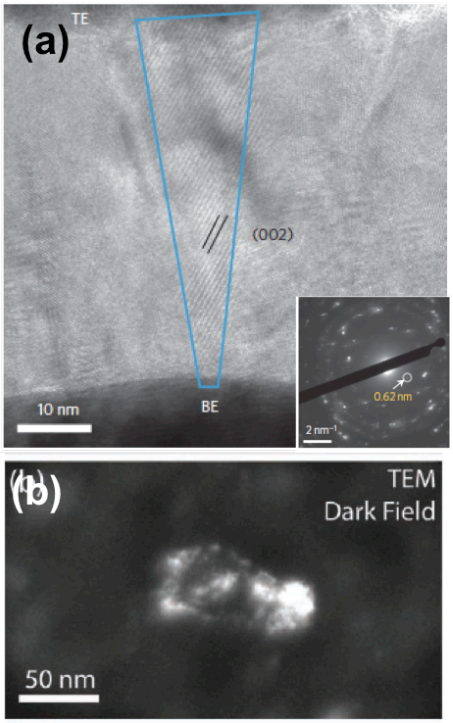

Figure 2.5 TEM micrographs presenting Magnéli phase presence in $Pt/TiO_2/Pt$ resistive switching devices. (a) Cross-sectional HRTEM image showing (002) lattice planes of Ti_4O_7 Magnéli phase connecting the top and bottom electrodes.[29] (b) Plan-view dark-field (DF) TEM image showing Ti_4O_7 Magnéli phase (brighter contrast).

All the observations listed above fall in to the regime of the filamentary switching mechanism, in that the observed structural and/or chemical changes are localized in the

oxide functional layer. Quite remarkably, even though extensive analyses have been reported so far, there is still debate regarding the nature of the conductive filament and the underlying switching mechanisms. This is because most of above experimental results were produced by indirect methods and performed in a problematic experimental condition (e.g. high power operation).

In the following chapter 3 and 4, I demonstrated the fundamental defect dynamics associated with resistive switching at low power regime. *In situ* electrical biasing TEM techniques were adopted and TiO_2-based model single-crystal RRAM devices were used to facilitate the defect imaging under TEM.

3 *In situ* biasing TEM investigation of resistive switching events in TiO_2-based RRAM

This chapter describes defect dynamics associated with resistive switching events observed using *in situ* biasing TEM techniques. Model single-crystal rutile TiO_2 and ALD-grown TiO_2 film has been selected for functional/insulating layers in MIM stacks fabricated using focused ion beam (FIB) milling.

3.1 Introduction

Oxygen vacancy motion and their agglomeration are often associated with resistive switching in TiO_2.[7,12,24] However, the defect distribution and changes of device resistance are still poorly linked and require direct analysis.[29,47] Extensive *ex situ* microstructural analysis has led to propose switching mechanisms that invoke defect formation/motion, but direct observation of defect evolution under applied bias is still lacking. In this chapter, direct observation of Wadsley defect formation (missing planes of oxygen in the rutile structure) and evolution has been demonstrated by using *in situ* electrical testing of TiO_2-based resistive switches inside the TEM column. The goal of the study is to monitor structural transformations (defect evolution) that accompany application of electric field. The hypothesis is resistance change of RRAM devices is caused by Wadsley defect (oxygen vacancy aggregates) growth and dissolution. I expected to observe connection and disconnection of the oxygen vacancy aggregates at an electrode during the SET and RESET processes, respectively. Both single-crystal and

nano-polycrystalline thin film TiO_2 devices were fabricated and investigated. Typically, RRAM devices have thin film MIM stacks with an amorphous oxide functional layer and such devices were examined by *in situ* biasing experiments in this study. The single-crystal TiO_2 has also been used to facilitate TEM defect imaging and served as a control system akin to individual grains in the polycrystalline TiO_2 film.

3.2 Experimental

This section describes the materials and TEM specimen sample preparation methods. Also the TEM imaging techniques and *in situ* electrical biasing approach are explained.

3.2.1 Materials

For the single-crystal devices, I have fabricated the metal/insulator/metal (MIM) RRAM devices consisted of W/TiO_2/TiN layers by thin film deposition and dual-beam focused ion beam (FIB) techniques. Single-crystal rutile TiO_2 (001) substrates were purchased from MTI Corporation. A 250 nm Ti oxygen getter layer was sputter deposited on the backside of the crystal and annealed at 500°C for 1 hour in a vacuum chamber (10^{-8} Torr). This process increased oxygen vacancy concentration in the crystal and electrical conductivity increased from 50 S/m to 1290 S/m.[70] Subsequently, 100 nm TiN film was sputtered on the topside of the reduced crystal and 20 nm Mo film was sputtered on top of the TiN film. The TiN film acted as an electrode of the *in situ* biasing TEM specimen and the Mo film served as a protective layer to avoid TiN film oxidation.

For the thin film TiO_2 devices, 5 nm Ti and 500 nm Pt were sputtered on Si, followed by deposition of 100 nm thick TiO_2 functional layer by atomic layer deposition (ALD) at 250 °C. Subsequently, 70 nm TiN was sputtered (with 20 nm Ru capping layer) to complete the Pt/TiO_2/TiN MIM stack.

3.2.2 TEM specimen preparation

Electron transparent specimens (thickness of ~ 100 nm) were fabricated for *in situ* biasing TEM studies using an *in situ* lift-out technique inside an FEI Nova 600 Nanolab dual-beam focused ion beam (FIB) equipped with an Omniprobe nano-manipulator. For the single-crystal devices, ~ 3×1.5×1.2 μm^3 specimens were extracted and attached to tungsten (W) scanning tunneling microscopy (STM) probes purchased from Bruker Corporation (ion-beam induced chemical vapor deposition (CVD) W capping layer was deposited on top of the sputtered Mo film). W was deposited by electron-beam assisted CVD on the bottom side of the extracted slabs as both an electrode and a weld to the W STM probes. This process thus fabricated a complete W/TiO_2/TiN device structure inside the dual-beam FIB system (Figure 3.1(a)). The slabs were thinned down to electron transparency (~100 nm thickness) at 30 keV with final polishing at 5 keV to remove any Ga^+ ion induced damage layers.

For the thin film TiO_2 devices, the specimens were similarly prepared via FIB milling and lift-out as described above. Slabs were extracted *in situ*, mounted onto STM W probes and thinned down to electron transparency. Since these specimens already have a

complete MIM structure (Pt/TiO_2/TiN), the slabs were simply mounted onto the W STM probes by Pt welding (Figure 3.1(b)).

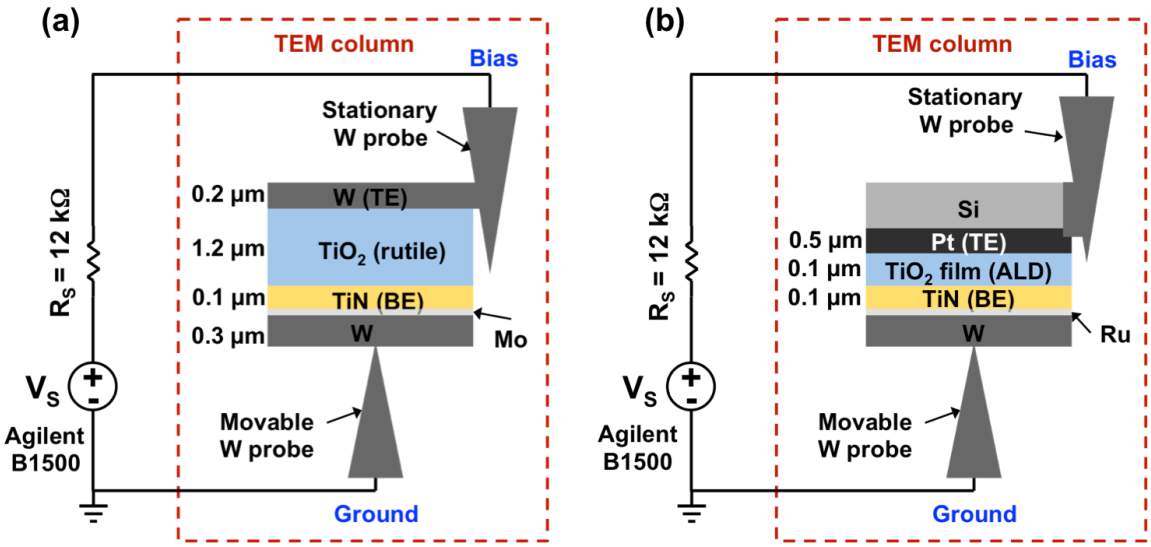

Figure 3.1 Schematics of *in situ* biasing TEM setup for (a) single-crystal TiO_2 devices and (b) thin film TiO_2 devices.

3.2.3 *In situ* biasing TEM set up

The *in situ* biasing TEM experiments were performed in an FEI Tecnai F20 operated at 200 keV with a Nanofactory® *in situ* biasing single-tilt holder. Figure 3.1(a) and (b) depict the *in situ* TEM biasing setup schematic for single-crystal and thin film devices, respectively. Two STM probes can be mounted in the TEM holder. A piezo-driven nano-manipulated W STM probe (1 nm positioning precision) made electrical contact to the devices and was assigned electrical ground. The stationary W STM probe where the devices were attached was electrical biased. An Agilent Semiconductor Parameter Analyzer B1500 was used to apply DC sweeps. A 12 kΩ external series resistor was

connected to the circuit to suppress excessive transient current due to parasitic capacitance discharge while applying voltage.[71] Considering the geometry of the setup, W and Pt are referred as top electrodes (TE) and TiN is referred to as the bottom electrode (BE).

For the single-crystal device study, two-beam condition bright-field (BF) TEM imaging was utilized to observe formation and evolution of Wadsley defects. High-resolution (HR) and high-angle annular dark field (HAADF) imaging was performed in the FEI Tecnai F20 in scanning transmission electron microscopy (STEM) mode in order to identify local structural/chemical changes in thin film devices. Figure 3.2(a) is a BF TEM image of an as fabricated single-crystal device showing the W/TiO_2/TiN MIM structure. The curved dark contrast lines in the TiO_2 crystal are bend contours and the notch at the top-left corner was intentionally FIB milled to prevent electrically shorting the device during biasing. The W probe made electrical contact to the device by touching the FIB deposited W capping layer. Figure 3.2(b) shows a BF TEM image of the TiO_2-based thin film device. The functional TiO_2 film is sandwiched by Pt (TE) and TiN (BE). The bright contrast in the center of the Si substrate is an artifact created during the FIB thinning process.

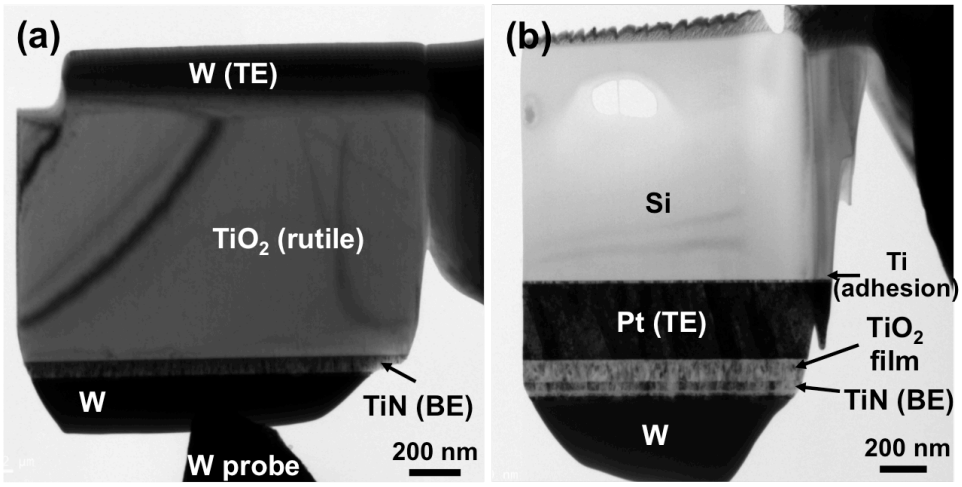

Figure 3.2 BF TEM images of pristine (a) single-crystal TiO_2 device and (b) thin film TiO_2 device before any biasing.

3.3 Results and discussion

In the single-crystal TiO_2 devices, TEM analyses coordinated with electrical biasing show that electroforming caused decrease of electrical resistivity while also induced Wadsley defect formation. Figure 3.3 shows the *I-V* plot of the electroforming process. After biasing the device to induce this electroforming event at about 1 V, a large Wadsley defect zone was observed at the W/TiO_2 interface extending towards the TiO_2/TiN interface, covering nearly the entire sample (Figure 3.4(a)). Additionally, a ~50 nm Wadsley defect-free zone was observed at the TiO_2/TiN interface (inset in Figure 3.4(a)). Selected area diffraction patterns (SADPs) were collected around the center of the functional layer (marked with a circle in Figure 3.4(a)) for both as-fabricated and electroformed devices. Figure 3.4(b) and (c) are diffraction patterns close to the [100]-zone axis before and after the *in situ* biasing induced electroforming process. Figure 3.4(c) reveals satellite reflections and steaks along <011> directions consistent with

{011} shear planes. These extra reflections indicate the presence of secondary phases in the specimen. Note that the SADP in Figure 3.4(c) appears different compared to the typical diffraction pattern of Magnéli phases as shown in Figure 2.3(c). This can be simply because the specimen orientation has been deviated from the <111>-zone axis, where one can optimally determine the presence of Magnéli phases.[61] Since the *in situ* TEM holder used in the present experiment has only one tilt axis (alpha (α) tilt: tilt around the rod of the TEM holder), Magnéli phases identification was not possible. Nevertheless, the streaks in Figure 3.4(c) provide unambiguous evidence of Wadsley defects. Thus, the large defect area is regarded as a large Wadsley defect zone.

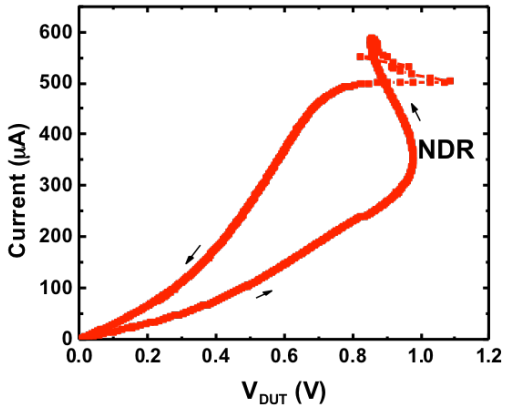

Figure 3.3 Current (I) versus voltage (V) across the device (V_{DUT}) curve, showing the electroforming behavior of a single-crystal device.

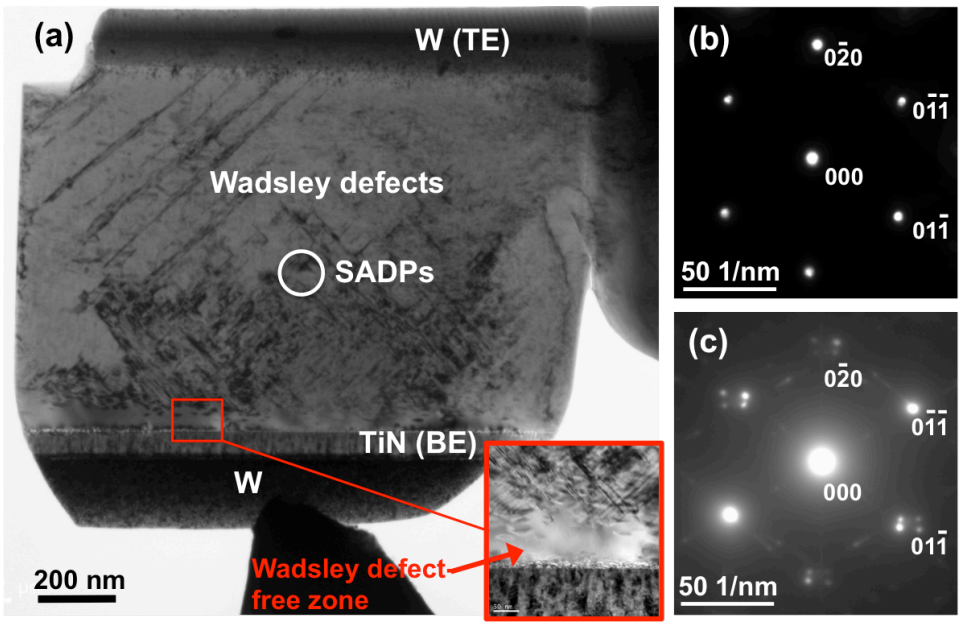

Figure 3.4 TEM analysis of electroformed TiO_2 single-crystal device. (a) BF TEM image showing large Wadsley defect zone formation after electroformation. Inset shows a magnified view of a Wadsley defect-free zone near the BE. SADPs of (b) the as-fabricated and (c) electroformed device. The diffraction patterns were obtained from near the center of the functional layer as marked with a circle in (a).

After electroforming, the device exhibited very stable resistive switching as demonstrated in the *I-V* behavior shown in Figure 3.5. The large Wadsley defect zone appeared to be stationary while applying bias. This defect zone may act as a virtual electrode for the switching and the device resistance appears to correlate with the Wadsley defect distribution. In other words, oxygen vacancy accumulation in the defect-free zone corresponds to extension of Wadsley defects into the zone and connection to the large defect zone as the device undergoes SET processes (Figure 3.6(a)). The defects retract during RESET processes (Figure 3.6(b)) and extend again during another SET process

(Figure 3.6(c)). More importantly, when the *I-V* did not show the hysteretic resistive switching behaviors during *in situ* biasing (below the SET voltage), Wadsley defect extension has not been observed (not shown here), thus, ascertaining a direct correlation to oxygen vacancy motion associated both with SET and RESET processes in the single-crystal TiO_2 device.

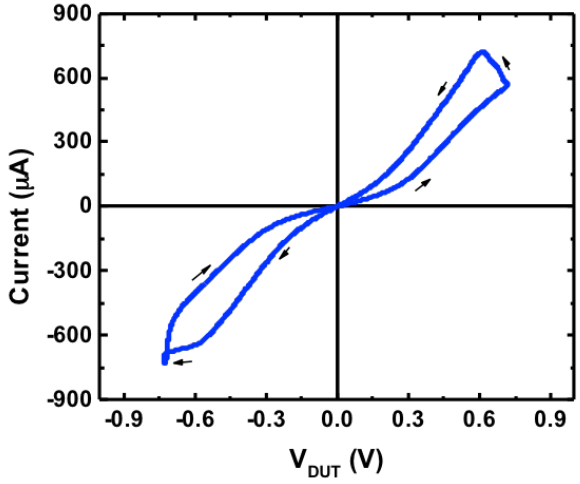

Figure 3.5 Switching *I-V* of TiO_2 single-crystal device. V_{DUT} refers to voltage across the device under test.

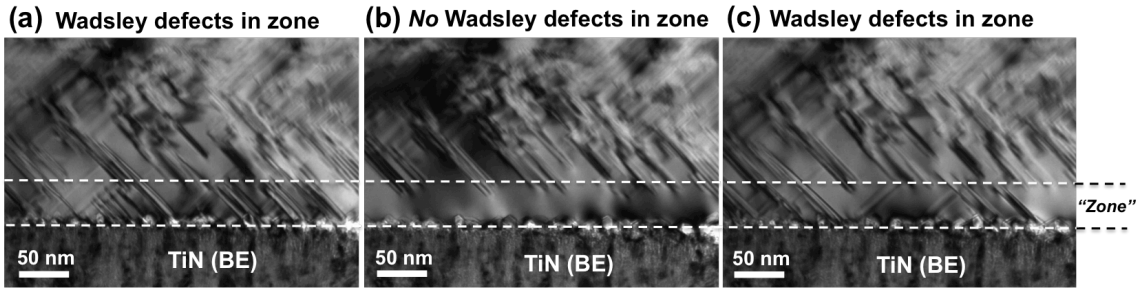

Figure 3.6 A series of BF TEM images during resistive switching of a single-crystal TiO_2 device. The "zone" marked by dashed lines is the Wadsley defect free area. (a) Wadsley

defects extend into the zone during SET process (LRS), (b) retracted during RESET process (HRS), and (c) extended again during another SET process (LRS).

These observations indicate two possible conducting mechanisms; i) individual Wadsley defects behave as conductive filaments and they are distributed globally, ii) contact resistance at the TiO_2/TiN interface changes by Schottky-like barrier modulation. Above results, however, support neither the filamentary nor the interfacial switching mechanism, in that there is no obvious, single conductive path and it is difficult to identify any possible characteristics of Schottky-like barrier formation. Nevertheless, oxygen vacancy motion associated with resistive switching has been successfully demonstrated, and also I have established a viable methodology for tracking oxygen vacancy motion in TiO_2 single-crystal under applied electric fields.

Similar experiments were performed for thin film TiO_2 devices; resistive switching observed in TEM and shown in Figure 3.7. High resolution (HR) TEM investigation reveals that the ALD TiO_2 film in the as-fabricated sample is polycrystalline with ~20 nm average grain size (likely anatase phase based on d-spacing measurements) as shown in Figure 3.8. Although the tracking of the microstructural change after the switching cycles has been examined with HRTEM imaging, no structural change such as Magnéli phase formation has been detected as opposed to the reported studies in which the devices were tested at significantly high dissipated power (~20 mW).[29,47]

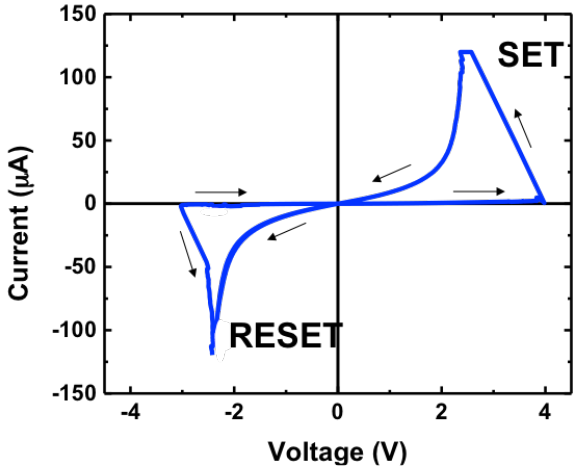

Figure 3.7 Switching *I-V* of thin film TiO_2 device while *in situ* biasing.

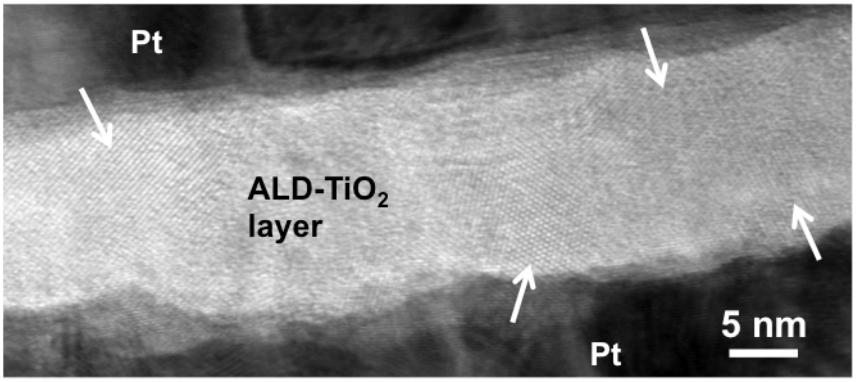

Figure 3.8 HRTEM image of ALD-grown TiO_2 layer sandwiched by Pt electrodes (dark contrast at top and bottom of the image), showing lattice fringes with multiple orientations along the length. Grains with multiple orientations are marked with arrows.

Figure 3.9 shows scanning TEM (STEM) high-angle annular dark field (HAADF) micrographs recorded before and after a SET process. These images provide qualitative information on local chemical compositional variations within the specimen. Using a camera length of 100 mm, higher atomic weight produces brighter contrast and allows Z-contrast imaging in STEM-HAADF mode.[72] The brightest contrast regions are the top

and bottom of the each image (Figure 3.9) and correspond to Pt TE and protective W layer. The ALD grown functional TiO_2 and TiN BE are seen as dark grey and light grey color. Figure 3.9(a) and (b) indicate a contrast change across the TiO_2 layer before and after the device undergoes SET process, respectively. The observed ~20 nm bright contrast (marked with an arrow) may indicate local structural/chemical changes in the individual grain associated with the SET process. Possible explanation for this bright contrast includes local oxygen deficiency and enhanced electron scattering to the HAADF detector. The following RESET process, however, does not exhibit a clear correlation with contrast changes. Thus, the observed contrast change may not be the indication of the conductive path location but some imaging artifact such as orientation changes due to the SPM probe motion during *in situ* biasing.

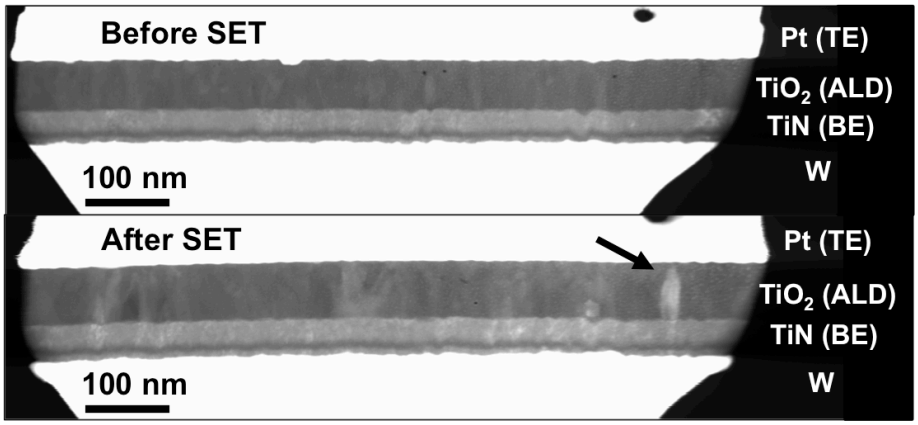

Figure 3.9 STEM HAADF images before and after SET processes.

Even though clear resistive switching was observed based on *I-V* measurements, no structural or chemical change was detected in the ALD-grown TiO_2 device. This result indicates the structural and chemical changes associated with resistive switching may be

too subtle to be tracked with conventional diffraction contrast and Z-contrast imaging. Strachan *et al.*[31] also reported that the secondary phase formation may not be the necessary process, but rather a subtle change in Ti/O ratio is more crucial for operation of their TiO_2-based RRAM devices. In the following chapters, new approaches to visualize the switching associated changes are proposed and discussed.

3.4 Summary and conclusion

In summary, electrical testing of TiO_2 -based RRAM devices showed evidence for oxygen vacancy migration under bias. The use of *in situ* biasing in the TEM obtained direct evidence of vacancy migration in the same device, at a specific spatial location during concurrent bias and TEM imaging. Resistive switching of the single-crystal TiO_2 devices was associated with Wadsley defect formation initiated from the TiO_2/TiN interface. The defects were observed to connect and disconnect during the SET and RESET processes within a 50 nm defect-free zone, which evidences the hypothesis of the present study. In thin film TiO_2 devices, no structural change (e.g. Magnéli phase formation) has been detected using HRTEM. On the other hand, a local contrast change with a 20 nm extent has been observed using STEM-HAADF. This contrast change can be an indication of chemical and structural changes associated with the switching event. However, it is not conclusive because the local contrast change has not been detected during the RESET transition. Also, the contrast change can be simply due to variation in diffraction conditions caused by a mechanical motion of the piezo-driven STM probe made contact to the specimen during *in situ* biasing. Thus, further studies are necessary to fully correlate switching behaviors to defect dynamics in TiO_2 and some new approaches

are presented in Chapter 4 and 5.

4 Oxygen vacancy creation, drift, and aggregation in TiO_2-based resistive switches at low temperature and voltage

This chapter describes experiments investigating defect dynamics in single-crystal TiO_2-based resistive switching devices, which is an extension of the work presented in Chapter 3. Since the structural change (extension and contraction of Wadsley defects (Figure 3.6)) associated with resistive switching was fast, it was difficult to capture the direction of the defect motion and define the exact voltage triggering them. Also, the causality of defect motion (either electrical or thermal origin) was not fully demonstrated. In this chapter, a series of constant low bias experiments were performed for TiO_2-based devices where Wadsley defect motion at low temperature has been tracked by coordinated *in situ* biasing and TEM diffraction contrast imaging. The contents in this chapter have been published in a peer-reviewed journal and some of the paragraphs have been directly quoted from the published work.[73]

4.1 Introduction

The interpretations of the electro-formation and resistive switching phenomena summarized in Chapter 2 are based on several elementary processes assumed to occur in the metal / insulator / metal (MIM) structures. The first of them is the creation of oxygen vacancies in the functional layer under bias. This process is attributed to electrochemical redox reactions at the oxide/anode interface.[8,14,24] When a doubly positively charged oxygen vacancy is created in TiO_2, two electrons are donated to the conduction band

leading to an increase in its conductivity during electro-formation.[24] It is important to note that the creation of vacancies in the accepted interpretation precedes current increase i.e. they are expected to form as the result of the electrochemical reaction rather than Joule heating due to the current flow. The second elementary process assumed to occur is oxygen vacancy drift in the applied field, leading to the accumulation of vacancies at the cathode. This is followed by the third important process: the reversible coalescence and dissociation of vacancies into and from an agglomerate. While there is ample evidence of the drift of oxygen vacancies at low temperatures, [28,74,75] the evidence for the other two processes is sparse and most of it is indirect.

The issue of vacancy creation in oxides by electrochemical reaction has been thoroughly reviewed by Jeong *et al*.[8] and Szot *et al*.[14] One group of experiments, nominally similar to electro-formation and switching, is induced electro-coloration and electro-degradation in bulk oxides.[27,74–76] The electrical bias applied at temperatures between 27 and 230^{o}C resulted in orders of magnitude decrease in electrical resistance. This resistance drop was attributed to redistribution of pre-existing oxygen vacancies under bias; none of the authors mentioned the creation of vacancies under applied bias. Observations in support of vacancy creation include the formation of gas-filled bubbles under the anode metal layer.[37,48] The effect was attributed to evolution of oxygen gas from the functional layer. It is clear, however, that this evidence is only indirect and the bubble effect is absent in most nanoscale devices. Lastly, Szot *et al*.[14] argued that vacancies were formed in bulk TiO_2 samples under low electrical fields (0.01 V/cm) and high, but unspecified, currents. The current flow in that experiment heated the sample to 500 °C, which is significantly

below temperatures where thermally induced reduction is expected to occur (>1000 °C).[77] It should be pointed out, however, that the sample was in contact with metallic leads, in which case, temperatures as low as 400 °C are adequate for significant oxygen loss in TiO_2.[78] Therefore, observed reduction and electrical resistance changes in oxides could have been of thermal origin.

The third process (reversible coalescence of vacancies into stable agglomerates and their dissolution) is an important feature of the switching process. Since the drift mobility and diffusion coefficient of isolated vacancies are proportional to each other, it is difficult to envision fast switching and long retention. This voltage-time dilemma[23,58] could be reconciled if ion transport becomes non-linear in high fields (accelerating switching)[59] or if oxygen vacancies form agglomerates (improving retention)[60]. One such vacancy agglomerate in TiO_2 are Ti_nO_{2n-1} Magnéli phases reported to be present in some electroformed and switched devices.[29,47,79] However, these observations were made on non-optimized structures exhibiting high temperature excursions during switching. The crystalline Ti_nO_{2n-1} phase can be an aftereffect of the high temperatures rather than their cause. In fact, later TEM investigations reported absence of Magnéli phases in switched devices.[31] Other than the observations of Magnéli phases at high dissipated power, there is no existing evidence of other types of agglomerates vacancies could form.

There is, however, ample evidence of vacancies forming agglomerates as a result of high temperature annealing. The periodically arranged three-dimensional vacancy aggregates i.e. Magnéli phases have been observed in samples prepared by annealing of non-

stoichiometric TiO_2+Ti mixtures at 1150 ^oC[80] or by melting of TiO_2 powder pellets at 1830 ^oC.[61,65] Annealing stoichiometric rutile crystals at temperatures up to 1000 ^oC in vacuum produced only disordered planar faults known as Wadsley defects.[81,82] The reverse process of dissolution of Wadsley defects during annealing in oxidizing ambient has also been reported.[83,84] The study by Kamaladasa *et al*.[70] attempted to test whether similar aggregation/dissolution processes can be induced by biasing the metal/single-crystal rutile/metal structure. While they reported formation of Wadsley defects and Magnéli phases, Joule heating was sufficient to raise the sample temperature above 800 °C, posing the question of their origin.

The series of experiments described below have a goal of documenting and quantifying all three elementary processes (vacancy creation, drift, and reversible coalescence/dissolution) involved in resistive switching in rutile by *in situ* biasing of metal / rutile / metal structures. Use of single-crystal rutile as the functional oxide has made it possible to analyze bias induced extended defect creation, which would be experimentally difficult in nano-crystalline materials. The objective of the present study is to definitively observe reversible coalescence of oxygen vacancies into extended defects and their dissociation under applied electric field but at low temperatures. The correlation of the switching *I-V* characteristics and particular morphology of structural changes is beyond the scope of this study. It is a worthwhile objective and some of this was the subject of previous publications.[70,85] However, the switching process in oxides induces large temperature excursions that are further exacerbated by the poor thermal

sinking of thin TEM foils. This does not allow for identification of the three elementary processes, which is the objective of this work.

Thus, the hypotheses of the present study are

I. Oxygen vacancies can be created, can migrate, and accumulate under a constant bias (at low power and temperature regime with absence of current run away event) and their motion depends on the polarity of applied bias.

II. Transformation between oxygen vacancies and Wadsley defects (vacancy agglomerates) is reversible.

4.2 Experimental: materials, TEM specimen preparation, and *in situ* biasing TEM setup

The functional oxide for the investigated structures was single-crystalline rutile (MTI Corporation (Richmond, CA)). A 100 nm thick Ti getter film was sputter deposited on the backside of rutile single-crystal substrates followed by annealing at 500 °C at 1×10^{-8} Torr for 1 hour. The annealing step reduced the crystal with the electrical conductivity increasing from 50 S/m to 250 S/m. This yields a doubly ionized oxygen vacancy density of 7.8×10^{18} cm^{-3} (assuming electron mobility of 1 $cm^2/V\bullet s$)[86]. A thin film stack composed of 80 nm TiN followed by 20 nm of Mo was sputtered as a bottom electrode (samples were inverted for TEM experiments). TEM specimens (about $2\times1\times1.5$ μm^3 in size) were lifted-out in FEI Nova 600 Nanolab focused ion beam (FIB) and affixed to W STM probe tips. The top electrode was an electron beam-assisted chemical vapor deposited (CVD) platinum layer by FIB. The slabs were then thinned down to electron

transparency (~ 150 nm) with 30 keV Ga^+ beam and finished with 5 keV polishing step (~100 nm). It is known that the 5 keV ion polishing step during sample preparation leaves a thin amorphous layer on the sample surfaces. The thickness of such a layer in single-crystal Si prepared in similar manner was estimated at 10 nm.[87] While this amorphous overlayer somewhat degraded the image quality, it still allowed for observation of structural changes in the device.

The *in situ* biasing TEM experiments were performed in the FEI Tecnai F20 microscope operated at 200 keV with a Nanofactory *in situ* biasing holder (single-tilt). Two-beam bright-field (BF) imaging was utilized to observe formation and evolution of extended defects. A schematic with the scanning TEM (STEM) high-angle annular dark field (HAADF) image in Figure 4.1 illustrates the *in situ* biasing TEM setup used in this study. Two W scanning tunneling microscope (STM) probes were mounted in the TEM holder facing each other. The stationary STM probe where the specimen was attached was electrically biased. The piezo-driven nano-manipulated STM probe was grounded in all experiments.

An Agilent Semiconductor Parameter Analyzer 4156C was utilized to apply quasi-DC sweeps and constant bias across the $Pt/TiO_2/TiN$ stack. The constant bias in this study refers to the source voltage and the device voltage (always lower than the source voltage due to a series resistor) represents the actual voltage across the device. A decrease in device voltage has been observed as the resistance of the device decreases over time (see Figure S4.1 in Supplementary Material). An external series resistor of 12 kΩ was

connected to the circuit to suppress current run away leading to rapid resistance changes in the device and thus helped to prevent large local temperature excursions.

The complete device structure attached to the W probe is shown in the scanning TEM high angle annular dark-field (HAADF) micrograph in Figure 4.1. Pt and TiN layers are seen as grey contrast, and considering the geometry in the image, these are referred to as top and bottom electrodes, respectively. In all TEM micrographs below, samples are shown in the same orientation as in Figure 4.1 with bias applied to the top electrode and the bottom electrode (contact made by a movable needle) grounded. This geometry allowed for observations of extended defect dynamics under bias.

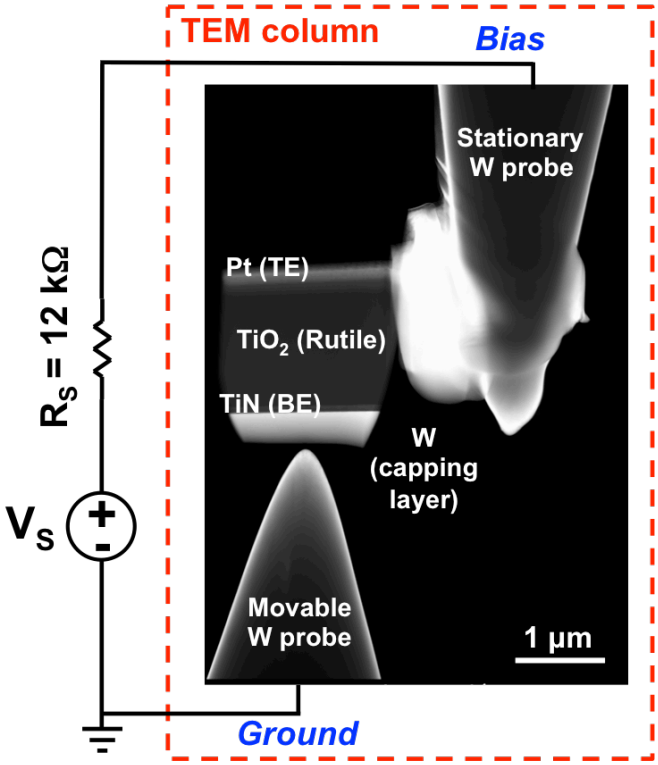

Figure 4.1 STEM-HAADF image of the Pt/TiO_2/TiN/Mo/W sample mounted on the W probe. The bright contrast between the sample and the W probe is the FIB-deposited Pt weld. Schematic diagram of electrical connections is included.[73]

4.3 Results

4.3.1 Microstructure changes under bias

Figure 4.2(a) shows a bright field (BF) TEM micrograph of an as-fabricated Pt/TiO_2/TiN/Mo/W sample before application of electrical bias. The electron-beam assisted chemical vapor deposited (CVD) Pt electrode and W protective layer are visible as dark areas at the top and bottom of the image. The single-crystal TiO_2 is sandwiched between the Pt and TiN layers. The gradual left to right contrast modulation in the TiO_2 layer is due to sample bending. The dark contrast along the TiO_2/TiN interface is

presumably a FIB-induced artifact during the Ga^+ ion beam milling. The TiN layer shadows the oxide, resulting in a continuous FIB damage layer on the TiO_2 crystal along the interface. Nevertheless, it is apparent that the TiO_2 layer initially is free of any extended defects, including any possible secondary phase inclusions, stacking faults or dislocations. The absence of dislocations is important as some authors argue for high dislocation densities near oxide surfaces as influencing resistive switching.[13,37] Figure 4.2(b) is a selected area diffraction pattern (SADP) at approximately the two-beam condition for $\boldsymbol{g}$=020 near the [100] zone axis, recorded at the center of the TiO_2 layer. The pattern is initially free of any streaking that would otherwise indicate the presence of Wadsley defects in the single-crystal TiO_2 layer. Thus, this SADP will serve as a reference to monitor structural changes in the functional TiO_2 layer during bias application.

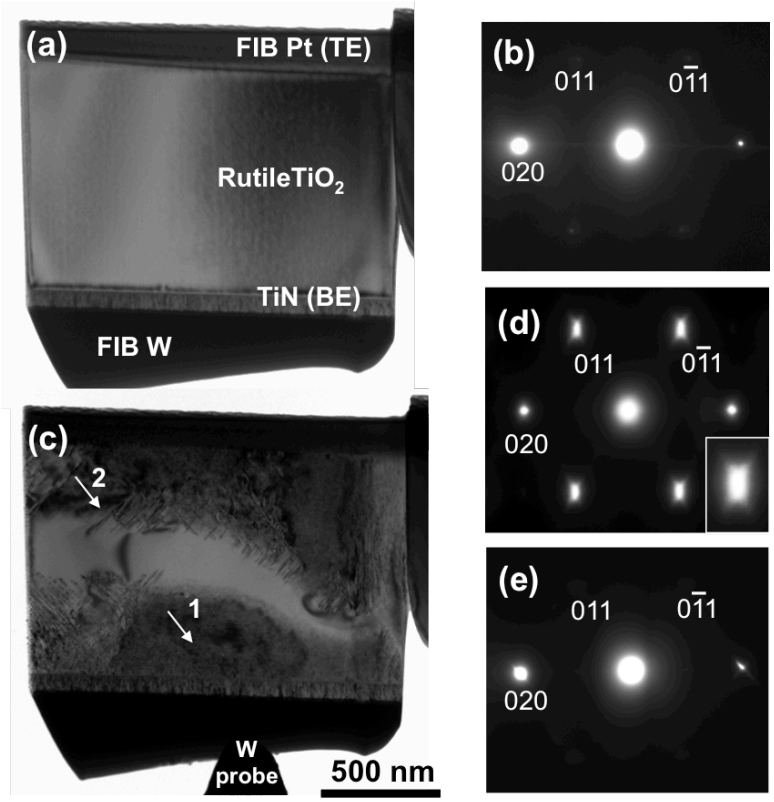

Figure 4.2 TEM bright field images of as-fabricated Pt/TiO_2/TiN device (a) and the same device after electrical biasing (c). (b), (d) and (e) are selected area diffraction patterns (SADP) close to two-beam condition for $\boldsymbol{g}$=020 near [100] zone axis. (b) corresponds to the as-fabricated structure while (d) and (e) were obtained from location indicated by arrows "1" and "2" in (c). The sampling size of the SADP aperture was a 200 nm diameter region.[73]

Figure 4.2(c) is a BF TEM image of the specimen after a series of quasi-DC sweeps and constant bias application with maximum device voltage of ± 1.5 V. (All plotted voltages are device voltages measured across the sample and do not include the drop across the series resistor). This voltage was below the forming voltage and at no point was there a rapid change of resistance, characteristic of the electro-formation process. The voltage

range and the series resistor has been deliberately selected to prevent current runaway, which can result in current localization and large local temperature excursions.[11] An example of the resistance change during biasing is shown in Figure S4.1 in the Supplemental section of this chapter. The maximum electric field in the device was 1.5×10^4 V/cm and the maximum power delivered to the device was less than 0.4 mW. This field is three orders of magnitude lower than that used by Strachan *et al.*[31] with the similar dissipated power. The resistance of the device decreased from 20 kΩ to 7.5 kΩ between Figure 4.2 (a) and 4.2(c). This resistance drop is similar to that observed during electro-degradation.[75] The change of contrast in the TiO_2 is apparent: two dark defect zones appeared in proximity to both electrodes with only a narrow strip of approximately 300-100 nm in width at the center of the TiO_2 remaining free of defects. The nature of the defects was determined from the SADP shown in (d) and (e). The pattern in Figure 4.2(d) obtained in the center of the dark contrast area (marked by an arrow "1" in Figure 4.2(c)) shows multiple {011} streaks. The streaking suggests presence of planar faults in the sample along (011) and $(0\bar{1}1)$ planes. The streaking depends on the location in the sample. For example, the SADP collected at the edge of the defect zone (marked by arrow "2" in Figure 4.2(c)) exhibits one dominant streak along the [011] direction indicating the presence of only one set of planar faults parallel to (011). The intensity of the streak is weaker than in Figure 4.2(d), consistent with the expected lower density of faults at the edge of the defect region. The appearance of streaks rather than discrete superlattice reflections[65] indicates a random rather than periodic distribution of faults. Planar faults in {110} planes of rutile are well known and have been analyzed in detail by TEM.[61] These defects correspond to missing {110} planes of oxygen atoms and are

referred to as Wadsley defects[65] The faults appear in rutile crystals reduced at temperatures above 1000 ^{o}C and are known to be created by coalescence of oxygen vacancies. The vacancies can also coalesce on {121} and {132} planes creating different families of Wadsley defects.[65]

The defect zones in Figure 4.2(c) extend along both electrodes roughly reflecting the expected distribution of electrostatic potential in the biased sample. The slight asymmetry could be due to differences in local temperature caused by the W probes acting as heat sinks and/or changes in sample thickness locally affecting thermal resistance. In most locations within the defect zones in electrically stressed samples, the defect densities were too high to resolve individual faults. The low fault density area at the edge of the defect zone in Figure 4.2 (c) is analyzed in more detail in Figure 4.4.

The identification of contrast as due to Wadsley defects is further supported by micrographs shown in Figure 4.3. Figure 4.3(a) is a bright field TEM micrograph of another specimen after a series of gradually increasing quasi-DC sweeps from 0 to -1.1 V (note: only negative bias was applied to the top electrode). The bias resulted in formation of only one defect zone in proximity to the top electrode (the diffuse dark bands in the middle and the right bottom of the TiO_2 are bend contours). In all experiments, the defects always appeared at the negatively biased electrode whether it was Pt or TiN. This behavior is consistent with faults formed by coalescence of positively charged point defects such as oxygen vacancies drifting in the applied electric field and accumulating close to the cathode as first suggested by Kim *et al.*[25] and later more widely accepted.[24]

The result proves one of the hypotheses (oxygen vacancy motion depends on the polarity of the applied bias) of the present study. The biasing was stopped at initial stages (lower field and shorter time than in Figure 4.2) and the individual defects can be resolved at the edge of the defect region. They appear as narrow lines along (121) traces on the surface of (100) oriented sample i.e. the image represents the planar (121) Wadsley defects viewed edge on. The morphology of the faults can be seen in Figure 4.3(c) obtained by tilting the specimen by about 15° around a vertical axis (α-tilt). The previously set of straight-lines, now appears as a series of two dimensional defects with striped contrast characteristic of planar faults.[72] All of the characteristics of defects observed in the samples appear to be consistent with those of Wadsley defects reported in reduced TiO_2.[65]

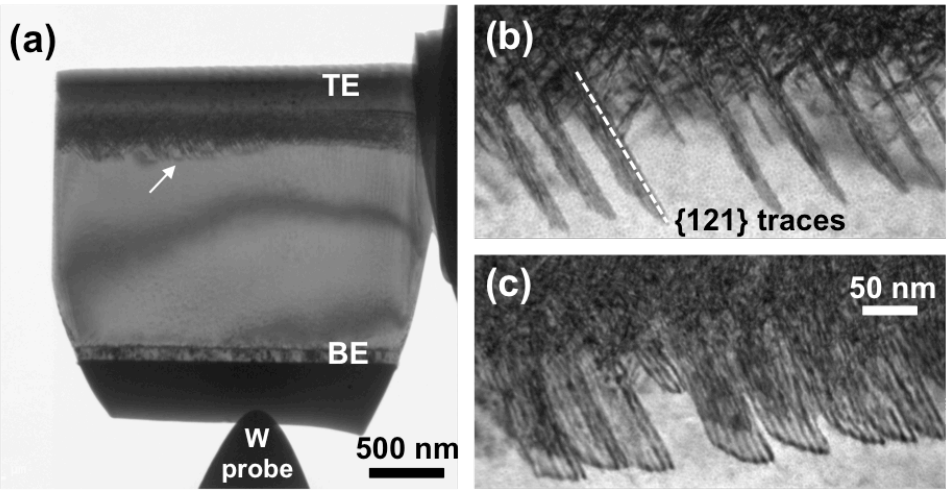

Figure 4.3 (a) BF TEM image of electrically stressed specimen at the early stages of defect formation (b) A magnified view of the region denoted by an arrow in (a). (c) The same location as (b) with the specimen tilted to better expose the defect planes.[73]

Wadsley defects, observed in current experiments, can form Magnéli phases if arranged in a periodic fashion.[61,88] Therefore, Wadsley defects can be considered an initial step toward creation of such Magnéli phases and in this sense current results are in agreement with those of Kwon *et al*.[29] Nevertheless, one needs to address the question as to why Magnéli phases were not observed even after prolonged biasing of the samples. The likely reason lies in the much lower dissipated power density in current structures. In experiments by Kwon *et al.*,[29] the current flow was restricted to a narrow filament with the maximum dissipated power during the RESET process of over 20 mW. The corresponding local Joule heating caused the temperature increase to be high enough to change the morphology of the top electrode and possibly melt it. The estimated temperature of the 200 nm diameter TiO_{2-x} filament with such power dissipation exceeds 3700 ^{o}C.[89] Formation of Magnéli phases in such conditions (T > 1500 ^{o}C) would be consistent with experiments of Bursill *et al*..[61]

It is apparent that there are no Wadsley defects or any other oxygen vacancy agglomerates in the rutile crystal of the as-fabricated structure shown in Figure 4.2(a). It implies that the concentration of oxygen vacancies is below the solid solubility limit which was estimated at x = 0.0015 in TiO_{2-x}[82] which corresponds to the vacancy concentration of 4.8×10^{19} cm^{-3}. The vacancy density estimated from measured electrical conductivity (assuming electron mobility value of 1 μm/V•s)[86] was 7.8×10^{18} cm^{-3}. It is also apparent that the vacancy concentration in the sample after electrical biasing exceeded the solubility limit causing the vacancies to precipitate out and form Wadsley

defects. Since the defected areas in the sample constitute over 80 % of the total sample volume (Figure 4.2(c)), one can argue that the total vacancy concentration exceeded total solubility. Also, the delivered power to the device during the biasing experiments is significantly higher than the oxygen vacancy formation energy in rutile TiO_2.[90] I can therefore conclude that oxygen vacancies were created under the experimental conditions. As the biasing progressed, the total number of vacancies in the sample gradually increased. This could be expected, since the ultrahigh vacuum (UHV) environment would not allow the oxygen atom to be replaced once lost. On the other hand, I have locally observed repeated processes of oxidation and reduction as the bias was reversed (Figure 4.4 below). The last step necessary to prove that vacancy creation was by electrochemical reaction (not thermal origin) is by performing a temperature estimate. This is discussed in detail in Section 4.5 with the conclusion that the temperature during current experiments does not exceed 150 ^{o}C. This is significantly below the temperature necessary to reduce TiO_2 in contact with a getter layer (~ 400 ^{o}C), providing the most compelling evidence so far for electrochemical reaction-induced creation of vacancies in resistive switching devices.

4.3.2 Coalescence and desorption of vacancies from planar faults

The typical testing method of switching devices employs quasi-DC sweeps with a pre-determined voltage range. At some point during the sweep, the resistance of the device rapidly changes during the SET and RESET events. Concomitantly, the filament is expected to change its length or cross section. This type of behavior was reported by Kamaladasa *et al.*: the rapid change of resistance was associated with major changes of

the microstructure (redistribution of Wadsley defects) in TiO_2.[70] While informative in their own right, such events are difficult to analyze from the perspective of the mechanisms involved since the electro-formation and switching events typically are associated with large local temperature excursions.[11,31,89] In this study, devices were biased at constant source voltage in order to eliminate such excursions and focus on effects of the electric field (the evolution of sample resistance under bias is shown in Figure S4.1 in the Supplemental section of this chapter). The evolution of Wadsley defects under constant source voltage was observed by TEM using $\boldsymbol{g}$=020 two-beam condition imaging. Figure 4.4 is the high magnification image of the region marked with arrow "2" in Figure 4.2(c). The images (a)-(c) show the same area of the sample with the two opposing regions of Wadsley defects. The micrograph in (a) corresponds to the starting time point with (b) taken after 300 seconds of -1.35 V applied to the top electrode. (Note that the voltage across the device decreased to -0.85 V during the experiment due to a change in the device resistance (see Figure S4.1 in Supplementary Material). Comparing the two images, it is apparent that Wadsley defects (dark straight lines) at the top defect zone extended downward, narrowing the gap. The faults increased in length by an average of 135 nm. Since the faults are non-conservative (they change local composition of the material) with the displacement vector out of the plane of the fault,[88,91] such extension must be associated with the absorption of oxygen vacancies. The process occurs one vacancy at a time attaching to the edge of the missing plane of oxygen ions; crystallography of the process is described by Anderson and Hyde[91] and Bursill and Hyde[65]. The defect zone in the lower part of the specimen could serve as the reservoir of vacancies.

In fact, close comparison of the same pair of micrographs indicates that the faults at the edge of the bottom defect zone retracted somewhat (~20 nm). The bottom faults changed contrast from continuous lines (Figure 4.4(a)) to "dashed" lines (Figure 4.4(b). Explanation for the behavior of the faults in the lower defect zone is not immediately obvious. One could expect the vacancies to desorb from the edges of Wadsley defects. Such a process, if repeated, would result in a gradual contraction of the fault and would be the exact opposite to the fault extension occurring in the upper defect zone. Rather than this, the contrast change indicates the planar faults break up into numerous smaller defects with sizes of about 10 nm lying in the same plane and giving a "dashed" line appearance. While this behavior effectively lowers the fault area and the total number of vacancies aggregated into faults, it increases the length of partial dislocations bounding the faults. Observation of similar contrast associated with thermal dissolution of Wadsley defects has been reported by Blanchin and Bursill.[83,92] Specifically, these authors reported Wadsley defects dissociating into dash-like "small defects". The structure of these is likely that of a disc of vacancies bound by the dislocation loop. This assertion is supported by the image in Figure 4.4(d) obtained by tilting the sample by about 15 degrees about the vertical axis (α-tilt). The small defects produce a characteristic "coffee bean"-like contrast that is known to correspond to strain contrast of a small dislocation loop.[93] It was impossible to determine the Burgers vector and the plane normal of the loops due to the limited tilt of the single-tilt axis TEM holder. Wu *et al.* reported observation of the similar dislocation loops in annealed $BaTiO_3$ and found the loops are vacancy type by extensive $\boldsymbol{g \bullet b}$ analysis.[94] The incomplete retraction of defects under bias can have important consequences for the endurance or reliability of switching

devices. Leaving “remnants” behind the retracting faults would lead to slow accumulation of vacancies, gradually affecting the device characteristics and even result in eventual RESET failures. It should be noted here that the extension and retraction of faults has been observed repeatedly upon reversal of the bias polarity. This corresponds to repeated local oxidation and reduction of the sample.

The image shown in Figure 4.4(c) was obtained after application of positive 1.15 V bias for 300 seconds (compared to Figure 4.4(b)). Similar to the negative biasing, a voltage drop to 0.76 V was observed during the experiment. The changes of the microstructure are basically the reversal of the changes between images (a) and (b). Since the temperature during the experiments did not exceed 150 ^{o}C (see Section 5), this image series proves that vacancies can detach themselves from the Wadsley defects under the influence of the electric field. Also, it is quite obvious from Figure 4.4(a)-(c) that the vacancies drift in the electric field and coalesce to form and reform faults. This proves the second (oxygen vacancy drift) and the third (reversible coalescence of vacancies into stable agglomerates and their dissolution) elementary processes responsible for resistive switching do occur.

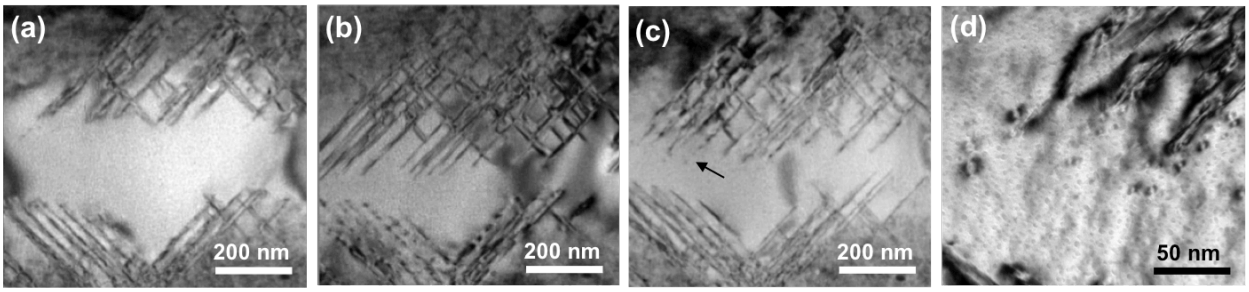

Figure 4.4 High magnification TEM images of the region marked by arrow "2" in Figure 2(c) during *in situ* constant bias stressing. (a, b) Max. V = -1.35 V applied between (a) and (b) for 300 s. (b, c) Max. V = +1.15 V applied between (b) and (c) for 300 s. (a, b) Growth of the top defect zone and dissociation of the bottom defect zone. (b, c) Dissociation of the top defect zone and growth of the bottom defect zone. (d) Magnified views of arrowed region in (c) showing dislocation loops (coffee bean-like contrast) near the end of the Wadsley defects. The small (<5 nm) grey speckles shown in Figure 4.4(d) are to be believed Ga droplets with Ga deposited during the FIB sample preparation and aggregated during the experiment.[95] Note that the specimen was tilted when imaging (d).[73]

4.3.3 Temperature estimates

Based on previous studies and available literature results, the field of resistive switching generally attributes the type of processes observed in the previous sections to be thermally activated. The device temperature is of importance for the current study as I intended to decouple defect dynamics due to temperature and voltage. In order to estimate the temperature changes due to Joule heating, a 3-D heat flow simulation was performed using COMSOL Multiphysics® package. Built-in ‘electric current’ and ‘heat transfer in solids’ modules were coupled for the steady-state simulations. These modules solve the heat diffusion equation and Maxwell’s equations simultaneously to yield a self-

consistent temperature estimate. Figure 4.5 shows the thermal profile of the simulated device. For the calculation, the maximum applied electrical bias of 1.35 V during *in situ* biasing experiment was applied. The peak temperature reached is 143 °C and this would represent the highest temperature reached during the entire series of *in situ* biasing experiments presented in Sections 4.3 and 4.4. The temperature near the location where the concurrent growth and dissociation of Wadsley defect occurs is 107 °C, which is significantly lower than thermal reduction temperature (>1000 °C). Materials parameters used for the calculation can be found in supplementary information (S2).

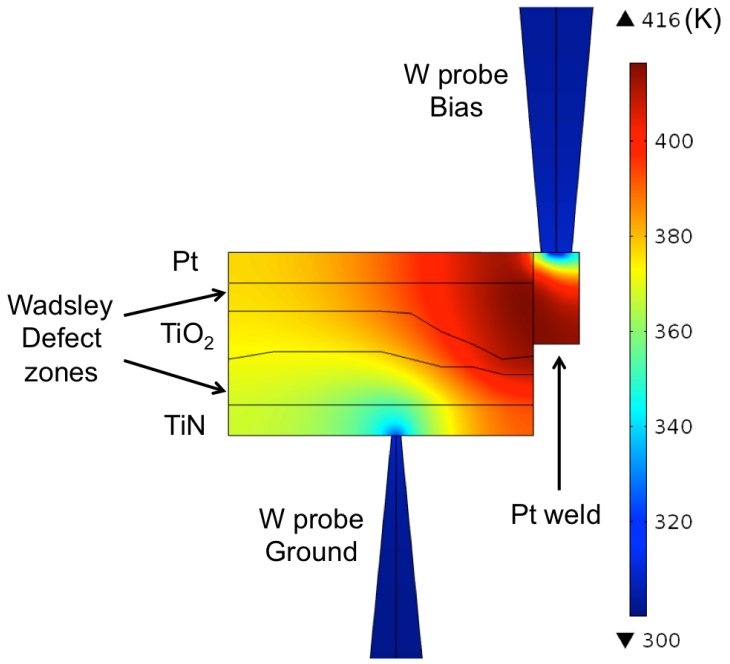

Figure 4.5 The temperature profile of the specimen during the *in situ* biasing experiment performed via COMSOL Multiphysics®. The peak temperature is 143 °C (416 K). Note that the temperature near the location where the concurrent growth and dissociation of Wadsley defect occurs is lower (107 °C (380 K)) than the peak temperature.[73]

4.4 Discussion

It is quite clear from Figures 4.2-4 that the vacancies / Wadsley defects never formed a small diameter filament. The defect zone boundaries in the samples are roughly parallel to the two electrodes and do not approach each other by less than 50 nm. This is in stark contrast with the expectation that the filament is more or less cylindrical with the diameter in the 1-10 nm range.[21,29] The possible origins of the different "filament" shape could be a difference in field strength, and a different sample geometry compared to standard switching devices: the large thickness of the oxide, relatively flat interfaces between electrodes and the oxide, and very different heat sinking. Another significant difference is the proximity of the sample surfaces making it easy for the oxygen ions to leave the functional layer. It is anticipated, however, that this is not a dominant effect as the TEM micrographs show the defect distribution being uniform throughout the sample thickness. The non-uniformities are rather associated with the electrodes as seen in the micrographs. Many of these differences are unavoidable consequences of the *in situ* experiment. Also different were electroforming/switching procedures used in current experiments. Typically, electroforming and switching are induced using a quasi-DC voltage sweep. At some point during the sweep, the resistance changes rapidly due to electronic instabilities of the structures. As shown by Sharma *et al*.,[11] the TaO_x-and TiO_x-based devices exhibit negative differential resistance in part of their *I-V* characteristics. This leads to a rapid spontaneous constriction of current flow, local Joule heating and formation of a small diameter filament. The MIM structures used in this experiment do not show such *I-V* characteristics.

The values of the voltage used in current experiments causing the vacancy formation and redistribution are small (1-2 V). They are, however, in the same range as electroformation and switching voltages reported in a number of devices based on TiO_2[48,89], Ta_2O_5[96], or HfO_2[15]. It is also widely accepted that the operating mechanism is the electrochemical reaction. The energetics of such reactions remain to be worked out and will likely require a much better understanding of the electrostatic potential distribution in switching structures.

Lastly, the question arises whether the process reported here could be active in typical switching devices comprising amorphous or nanocrystalline functional layers. It can be argued that this is indeed the case. While the amorphous oxide films lack long range order, they have a short range one. It is easy to imagine formation of oxygen vacancy clusters in amorphous materials that correspond to Wadsley defects in single-crystals of rutile. This can be plausible by first considering that the Wadsley defect corresponds to transitions between edge-sharing octahedra in the stoichiometric crystal to face-sharing ones.[62] This preserves the coordination of all atoms affecting only farther neighbors; such change can easily occur in amorphous or nanocrystalline materials. Of course, the coalescence in a single-crystal occurs on a well-defined crystal plane and the resulting defects have a large spatial extent. In amorphous or nanocrystalline material, the planes will not be well defined and the size of vacancy clusters is likely limited, reminiscent possibly of "small oxygen vacancy defects" reported by Blanchin and Bursill.[83,92] It is quite apparent that the local structure of such defects can be almost identical in single-

crystals and amorphous films. In both materials, the net electrical effect of the oxygen deficiency is very similar: titanium will retain more of its electrons populating the states in the conduction band and increasing the local electrical conductivity.

The lateral size of the Wadsley defects seen in Figure 4.3 is over 100 nm. Clearly there are no well-defined planes of this size in amorphous materials. As a consequence, the vacancy agglomerates would have to be smaller. It is well documented that vacancy agglomerates even in single-crystals come in a continuous distribution of sizes with clusters reported as small as just several anion vacancies.[83,92,97] It appears then quite possible to form similar clusters in either amorphous or nano-crystalline thin films.

Another important aspect of current observations is the relatively low value of electric field causing creation, drift, and coalescence of vacancies (~ 1×10^4 V/cm). A 10 mV *Read* pulse applied to a 10 nm thick oxide layer would induce fields well in excess of the fields used in current experiments. Therefore, the defect dynamics reported here can be important under *Read* and *Disturb* voltages for nanoscale RS devices. Also, the observation of residual dislocation loops (coffee bean-like contrast) near the end of the Wadsley defects, as shown in Figure 4.4(d), is quite important. These dislocation loops represent incomplete retraction of the Wadsley defects caused by the field reversal, thus indicating a possible mechanism for RESET failures after endurance cycling. Indeed, the *Read* and *Disturb* phenomena and device failure mechanism are one of the active research topics in the resistive switch field because they are directly related with the reliability issues that may prevent the eventual commercialization of RRAMs.

4.5 Conclusion

Electric field-induced defect reactions have been investigated in a prototypical resistive switching system consisting of single-crystal rutile TiO_2 sandwiched between Pt and TiN electrodes. Careful biasing limited the Joule heating of the specimens to no more than 150 °C. Three elementary processes (creation, drift, and reversible coalescence / dissociation of vacancies) essential for the functioning of resistive switching devices have been documented by direct *in situ* biasing TEM observations.

Oxygen vacancy creation at the applied electric field of 1.5×10^4 V/cm was observed as the increase of the vacancy content above the solid solubility limit of x=0.0015 in TiO_{2-x} throughout most of the TiO_2 volume. The vacancies coalesced into planar defects on {110} and {121} planes referred to as Wadsley defects. Repeated bias sweeps of both polarities created two defect zones adjacent to both electrodes. Upon changing the bias polarity, the extended faults near the anode dissociated and contracted by emission of oxygen vacancies. The point defects drifted in the applied field, attached themselves to the edges of faults in the defect zone near the cathode, and agglomerated so that fault lengths were extended.

Thus, I have extended a methodology demonstrated by Yang *et al*.[98] in the case of the conducting bridge mechanism to devices exhibiting valence change mechanism. The dynamic defect analysis in this model system can contribute to further understanding of resistive switching mechanisms for TiO_2-based RRAM and also in other non-

stoichiometric transition metal oxide systems. Specifically, this sheds light on the possibility of creation of oxygen vacancies at low-biases and temperatures that are conditions akin to *Read* and *Disturb*. Moreover, incomplete retraction of defects in presence of field also indicates this as being a possible mechanism for RESET failures after endurance cycling.

Supporting information

S4.1 Resistance evolution during biasing

Biasing was performed using constant source voltage of -3.5 V with the resistor of 12 kΩ connected in series with the device. The initial voltage drop across the sample was -1.35 V and it decreased to -0.85 V at the end of the stress. The evolution of resistance during the stress is shown in Figure S4.1. It is important to note that the changes are gradual rather than rapid as is characteristic of the SET switching process.[15] The conditions have been selected intentionally this way to prevent runaway processes with uncontrolled temperature excursions.

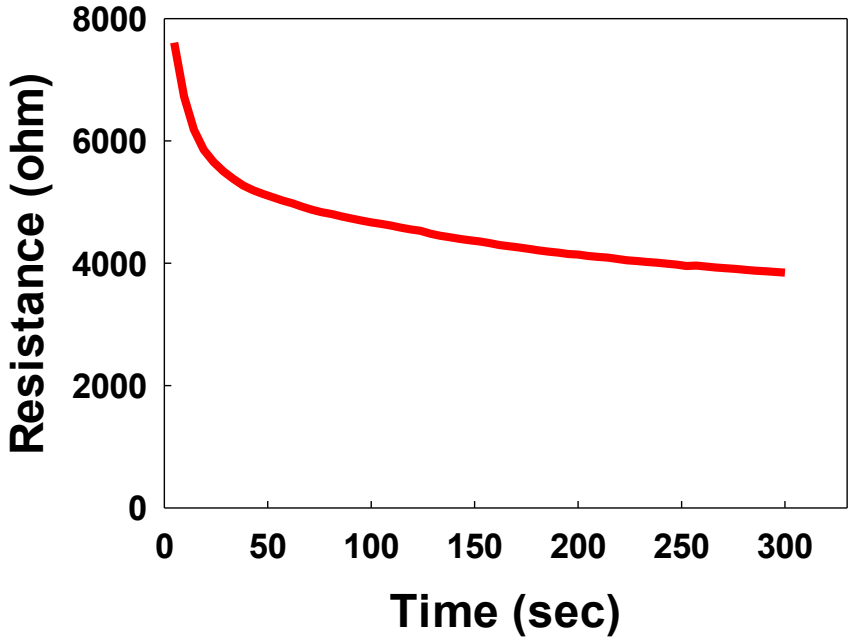

Figure S4.1 Resistance versus time profile showing a decrease in voltage across the device as the resistance of the device decreases over time (300 seconds) during the constant biasing (V_{SOURCE}=-3.5 V).

S4.2. Simulation for temperature estimation

The estimate of the sample temperatures was obtained by a 3-D heat flow simulation using COMSOL Multiphysics® package. The 'electric current' and 'heat transfer in solids' modules solve the heat diffusion equation and Maxwell's equations simultaneously to yield a self-consistent temperature estimate.

The oxide volume was divided into three parts with different electrical conductivities. The two Wadsley defect zones next to both electrodes were assumed to be highly conductive with conductivity of 3300 S/m. This corresponds to conductivity of TiO_x with the concentration of vacancies at the solid solubility limit and electron mobility of 1 $cm^2/V\bullet s$. The two zones are marked in Figure S4.2 below. The defect-free zone in the center of rutile crystal was assumed to have electrical conductivity of 250 S/m (the same as the measured value of conductivity in as-fabricated structure). These assumptions gave the correct value of current measured during the experiment i.e. the power dissipated in the sample in the simulation corresponded to experimental value of power. For the calculation, the maximum applied electrical bias of 1.35 V during the *in situ* biasing experiment was applied. The thermal and electrical conductivities for all materials are listed below in Table S4.1:

Table S4.1 List of parameters for COMSOL model used to produce Figure 4.5

Material	Electrical Conductivity (S/m)	Thermal Conductivity (W/m-K)
Pt	200 (measured, deposited electron beam assisted CVD by FIB; has organic inclusions)	1.0 (limited by organic inclusions)
TiN	1.6×10^6 (measured)	11.7 (Wiedemann-Franz law)[99]

TiO_x (Wadsley defect zones)	3300	11.0 (bulk)
TiO_x (as deposited)	250	11.0 (bulk)
W (needles)	1.887×10^7	172

The COMSOL model uses the non-uniform power generated in the sample as the source of Joule heating. Thus, the temperature at each discretized point can be obtained. For boundary conditions, the temperature was assumed to be 300 K at the base of both tungsten probes, as shown in the Figure S4.2.

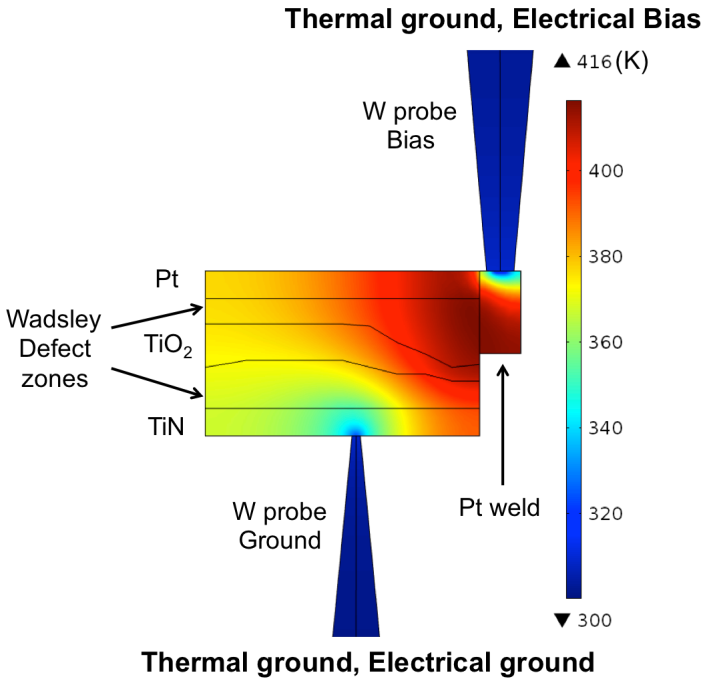

Figure S4.2 Thermal and electrical boundaries imposed on the W probes. Note that both W probes were set to thermal ground.

It must be noted that the temperature in the as-fabricated sample is much lower than the sample with defects. This is mainly due to the fact that the resistance of the pristine sample is much higher (all regions have electrical conductivity of 250 S/m) than the resistance of the sample with defects.

5 Transient thermometry and HRTEM analysis of filamentary resistive switches

Up to now, structural changes in single-crystal RRAM devices have been discussed, which provided useful insight on resistive switching mechanisms. In general, however, single-crystal RRAM devices are not commercially viable. Therefore, most current research focuses on thin film RRAM devices to understand the underlying switching mechanisms and improve their performance. As mentioned previously, the physical switching mechanism remains an active research area in this community. The actual RRAM devices generally have thin film stacks of 5-10 nm thick functional oxides sandwiched by 20-30 nm thick metal electrodes. Among various functional oxide systems, HfO_x and $HfAlO_x$-based RRAM devices are selected and characterized using electron microscopy techniques in this chapter. The contents in this chapter have been published in a peer-reviewed journal and some of the paragraphs have been directly quoted from the published work.[100]

5.1 Introduction

Hafnium oxide (Hafnia, HfO_x) has been extensively studied for high-k dielectric gate insulators to improve complementary metal-oxide-semiconductor (CMOS) performance.[101–103] Recently, HfO_x have drawn attention as a potential functional oxide layer in RRAM devices.[9,15,104,105] It has been reported that HfO_x-based RRAM devices show outstanding switching performance such as switching speed (~ ns), superior

endurance (> 10^{10} cycles) low-energy operation (< 0.1 pJ), and excellent scalability (10×10 nm^2) among various binary oxide-based devices.[43] Furthermore, it is known that the HfO_x with Al content enhances device performance; increasing endurance and uniformity.[106,107]

The filamentary switching model previously mentioned is also widely accepted for HfO_x-based RRAM resistive switches, in that the electroforming event triggers formation of conductive filaments and the resistivity can then be modulated by shunting and rupturing the filament.[15,21,46,108] However, since no electrically conductive phases are known in the Hf-O system, the description of the conductive filament is slightly different to the one in TiO_x-based RRAM devices (i.e. homologous series of Magnéli phases (Ti_nO_{2n-1})[14]).

Larentis *et al*.[21] suggested a numerical model describing resistive switching events in HfO_x-based RRAM devices based on voltage-driven ion migration. They assumed the conductive filament is a sub-stoichiometric HfO_x locally doped by shallow donors (concentration of 1.2×10^{21} cm^{-3}) such as oxygen vacancies or hafnium metal interstitials, increasing electrical conductivity by changing the Fermi level positions within the conductive filament region. According to the model, metallic conductive filament connects the two metal electrodes (Figure 5.1(a)), causing Ohmic-type characteristics during the SET transition. On the other hand, during the RESET transition, a depleted gap is created, resulting in high resistance state as shown in Figure 5.1.

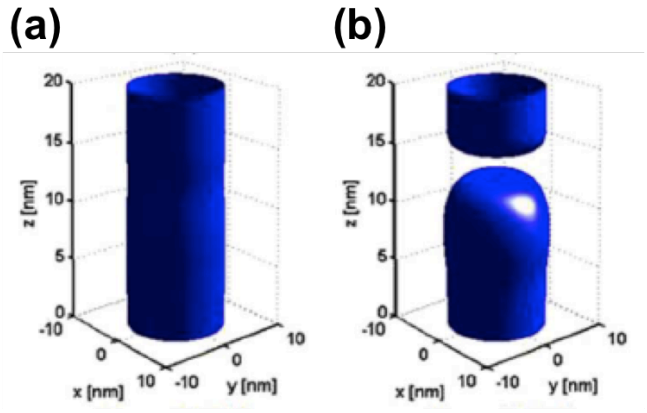

Figure 5.1 Three dimensional schematics of conducting filament (a) at low resistance (ON) state and (b) at high resistance (OFF) state.[21]

Degraeve *et al*.[104] demonstrated the SET and RESET transition with a dynamic "hourglass" model. The conductive filament is assumed sub-stoichiometric HfO_x that has an hourglass shape: two oxygen vacancy reservoirs near the HfO_x/metal electrodes interfaces and a constricted area in between as seen in Figure 5.2. The SET/RESET operation is explained by changes in constriction width by oxygen vacancy migration under applied bias.

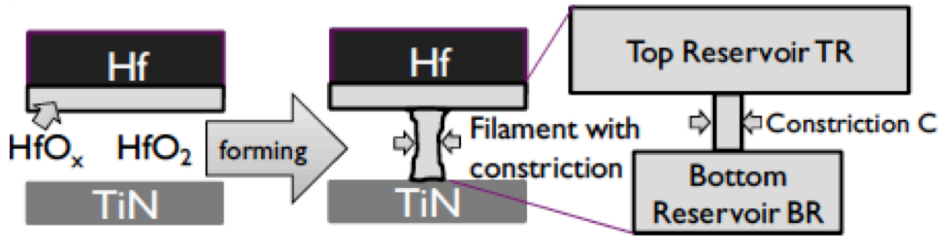

Figure 5.2 Schematic diagrams showing a dynamic "hour glass" switching model.[104] Forming creates an oxygen vacancy rich filament, consisting of top and bottom oxygen vacancy reservoirs connected by a constriction with variable width.

Although there has been a large body of research conducted to quantify the processes involved in resistive switching, many of the aspects of the process remain unclear. The most important is the nature of the structural change that makes the filament conducting. In HfO_x, along with other wide band gap oxides such as TaO_x and TiO_x, the switching is attributed to redistribution of oxygen vacancies by the applied electric field. Accordingly, the filament in the reminder of this chapter will be defined as the small diameter cylinder composed of reduced conducting oxide. Such a filament is nonvolatile and retains its properties after the bias is terminated. Its three fundamental parameters are the diameter, the composition (vacancy density) and the temperature it reaches during switching.[9] As pointed out below, the close-to-stoichiometric oxide surrounding the filament can conduct significant current density when heated. This is not considered as part of the filament.

Since resistive switching behavior is directly tied to the characteristics of the underlying filaments, methods for estimating their size are of fundamental importance and have been the topic of ongoing research. By determining the filament size, a deeper insight into the switching mechanism can be gained that will then enable the engineering of superior devices. There are large differences in filament size estimates in the literature. Some experimental results place the filament size in the 100 nm and over range by using a variety of characterization tools: transmission electron microscopy (TEM),[47] X-ray spectroscopy,[31] and atomic force microscopy (AFM).[24,48] However, device scaling suggests that filaments are below 10 nm in diameter.[43] This dimension has also been

assumed by most modeling efforts.[21,96,109] While assumptions are not equivalent to evidence, the modeling produced a self-consistent picture of both the SET and RESET processes as being due to the thermally activated motion of oxygen vacancies.[21] A change from 10 nm to 100 nm filament diameters would result in the filament temperature lower by hundreds of degrees at the given dissipated power and virtually freeze the motion of vacancies, making these models unfeasible. On the other hand, some of the TEM results[29] and AFM-based tomography[69] indicate the filament size at about 10 nm.

Although the above results appear contradictory, it is possible that the filament size in different devices formed in different conditions vary widely. Most of the experimental data mentioned above have been obtained from devices that have dissipated significant power during SET (≈ 20 mW).[14,29] Notable in this respect is the paper by Kwon *et al*..[29] While the structural features analyzed by HRTEM indicated the Magnéli phase inclusion of about 10 nm diameter, the crater formed by the electroforming process was about 10 μm and in concert with the level of dissipated power. HRTEM cannot analyze features of this size and by necessity the images showed only a small fragment of the entire crater possibly missing some of its parts. Recently fabricated devices formed with a low current compliance achieved by on-chip transistors and dissipated power of (10 - 20 μW) are likely to form a much smaller filament.[43] However, these results do require experimental verification.

The important consequences of the filament size are the filament temperature generated during switching and the consequence for the ultimate scaling limit. Clearly, the high temperature expected in small diameter filaments would affect the reliability of switching devices.[110] On the other hand, high temperatures are necessary to achieve fast switching.[21,96] The estimates of the filament temperature so far have largely relied on simulations that make a number of assumptions about the conductivity, size, and geometry of the filament.[22,33,96]

In the present work, I have attempted to resolve the contradictions among recent studies by performing a detailed electrical and high-resolution microstructural analysis of nanometer scale devices with on-chip ballast. All devices used in this study dissipate orders of magnitude lower power than the above examples and exhibit stable switching. High-speed pulsed thermometry was used to estimate the temperature excursions in nanoscale RRAM devices based on *I-V* characteristics and the physical picture was validated by direct evidence of microstructural changes in the form of local crystallization.[11,18] This work uniquely juxtaposes HRTEM with thermometry to provide insights into: (1) the interplay between the device size (nanoscale) and the filament heating in devices that operate at powers much more relevant in RRAM applications; (2) identify the peak temperature - limiting mechanisms in the RRAM cell; (3) validate these mechanisms and thermal excursions through the use of direct HRTEM studies; and (4) confirm the role of power compliance on filament size and thermal excursions. The results indicate that the filament diameter was overestimated by more than an order of magnitude while its temperature was greatly underestimated.

5.2 Experimental

In order the track the switching induced local crystallization, $HfAlO_x$-based RRAM devices are selected for the current study. The microstructure of pristine HfO_x and $HfAlO_x$ were found to be nano-polycrystalline and amorphous, respectively. Since it is difficult to track the local crystallization for the HfO_x due to the initially existing nanocrystals, the HfO_x based device has been excluded (see Appendix A).

5.2.1 Materials

Crossbar devices with stacks consisting of TiN (40 nm) / $HfAlO_x$ (5 nm) / Hf (10 nm) / TiN (30 nm) have been fabricated on SiO_2/Si substrates. The details of the device configuration and DC switching *I-V* are in Figure 5.3. The functional $HfAlO_x$ layer was deposited via atomic layer deposition and the bottom TiN and the top Hf/TiN electrodes were sputter deposited. The Hf layer acts as an oxygen getter layer that allows formation of the oxygen deficient, sub-stoichiometric $HfAlO_x$ functional layer, facilitating creation of the conductive filament under applied electrical bias. The active area of the devices is defined by the region where the bottom and the top electrode overlap. All devices were encapsulated by a 30 nm Si_3N_4 and a 200 nm SiO_2 passivation layer. The device size used for the current study was nominally 85×85 nm^2 unless specified otherwise.

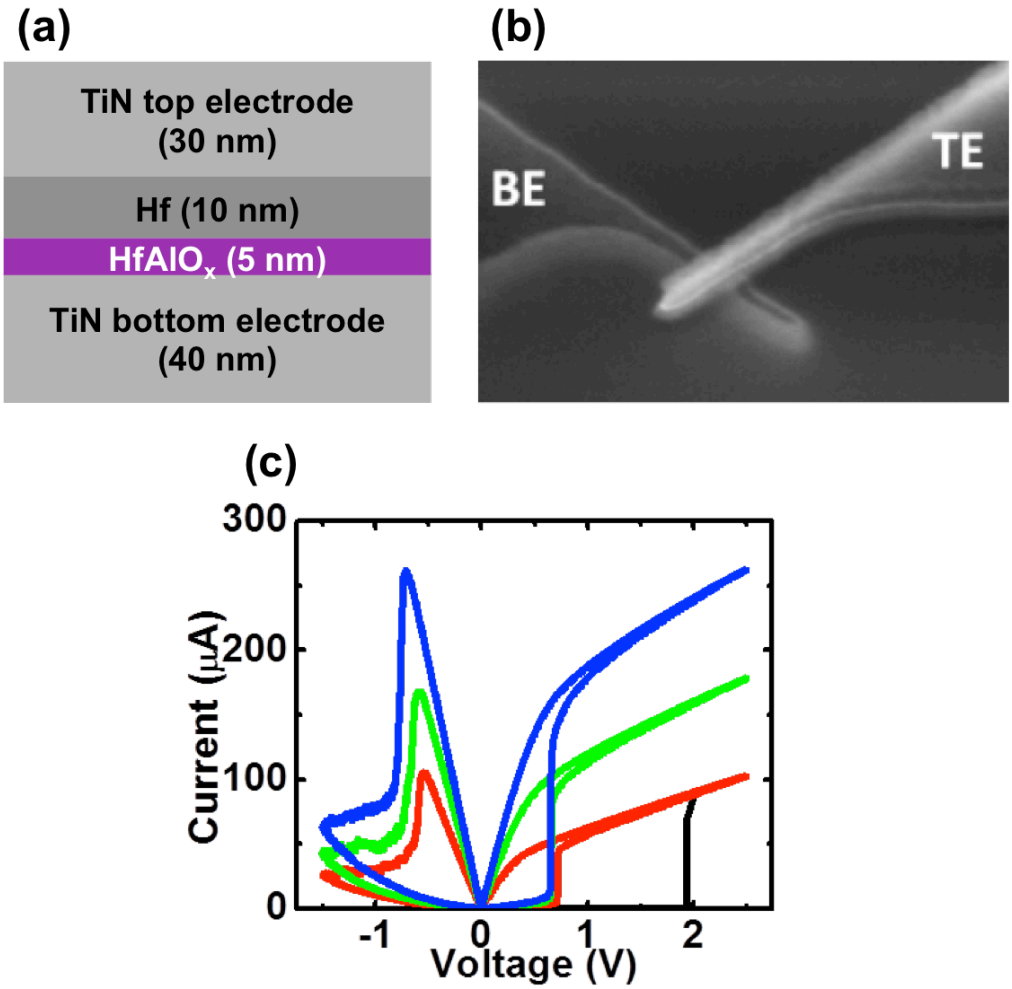

Figure 5.3 (a) Schematic diagram of RRAM device stack. (b) Scanning electron microscopy (SEM) image of crossbar RRAM device. (c) DC forming and switching *I-V* characteristics of the devices at different compliance current at forming (blue: 200 μA, green: 100 μA, red: 50 μA) on a linear scale (the sign of the current at negative bias is converted to the absolute values). Note the nearly linear *I-V* characteristics in the LRS.[100]

5.2.2 Electrical testing

Thermometry of the devices was carried out by collecting the pulsed *I-V* characteristics as a function of stage temperature. This was accomplished by launching ultra-short (80 ps) pulses to the device in Ground-Signal-Ground configuration along a 50 Ω

transmission line.[33] The voltage and current across the device were extracted using a time domain transmissometry setup[111] detailed in the Figure S5.1. The pulsed *I-V-T* characteristics obtained in this way are not affected by the self-heating of the device and can be used as a look-up table for interpretation of the DC characteristics.[33] The pulsed *I-V* characteristics were also used to determine the temperature coefficient of resistance (TCR) of the filament at ≈ 0.16 %. This value is consistent with the TCR of metals with poor electrical conductivity[112] and was used in electrothermal simulations to implement self-consistency between electrical and thermal domains.

5.2.3 Electro-thermal simulation

Finite element simulations using the COMSOL package were carried out making similar assumptions to those used in the previous works.[11,33] In addition, one of the significant deficiencies of past approaches has been addressed. Specifically, a thermal boundary resistance (TBR) at the metal/oxide interface has been included, which is crucial in understanding the high-temperature excursions that cause current spreading in RRAM device at high-powers. A TBR of 200 MW/m^{2}K typically exists between metals and semiconductors/insulators because the mode of heat transfer in metals (electrons) is fundamentally different from that of semiconductors/insulators (phonons).[113] At the interface, heat transfer between the oxide and the metal occurs only via phonon exchange with the temperature increase of the metal electrode lattice resulting in subsequent increase of the electron gas energy. The mismatch at the interface manifests itself in the form of TBR.[113] In current system, the TBR diminishes the vertical heat flow from the filament to the electrodes, which increases the local temperature of the filament. This, in

turn increases the lateral heat flow, resulting in significant heating of the oxide surrounding the filament and its electrical conductivity. As the consequence, the current spreads outside of the filament. In order to accurately simulate this effect, the pulsed *I-V* characteristics of an as-fabricated unformed device have been measured as a function of stage temperature, as shown in Figure 5.4.

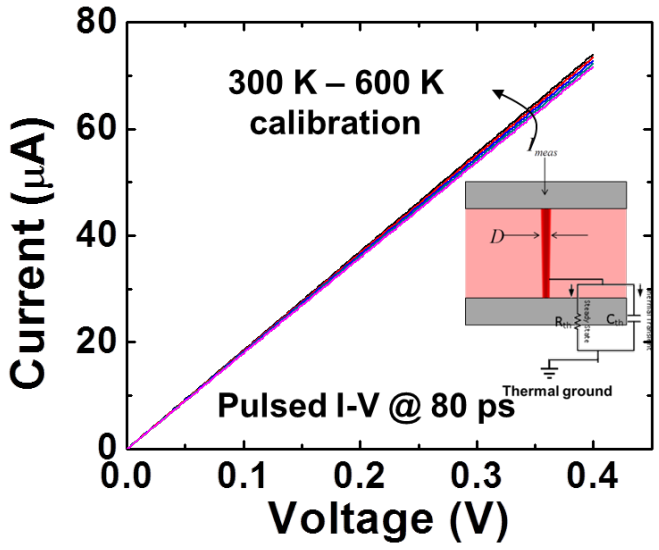

Figure 5.4 Pulsed *I-V* characteristics as a function of stage temperature for RRAM devices in low resistance state (LRS). Inset shows the thermal circuit that determines the temperature. A fast transient shunts the thermal current (electrical power) through the thermal capacitor, thus increasing the temperature only slightly.[33]

The *I-V* characteristics show a current with a non-linear dependence on both voltage and temperature. This *I-V-T* surface was fitted and used as the conductivity $\sigma(V, T)$ of the oxide surrounding the filament in the simulation. Also it is assumed that thermal properties of the amorphous and crystalline $HfAlO_x$ are the same, as the reported thermal

conductivity values in typical oxide (for example silica) thin film ranges from 1.1-1.4 W/m-K.[114,115] Moreover, changing the thermal conductivity of the surrounding region does not significantly affect the thermal resistance (and consequently temperature) seen by the filament, due to the heat dissipation occurring mostly through the electrode to thermal ground.

5.2.4 Microstructure analysis

The TEM assessment of microstructural changes was performed on crossbar type devices shown in Figure 5.3b. Electron transparent TEM specimens were fabricated using a FEI Nova Nanolab 600 dual-beam focused ion beam (FIB) system equipped with an Omniprobe *in situ* lift-out capability. Membrane samples about $4\times1.3\times2$ μm^3 in size were milled out using a 30 keV Ga^+ ion beam. The membranes were then transferred to Omniprobe copper grids and ion milled down to ≈ 100 nm thickness at 30 keV with final polishing steps performed using a 5 keV beam. The final thickness of the specimens was ≈ 80 nm. Since the actual device sizes are extremely small (65×65 nm^2), it is easy to lose the active device region during the ion beam thinning process necessary to make the electron transparent TEM specimens (≈ 80 nm). Thus, the thin strip of Pt fiducial layer is essential to locate the active device region within the thickness of the TEM specimens during milling as seen in Figure 5.5. Subsequently, 1.5 μm thick of the protective Pt capping layer was deposited on top of the Pt strip with the ion beam. This procedure allowed the entire device structure to be captured within the TEM specimen to detect all the possible switching-induced structural changes in the device.

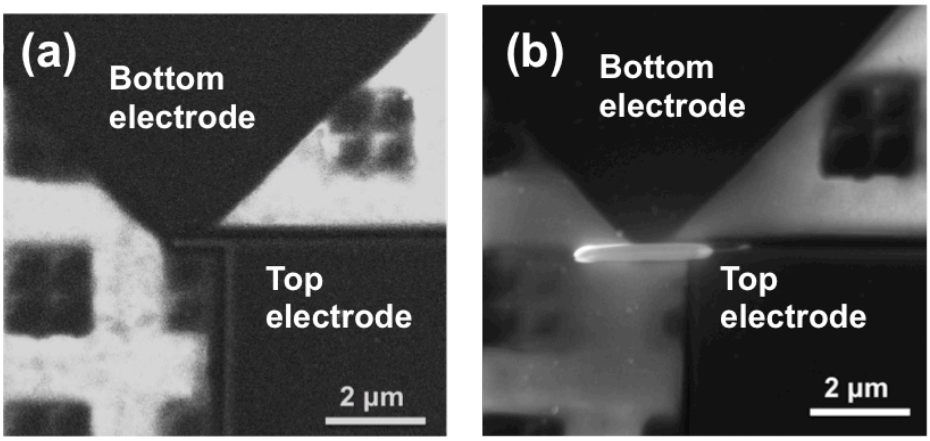

Figure 5.5 SEM micrographs of the crossbar RRAM device. The active device region is defined by overlapping of the top and bottom electrodes. (a) Before and (b) after electron beam-assisted chemical vapor deposition (CVD) Pt deposition along the top electrode serving as a fiducial mark during the specimen thinning process.

High resolution TEM (HRTEM) imaging was conducted using a C_s-corrected FEI Titan G2 80-300 TEM at 300 keV. The specimens were oriented along a zone axis referenced by the Si substrate in order to minimize the overlap between the layers. In order to image all existing crystallites through the thickness of the specimens, multiple images at the same location were collected with different objective lens strength (through focus imaging series).

5.3 Results and discussion

5.3.1 Local temperature extraction

Figure 5.6 shows the DC forming (black) and switching *I-V* characteristics of the TiN/Hf/$HfAlO_x$/TiN stack obtained with the current compliance set to 50 μA, 100 μA and 200 μA (during forming and switching). In all of these cases, the current compliance was assured by means of an on-chip transistor or resistor ballast. This minimized the capacitance of connections between the ballast and the devices, practically eliminated the energy dissipation due to capacitance discharge and allowed for a much better control of current during electro-formation than the off-chip ballast. As seen in Figure 5.6, the resistance of the low and high resistance state of the device decreases by nearly a factor of 4, as the compliance current during forming increases from 50 μA (red) to 200 μA (blue). The pulsed *I-V* characteristics of the device were used (see Experimental section 5.2.2) to extract the temperature excursions in the device.

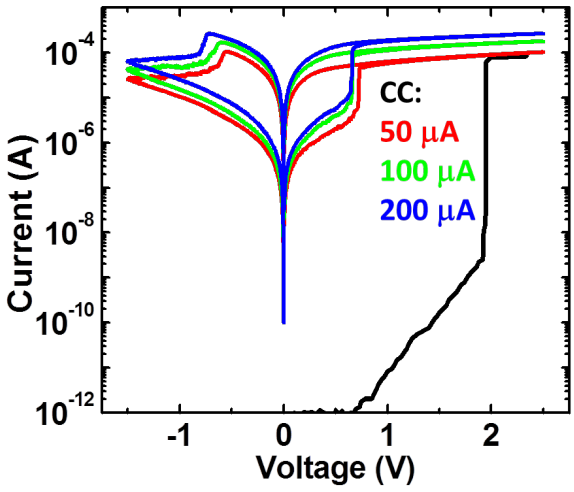

Figure 5.6 Quasi-DC forming and switching *I-V* characteristics of the devices at different compliance current at forming. A linear scale *I-V* can be found in Figure 5.3.[100]

The extracted temperature increase (ΔT) is plotted as a function of the applied power, P, in the low resistance state (LRS) of the device formed with the current compliance of 50 μA, as shown in Figure 5.7.

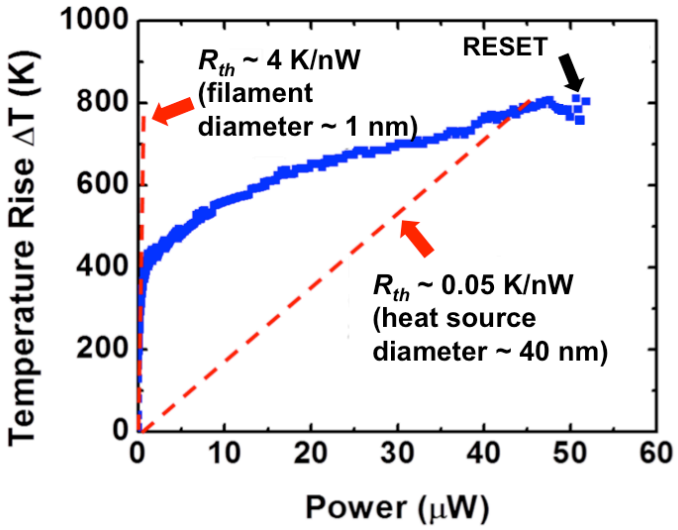

Figure 5.7 Temperature increase versus power in the low resistance state of $Hf_{0.82}Al_{0.18}O_x$-based device.[100]

The slope of the ΔT versus power (P) curve represents the thermal resistance (R_{th}) that is experienced by the heat-source. In the steady-state:

$$\Delta T = R_{th} \times P. \qquad \textbf{Equation 5.1}$$

Here, R_{th} depends on the thermal conductivity of the filament and the surrounding oxide, the distance over which the heat is transported (*i.e.* the thickness of the functional layer) and the area of the heat source. Out of these parameters, the area of the filament is the

only parameter that can change with dissipated power as thermal conductivity has a weak dependence on temperature.[33] At low dissipated power (< 1 μW) the temperature increases linearly with power corresponding to a constant cross-section of the conducting non-volatile filament. At higher power, the slope continuously decreases and at power close to the RESET reaches 0.05 K/nW. This implies that the effective cross section of the area where the heat is generated increased significantly. This change is interpreted in the following way. At low power, the current is conducted solely by the permanent small diameter metallic filament. As the power increases, the temperature of both the filament and the surrounding oxide increases, raising the electrical conductivity of the oxide matrix and decreasing that of the filament. The heat now is generated in a much larger volume with the significantly lower R_{th}. The effect only persists when the bias is on; the next switching cycle starts again with a small permanent metallic filament. In other words, one can consider the nonvolatile filament as the region detected using pulsed *I-V* (without Joule heating). This is the region with local oxygen deficiency. The region around the filament gets hot at high biases and thus becomes conducting. This is purely an electro-thermal byproduct of self-heating of the nonvolatile filament. However, as the electrical thermometry gives the size of the heat source, this region is detected in the measurement leading to a reduction in ΔT vs R_{th} slope.

This model was made quantitative by using finite element simulation to track changes in R_{th} with power. Figure 5.8 shows a COMSOL-generated plot of thermal resistance for filaments of various sizes, using a purely thermal simulation. To generate this plot, the steady-state temperature response of the device was simulated assuming conducting

regions (filaments) of increasing size – from 0.5 nm up to 400 nm radius. This simulation plots the ratio of the temperature rise to the applied power (arbitrary value of 10 μW assumed) to obtain the thermal resistance R_{th}. The thermal resistance is akin to a bulk equivalent of the resistance seen by the region which dissipates power (filament and hot zone), i.e. thermal resistance between the filament and the thermal ground. To improve upon the previous simulation,[11,33] a TBR of 200 MW/m^{2}K have been included as a component of this bulk R_{th}.

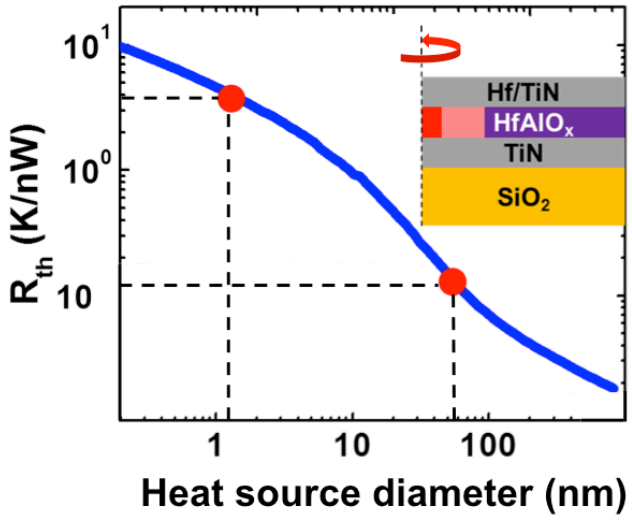

Figure 5.8 Thermal resistance for varying filament size. The inset presents the schematics of the device used in simulation. Red region represents the non-volatile metallic filament and the surrounding pink region represents the hot but otherwise untransformed oxide.[100]

The plot in Figure 5.8 is used as a lookup table to extract the radius of the heat source, in this case the conductive filament, for a measured R_{th}. The diameter corresponding to an R_{th} of 4 K/nW observed at low power is about 1 nm. This corresponds to the size of the permanent conductive filament serving as the heat source. It must be noted that this

thermal resistance (R_{th}) is approximately 100 times greater than that reported in the previous work.[33] This is due to a much smaller size of devices used in this study than the ones in previous work (85×85 nm^2 versus 1×1 μm^2), smaller thickness of the electrodes (5 nm versus 20 nm) and smaller thermal conductivity of the TiN bottom electrode compared to Pt (1.3 W/m·K versus 17 W/m·K). All three result in the electrodes being much less efficient as heat sinks.

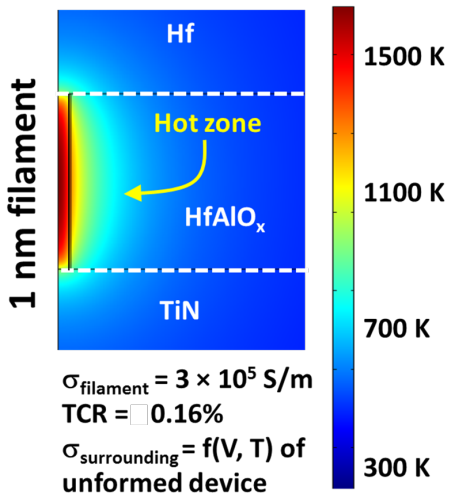

Figure 5.9 Electro-thermal simulation to estimate temperature distribution at 0.8 V and 40 μW dissipated.[100]

With the increase of voltage and the temperature of the filament, the surrounding oxide heats up substantially. This causes the electrical conductivity of the surrounding region to increase,[33] and the current to spread beyond the metallic filament. As the volume where the power is dissipated increases, the corresponding thermal resistance is reduced. This is apparent in Figure 5.8 where at voltages close to RESET, the slope of the ΔT versus power decreased to 0.05 K/nW corresponding to a diameter of the hot zone of about 50

nm. One must note that this diameter is averaged by the conductivity and the temperature is also similarly averaged.

The line scan of the temperature as a function of position obtained from the electro-thermal simulation (Figure 5.9) is shown in Figure 5.10(a). This simulation assumed the filament size obtained from low-power filament diameter (1 nm, Figure 5.8) with its temperature dependent conductivity obtained using pulsed *I-V* characterization (see Figure 5.4). The approximate temperature coefficient of resistance (TCR) is 0.16% in the investigated temperature range; however, for precision, a non-linear fit to the pulsed *I-V* incorporates TCR reduction at high temperatures. For the surrounding material, the electrical conductivity which is a non-linear function of voltage and temperature is used, as obtained from calibrations of an unformed device. The simulation is an axisymmetric simulation that allows electro-thermal conduction in all directions, allowing us to view the current spreading described in Figure 5.7. The peak local temperature obtained in the simulation is ≈ 1600 K in the middle of the nonvolatile filament. The temperature of the surrounding oxide reaches ≈ 850 K 7 nm away from the 1 nm permanent filament (Figure 5.10(a)). The corresponding current density distribution is shown in Figure 5.10b. The *I-V* characteristics of the device generated by this simulation match the experimental results, further corroborating the effect of heat and current spreading.

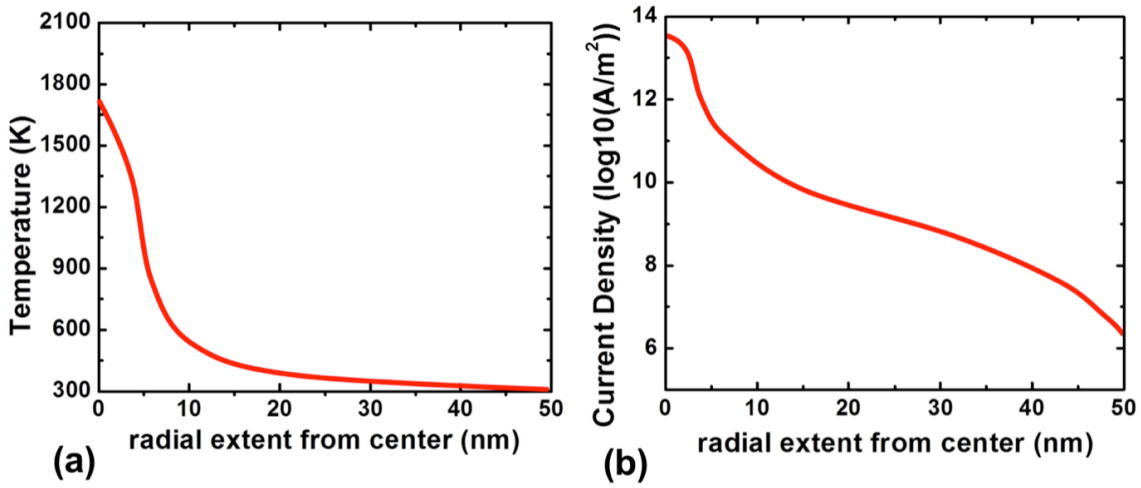

Figure 5.10 COMSOL simulation of a device electroformed with current compliance of 50 μA (Figure 5.6) under bias of 0.8 V. (a) Temperature distribution. (b) Current density as a function of distance from the center of the filament.[100]

5.3.2 Microstructural analysis

In order to experimentally verify the magnitude and extent of temperature excursions during switching, I have analyzed the microstructure of the device stacks by HRTEM. Figure 5.11(a) is a cross-sectional view of the pristine device showing TiN/Hf/HfAlO$_x$/TiN stack, and Figure 5.11(b) and 5.11(c) provide magnified views at the left and right edge of the device, respectively.

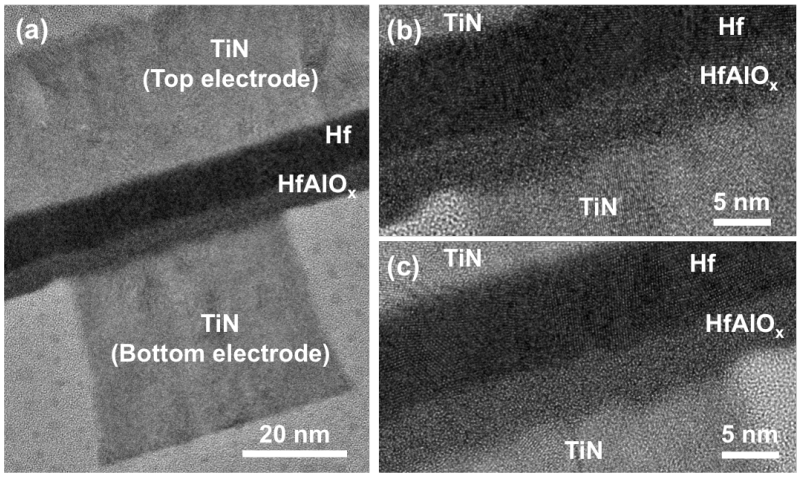

Figure 5.11 Cross-sectional TEM image showing the as-fabricated nominally (85×85) nm^2 device. The TEM sample was cut parallel to the top electrode of the crossbar device. Low magnification (a) and high magnification views of the left (b) and right (c) edge of the device.[100]

The TEM samples were sectioned parallel to the TiN top electrode of the crossbar device. As a consequence, the top electrode extends across the entire length of the sample (TiN layer in the upper half of the Figure 5.11(a)) and the bottom electrode is oriented perpendicular to the cross-sectional TEM sample surface. The two TiN electrodes are polycrystalline and exhibit a microstructural morphology consistent with columnar growth. The $HfAlO_x$ functional layer is slightly lighter than the Hf oxygen getter layer because of the atomic mass/density difference. The light grey contrast surrounding the TiN bottom electrode is the SiO_2. Small recesses in the functional layer seen at the edges of the top electrode are likely due to an etching process during device fabrication. The recesses provide landmarks to confirm that the magnified images in Figures 5.11(b) and 5.11(c) were recorded at the edges of the device. Some small regions of dark contrast that

can be seen in the SiO_2 layer are due to re-deposition of sputtered materials from the FIB specimen preparation process. Note that these features are not seen in the device area and so do not affect phase contrast imaging of the device layers. The $HfAlO_x$ functional layer in the as-fabricated device is amorphous. No signs of crystallinity were observed in $HfAlO_x$ even when performing a through focusing series and FFT analysis. This conclusion has been further confirmed by examining a much larger volume of $HfAlO_x$ in the as-deposited state for a different, larger device (1×1 μm^2) as seen in Figure 5.12.

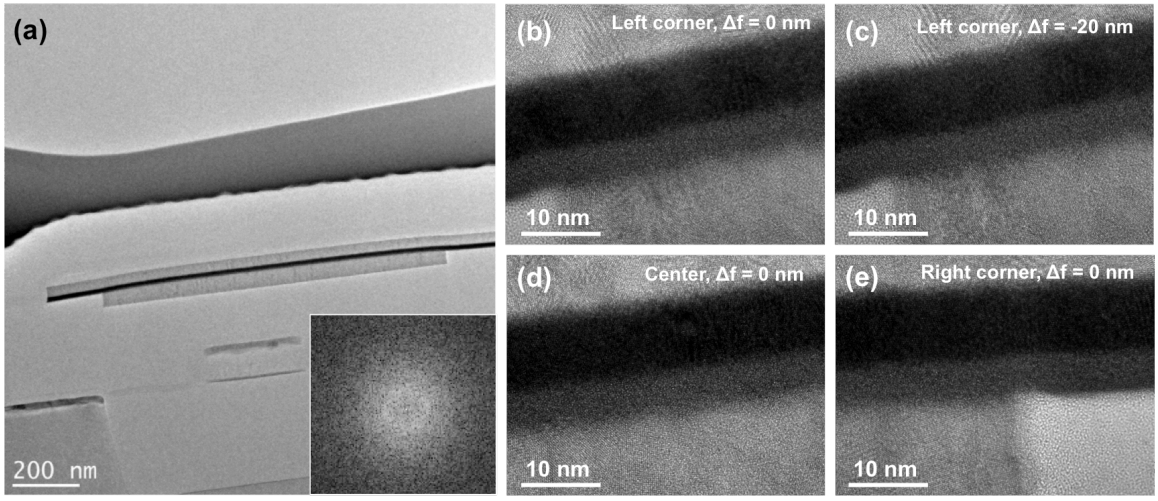

Figure 5.12 (a) Cross-sectional HRTEM micrographs of (1×1) μm^2 crossbar $HfAlO_x$ device. (b-e) A focusing series showing the $HfAlO_x$ layer is amorphous. The inset in (a) is a Fast-Fourier Transform (FFT) of $HfAlO_x$ layer. No spot pattern was observed in the FFT.

Similar analysis has been conducted on devices that were electroformed with current compliance set at 10 μA (Figure 5.13(a)), 50 μA (5.13(b)), and 200 μA (5.13(c)). The small device sizes (the actual size of the active area was 65×65 nm^2) allowed for inspection of the entire active device volume after biasing and, as the consequence, for

detecting any microstructural changes. The micrographs are high magnification images of the right edge of the devices (the recess is seen at the lower right corner).

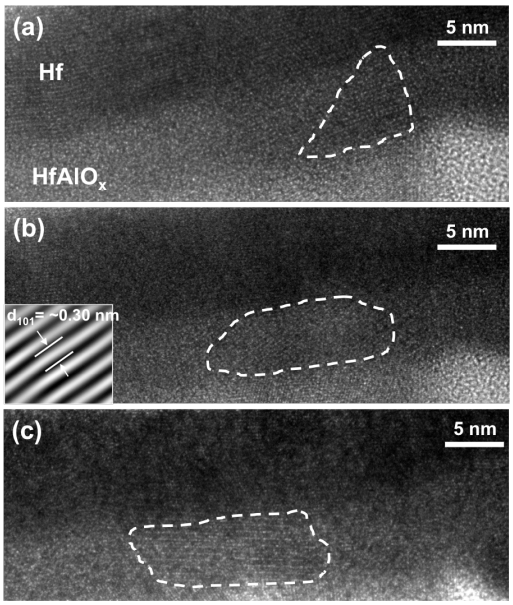

Figure 5.13 HRTEM micrographs showing a localized crystallite embedded in an amorphous matrix electroformed with (a) 10 μA, (b) 50 μA, and (c) 200 μA current compliance. The inset in (b) is an inverse FFT of the crystallite region showing clear lattice fringes.[100]

Imaging through-focus series revealed one crystalline region embedded in the amorphous $HfAlO_x$ layer for each device examined. The phase contrast regions, or lattice fringes, visible in these crystallites are denoted by dashed lines in Figure 5.13. An interplanar spacing of ≈ 0.3 nm was measured for the lattice fringes using Fast Fourier Transform (FFT) analysis and likely corresponds to the {101} crystallographic planes for tetragonal $HfAlO_x$. Details of FFT analysis can be found in Supporting information S5.2. The crystallite size is ≈ 10 nm at 10 μA compliance current and ≈ 15 nm at both the 50 μA and 200 μA compliance current. I interpret the presence of crystalline regions as an

indication of bias-induced crystallization of the $HfAlO_x$ caused by local heating of the oxide around the conducting filament. One has to note that the crystalline $HfAlO_x$ is not necessarily conducting and the crystallites are not the filament itself. These are merely interpreted as microstructural features indicative of appreciable, local Joule heating. As discussed above, the estimated size of the metallic filament (≈ 1 nm diameter) is significantly smaller than the crystallite size. The filament is believed to have the same crystalline structure as the crystallites with the only difference being the oxygen deficiency. While nominal resolution of the instrument used to acquire these images is < 0.1 nm, it is difficult to observe the filament due to the presence of the surrounding material along the electron beam path in cross-sectional view configuration. I have attempted to image the filament by using scanning TEM (STEM) electron energy-loss spectroscopy (EELS) with results described in the 5.3.3 Chemical Analysis section.

This above assertion is supported by the results of an annealing experiment. The devices used in this experiment were from the same wafer as the 65×65 nm^2 device described above. Separate dies cut from the wafer were annealed at different temperatures for 2 seconds in a rapid thermal annealing furnace and the FIB-TEM samples were prepared from large 3×3 μm^2 crossbar devices. The annealing time was chosen to set the similar time period of the DC sweep test. Five different locations in each specimen were randomly selected and through focus imaging was used to assess degree of crystallinity. Figure 5.14 shows cross-sectional views (one of the through focus series) of the devices annealed at 820 K, 870 K, 920 K, and 970 K.

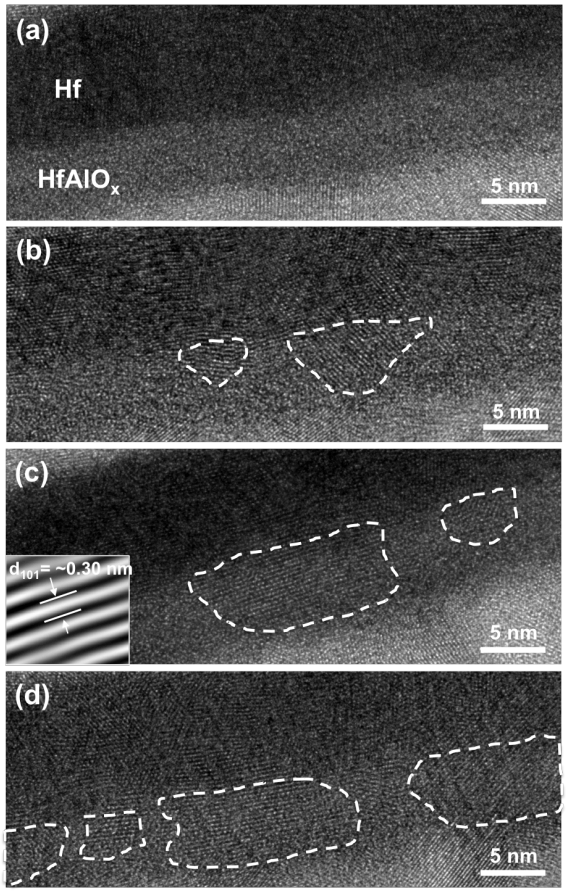

Figure 5.14 HRTEM micrographs of specimen annealed for 2 seconds at: (a) 820 K, (b) 870 K, (c) 920 K, and (d) 970 K. The inset in (c) is an inverse FFT of the crystallite region showing clear lattice fringes.[100]

The top dark layer in all Figure 5.14 images corresponds to Hf and is followed by slightly brighter $HfAlO_x$ and TiN layers. No signs of crystallization were found in specimens annealed up to 820 K. Above this temperature, all annealed samples contained crystallites with size and density increasing with temperature. The crystallites are outlined by white dashed lines in Figure 5.14 and the observed d-spacing was again ≈ 0.3 nm in all cases. It appears that the crystallites in $HfAlO_x$ nucleate on the Hf grains with the same orientation of lattice fringes (shown in Figure 5.15).

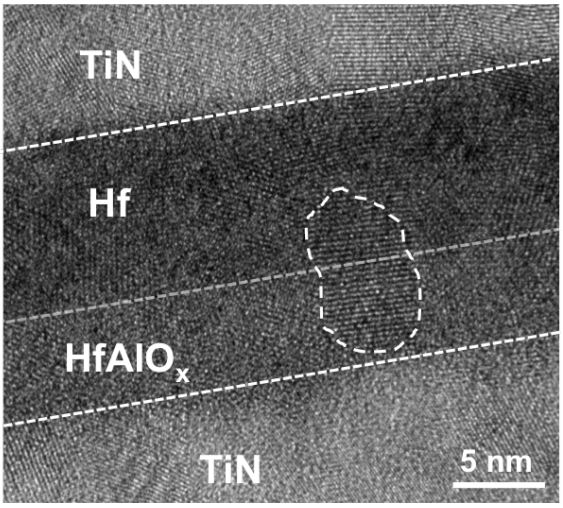

Figure 5.15 A HRTEM micrograph showing a templated growth of $HfAlO_x$ crystallite from Hf while rapid thermal annealing at 870 K.

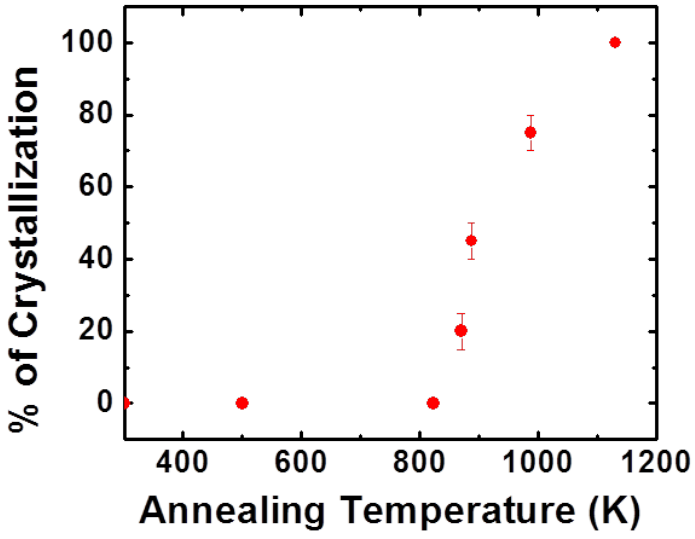

Figure 5.16 Degree of crystallization as a function of annealing temperature. A clear transition is observed around 850 K.[100]

The degree of crystallization (volume percent) as a function of annealing temperature is estimated and plotted in Figure 5.16. Since the first crystallites appeared in the annealed samples at 870 K, I set 850 K as the approximate crystallization temperature of $HfAlO_x$. One can determine the activation energy for the crystallization with more thorough annealing experiments (e.g. degree of crystallizations as a function of temperature for different heating rates) by applying Kissinger peak method and draw more quantitative result.[116] Above annealing study indicates that the crystallite size (≈ 15 nm) observed in the TEM analysis is consistent with the extent of the hot zone (≈ 14 nm) extracted from the thermometry and simulated by the COMSOL model (diameter corresponding to the size of the volume where temperature exceeds 850 K as seen in Figure 5.10(a)). *I-V* measurements for annealed devices show no changes in device resistivity, thus confirming that the crystallization does not correspond to filament formation itself, but rather is due solely to localized heating.

5.3.3 Chemical analysis

In order to identify filament configuration and understand its chemical nature, STEM-EELS analysis has been conducted using a C_s-corrected FEI Titan 80-300. The 50 μA CC specimen (Figure 5.13(b)) chosen for the chemical analysis was re-polished using 5 keV ion beam to further reduce the thickness of the specimen. The thickness was determined to be ≈ 40 nm by the Log-Ratio Method.[117] The STEM-EELS analysis did not detect any local oxygen deficiency both within and beyond the crystallite region. Instead, stochastic oxygen signal fluctuation was observed along the $HfAlO_x$ functional layer indicating that

oxygen content variation was below the sensitivity limit of the current STEM-EELS experiment, corresponding to < 4 % of oxygen content.

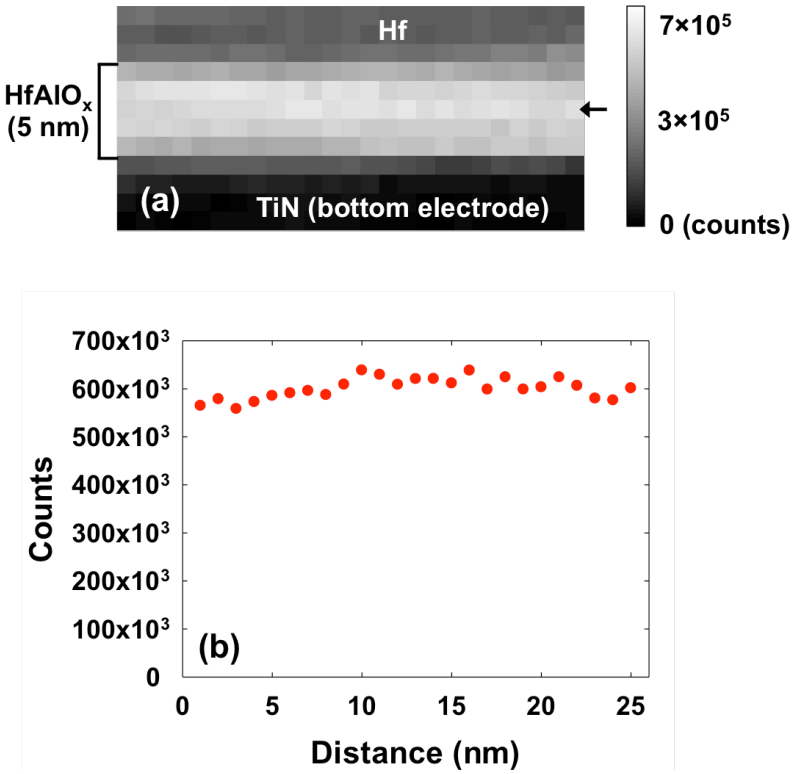

Figure 5.17 STEM-EELS O-K edge signal collected away from the crystallite in 50 µA CC specimen. (a) Integrated O-K edge map of Hf/HfAlO$_x$/TiN stack. Each pixel corresponds to (1×1) nm^2. (b) Integrated O-K edge line scan along 6th row (marked by an arrow in (a)).[100]

To assess the detection limit of the EELS experiment, an O-K edge map was collected from the same specimen in an area far from the crystallite (Figure 5.17(a)) with a spatial resolution of 1 nm/pixel and 2 second/pixel acquisition time. The acquisition time (electron irradiation dose) was limited to minimize electron beam-induced damage to the functional layer. The marked region from 4th to 8th row of the image is the HfAlO$_x$

functional layer (5 nm thickness) and the slight contrast change at the interfaces is due to the overlap of the Hf/$HfAlO_x$ and $HfAlO_x$/TiN layers. Figure 5.17(b) is an O-K edge line scan along the 6th row in the area map (marked by an arrow in Figure 5.17(a)). The line profile oscillates around the average with a standard deviation of 3.9 %. Since there is no reason to suspect the oxygen content to vary in the $HfAlO_x$ at these length scales, this value represents the oxygen detection limit in the investigated structures. Even in case of pure Hf filament embedded in the 40 nm thick $HfAlO_x$ matrix in current experiment, the oxygen deficiency along the electron beam path would amount to about 2 %, which is below the detection limit. It should be noted that the reported values of the oxygen deficiency in the filament were much lower than 100% (< 13 at.%).[20,21,96] Increasing acquisition time, reducing specimen thickness, and changing chemical make up of the functional layer may help to increase the detection limit but all of these approaches are expected to be limited. At present, EELS is unlikely to produce an oxygen deficiency estimate in this material system, principally because in the cross-sectional sample configuration, the beam traverses the entire oxide thickness which is many times the estimated diameter of the filament.

5.4 Conclusion

The estimates of the maximum temperatures reached during the switching cycles were presented in 85×85 nm^2 $HfAlO_x$ RRAM devices using transient thermometry. For these devices, the temperature of the metallic non-volatile filament, could reach as high as 1600 K at the onset of RESET. The thermometry estimates the filament size to be as small as 1 nm in diameter. At high biases the surrounding oxide heats up and there is a

larger conductive region that lowers the current density. The temperature can reach 850 K 7 nm from the filament at RESET voltage. The thermometry and modeling were verified by HRTEM of the as-fabricated and electroformed devices. The images show a single crystallite in each of the formed devices with the size in the 10-20 nm diameter range. Independent TEM experiments determined the onset of $HfAlO_x$ crystallization at 850 K. The size of the crystallites agrees with the simulated temperature distribution at RESET bias. In a parallel STEM-EELS experiment, no chemical change has been observed due to the inherent detection limit of cross-sectional STEM-EELS. The thermometry of these devices, showed the comparable change of thermal resistance. This methodology and observations could play a pivotal role in understanding the role of the surrounding oxide region in thermal dynamics, peak temperature, switching mechanism and scaling behavior.

Supporting information

S5.1 Time domain transmissometry setup

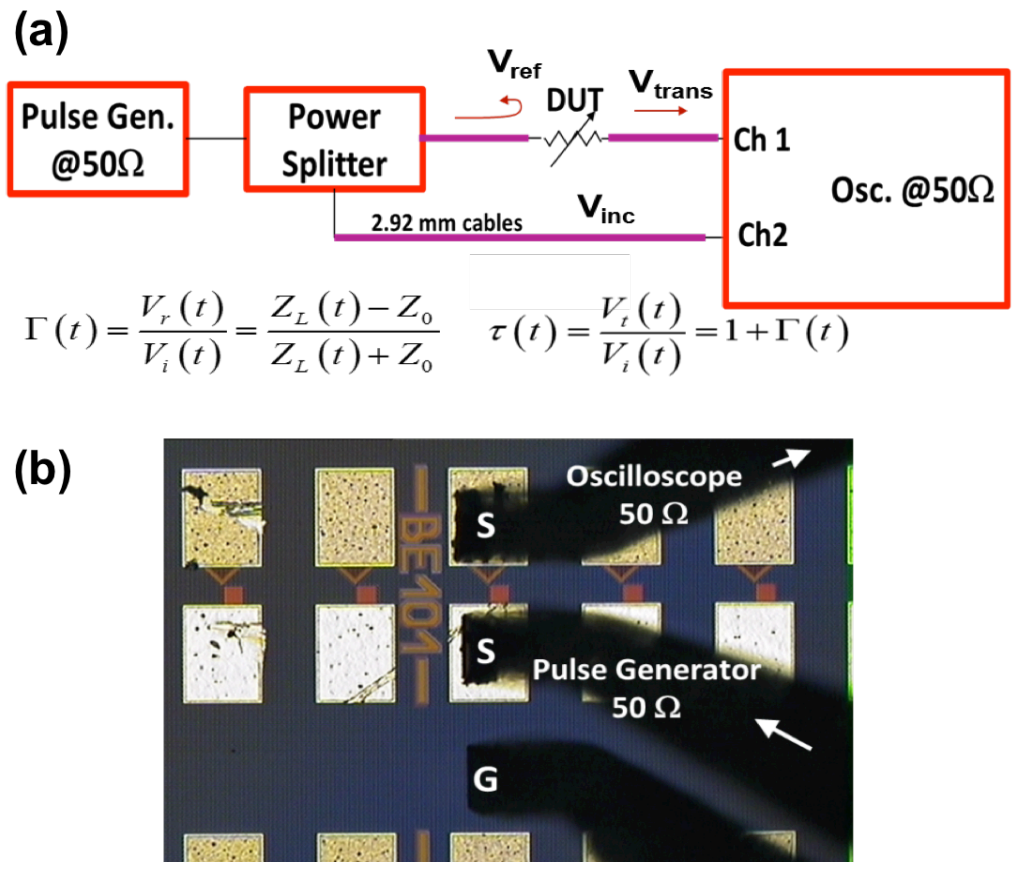

Figure S5.1 (a) Circuit schematic of the time domain transmissometry setup with equations to monitor the device characteristics at sub-100 ps speeds. (b) Optical micrograph showing SSG (signal-signal-ground) probes used for through measurements to improve signal to noise ratio.

S5.2 Fast Fourier transformation (FFT) analysis

In order to confirm the pristine $HfAlO_x$ layer is amorphous, FFT analysis has been performed via ImageJ software. As seen in Figure S5.1a and S5.1b, multiple locations in the pristine $HfAlO_x$ layer were analyzed and none of the FFTs show spot features that would indicate crystallinity. More focusing series were analyzed and I concluded the initial microstructure of the $HfAlO_x$ layer was amorphous. On the other hand, clear spot patterns are seen from the FFT analysis of the switched $HfAlO_x$ layer as shown in Figure S5.1c and S5.1d, corresponding to tetragonal d_{101} ~0.30 nm. The various d-spacings of $HfAlO_x$ phases obtained by SingleCrystal software are listed in Table S5.1.

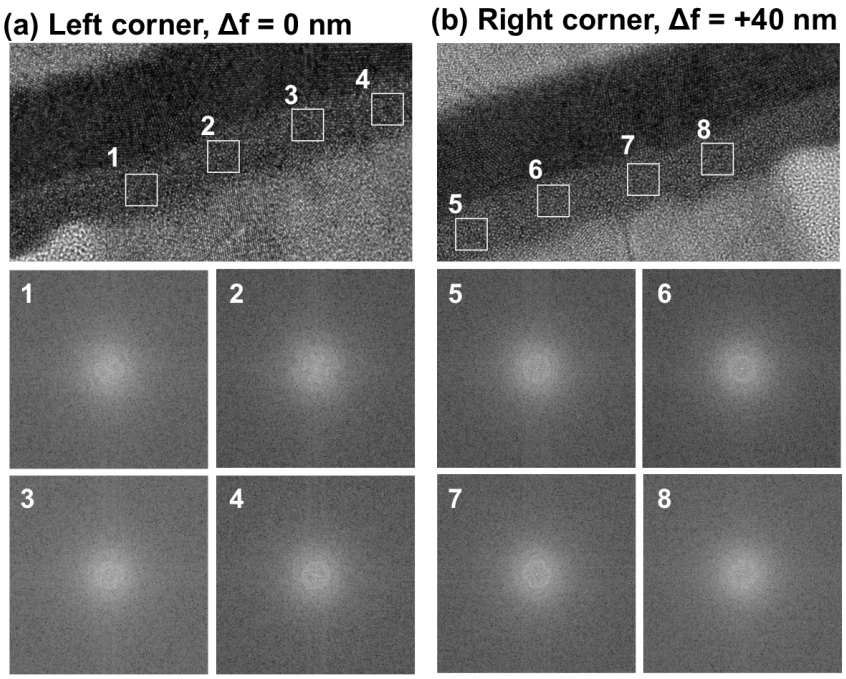

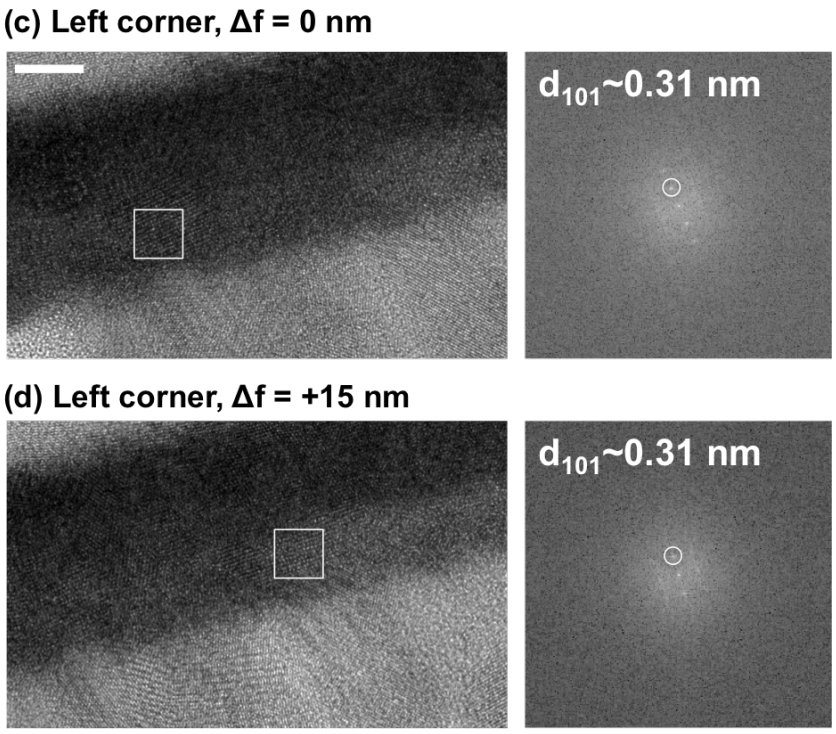

Figure S5.2 (a, b) FFT analysis of the multiple locations in the pristine $HfAlO_x$ layer. (c, d) FFT analysis of switched $HfAlO_x$ layer. The FFT shows clear spot patterns corresponding d_{101} (marked as a white circle). The scale bar is 5 nm.

Table S5.1 Various d-spacings of tetragonal and monoclinic $HfAlO_x$ phases calculated using SingleCrystal software.

	Tetragonal	Monoclinic
d-spacings	d_{002} ~ 0.33 nm	d_{002} ~ 0.33 nm
	d_{101} ~ 0.30 nm	d_{020} ~ 0.26 nm
	d_{110} ~ 0.25 nm	d_{200} ~ 0.24 nm
	d_{112} = 0.19 nm	d_{022} ~ 0.18 nm

6 On-going research projects with preliminary results

6.1 Plan-view EELS on TaO_x-based RRAM devices

Following up on the EELS experiment in Chapter 5, I further developed the EELS approach to investigate the chemical makeup of the conductive filaments. As described in Chapter 5, presence of the unchanged oxide layer around the conductive filament significantly lowers the signal detection sensitivity. Even though the potential filament location can be identified by observing the local crystallization (see Figure 5.13), it was difficult to sense the subtle oxygen deficiency around the filament in the cross-sectional view orientation. In order to overcome this limitation, I designed and fabricated the TaO_x-based RRAM devices allowing fabrication of the plan-view oriented TEM specimens as seen in Figure 6.1. I have intended to use TaO_x binary oxide as a functional oxide layer instead of $HfAlO_x$ studied in previous chapter to simplify and facilitate the chemical footprint analysis.

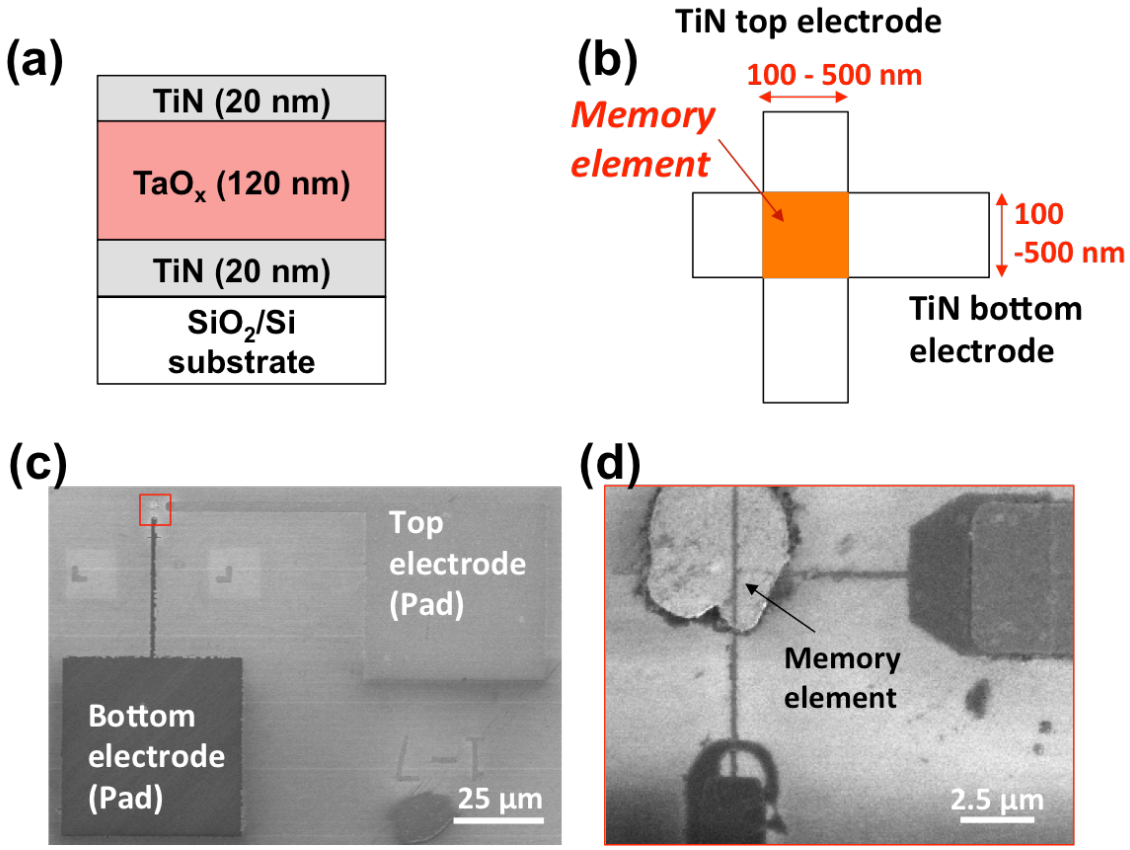

Figure 6.1 Fabricated TaO_x-based crossbar RRAM device for the plan-view EELS experiment. (a) Schematic of the cross-sectional and (b) plan (top) -view of the device. (c) Low and (d) high magnification of SEM micrographs of the device. (d) is the enlarged view of the red box in (c), showing memory element (overlapping of the top and bottom electrodes). The rounded square contrast in (d) is the patterned TaO_x functional layer sandwiched by the two electrodes.

The crossbar structures with a stack of TiN (20 nm) / TaO_x (120 nm) / TiN (20 nm) were fabricated on Si/SiO_2 substrate. The two TiN top and bottom electrodes were patterned and sputter deposited, and the TaO_x functional layer was reactive sputter deposited with 3 SCCM of oxygen gas flow. The memory element (active device region) is at the

overlapped area of the top and bottom TiN electrodes. The electrode sizes are ranging from 100 to 500 nm with an increment of 100 nm and thus 5 different device sizes were fabricated (100^2, 200^2, 300^2, 400^2, and 500^2 nm^2). Note that the smaller device size is desirable for the current experiment to ease identification of the potential filament location. A 10 kΩ on-chip load resistor was patterned to minimize parasitic capacitance discharge during electrical testing of the devices.

Figure 6.2 shows DC *I-V* forming and switching curves of the 300×300 nm^2 device. The forming voltage was 10.5 V, and SET and RESET voltage was 3.8 V and -3 V, respectively.

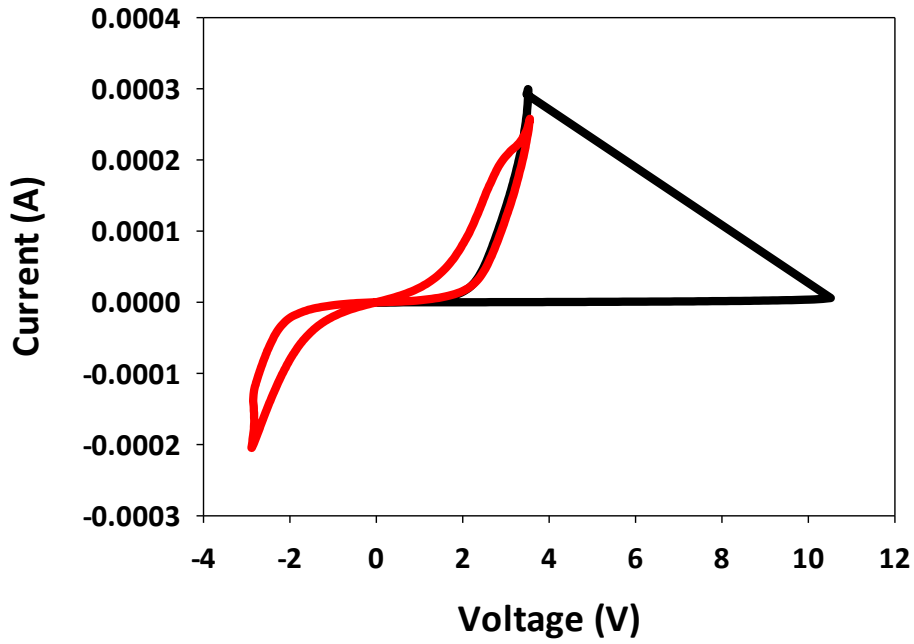

Figure 6.2 DC *I-V* curves showing forming (black) and switching curves (red) of the 300×300 nm^2 TaO_x-device.

Figure 6.3 is a bright-field TEM micrograph showing the cross-sectional view of the device (500×500 nm^2). The specimen was cut along the top electrode via FIB milling (FEI Nova 600 Nanolab) and finalized with low energy ion beam polishing at 5 keV. The thickness of the specimen is measured to be 60 nm. The as-deposited TaO_x film is amorphous and the TiN film is polycrystalline. The speckle contrast in SiO_2 is believed to be re-deposited Pt.

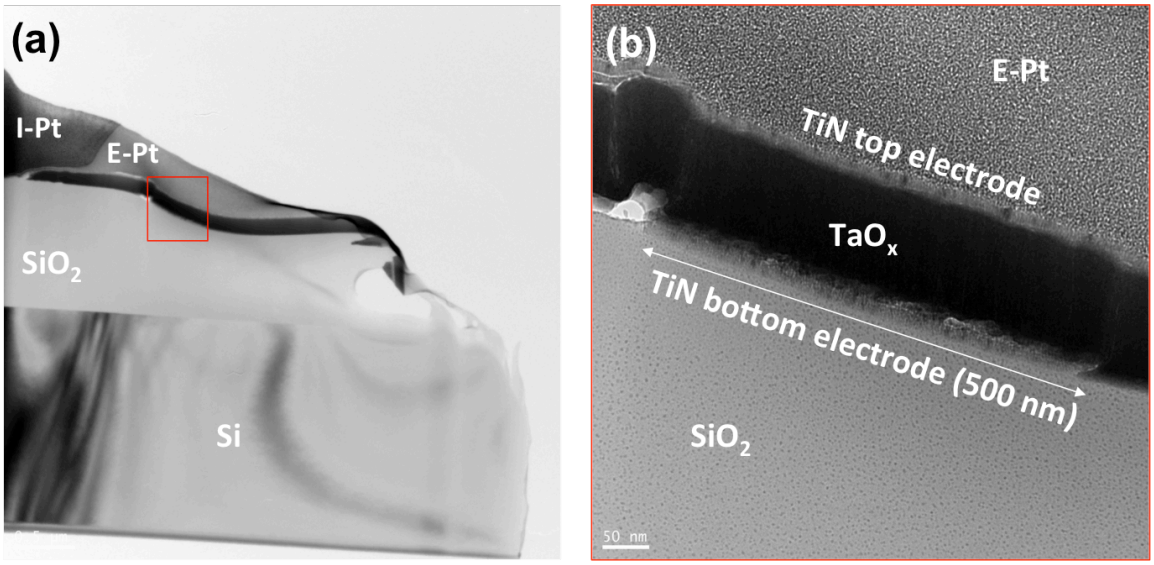

Figure 6.3 (a) Low and (b) high magnification BF TEM micrographs of TaO_x-based RRAM device (500× 500 nm^2). (b) shows enlarged view of the red box in (a).

In order to facilitate the plan-view TEM specimen fabrication, the die can be mounted onto the FIB sample stage as seen in Figure 6.4(b) (i.e. substrate normal is perpendicular to the electron beam column).

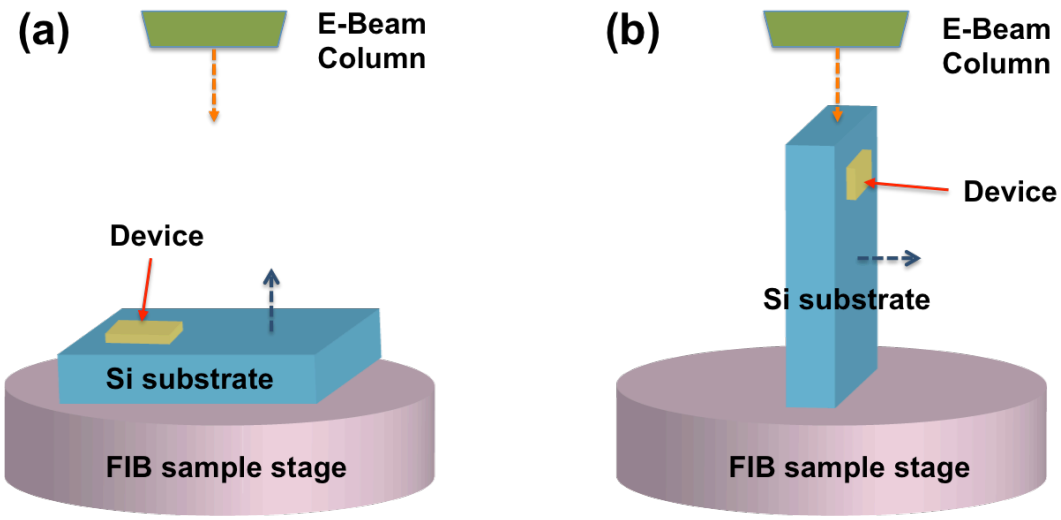

Figure 6.4 Schematic diagrams showing different mounted samples on a FIB sample stage. Si substrate normal is (a) parallel and (b) perpendicular to the electron beam column. Orange and blue dotted arrows indicate the orientation of the electron beam column and Si substrate normal, respectively.

Loading the die (substrate) in that way could enable us to fabricate the plan-view oriented TEM specimens by the conventional FIB lift-out techniques. One big concern for this approach is that it is essential for the devices to be placed very close to an edge of the die. If the devices are located >100 μm away from an edge, then when the die is mounted in the way shown in Figure 6.4(b), > 100 μm deep FIB milling is required to have the memory element captured in the specimen. Thus, placing the devices near an edge is critical for the current experiment. I plan to use a deep reactive ion etching (DRIE) to make a precision cut and locate the device structure within 10 μm away from an edge of the die.

Then, the TEM lamellas (~70×25×15 μm^3) can be lifted out and attached to Omniprobe Cu grids. Using a "window-cut", the specimens are thinned from the Si substrate side toward the TaO_x film and the top and bottom electrodes are removed by using a FEI Helios 600 Plasma FIB (PFIB). The specimens end up having a small-thinned region (window cut) with a freestanding TaO_x film. Figure 6.5 is SEM micrographs showing a model TEM lamella made by FEI Nova Ga^+ FIB. As described above, the free standing TaO_x film can be seen in a small-thinned region.

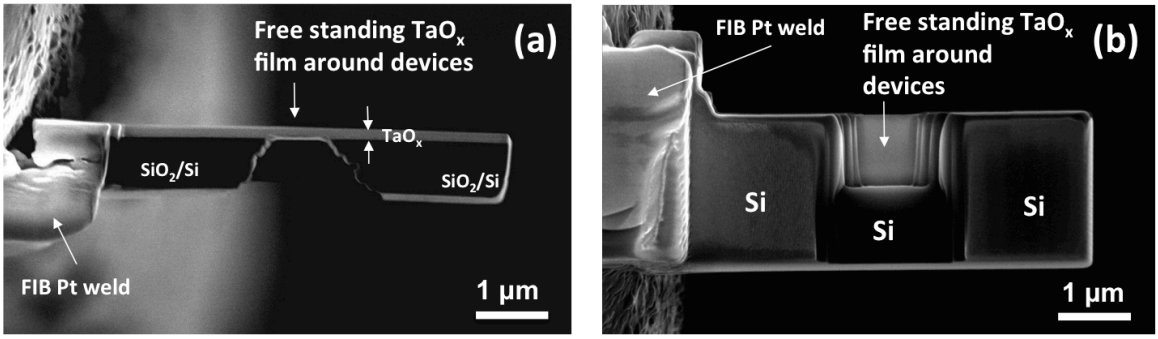

Figure 6.5 (a) Edge-on view and (b) plan-view of SEM micrographs showing model plan-view TEM specimen.

In order to re-evaluate the O-K edge signal detection sensitivity for the TaO_x film, the cross-sectional TEM specimen (Figure 6.3) has been shipped to NIST. A C_s-corrected FEI Titan will be used to map EELS O-K signal for as-fabricated TaO_x film. Once the device fabrication is completed, the plan-view oriented TEM specimens can be prepared via methods described above and EELS O-K edge mapping ends up being performed at NIST to identify the chemical makeup of the filament.

6.2 Electrostatic potential mapping by *in situ* biasing electron holography

The switching mechanisms and nature of conductive filament have been investigated throughout Chapter 3, 4, and 5. However, filaments present a tremendous challenge when using conventional TEM imaging and spectroscopic methods to observe subtle atomic structural changes and compositional variations. As an alternative approach, I proposed direct imaging of electrostatic potential and charge distribution during electrical biasing *in situ* to identify the filament shape and position within the functional oxide layer by adopting an *in situ* biasing electron holography. TEM-based electron holography enables direct visualization and mapping of electrostatic potential and/or the charge distribution in an operating RRAM device with 0.1 eV potential sensitivity.[118]

Electron holography is a TEM phase contrast imaging technique that obtains information about spatial distribution of phase shift of the incident electron beam after penetrating through a specimen.[119] The off-axis electron holography experiments produce interference holographic patterns due to interference between half of the incident electron beam travelling through the specimen with the other half travelling through vacuum (Figure 6.6). The interferogram formed by the phase differences of the two electron beams can be directly related to the electrostatic potential within the specimen since the phase shift is directly proportional to the local electrostatic potential.[72,120]

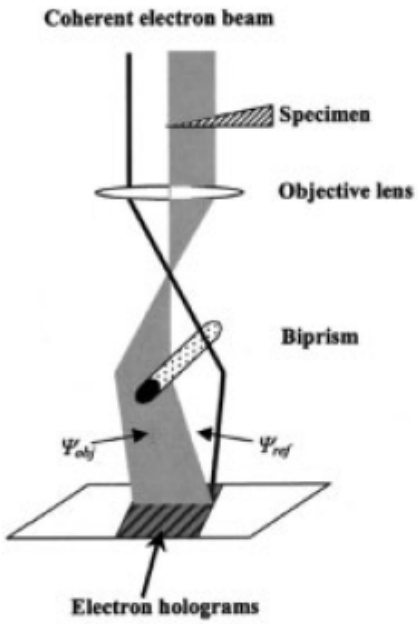

Figure 6.6 A schematic of the electron beam path for off-axis electron holography in a TEM.[119]

Figure 6.7 shows calculated electrical potential distribution in HfO_x-based RRAM devices by Larentis *et al*.[21] under an assumption of the filamentary switching mechanisms with a ~14 nm diameter cylindrical filament described as oxygen vacancy doped area (marked by dashed lines). A voltage-driven ion migration-based switching model was used for the calculation and it predicts the SET and RESET transitions during resistive switching. Figure 6.7(a) and (b) represents the electrostatic potential in the samples under bias in ON state (low resistance) and OFF state (high resistance), respectively. The color maps in Figure 6.7 show potential distribution in functional HfO_x layer sandwiched by metal electrodes at the top and bottom of the map (not shown here). In ON state (Figure 6.7(a)) where the filament connects the electrodes, the potential distribution across the device is uniform. On the other hand, in OFF state (Figure 6.7(b))

where the gap forms near the top portion of the filament, most of potential drop occurs at the gap. Three-dimensional drawings of conducting filament at ON and OFF states are shown in Figure 5.1. I hypothesize that the electrostatic potential distribution during resistive switching (ON and OFF state) obtained by *in situ* biasing electron holography will be similar to the Figure 6.7: uniform distribution at ON state due to the continuous metallic filament and asymmetrical non-uniform distribution at OFF state due to presence of gap along the filament.

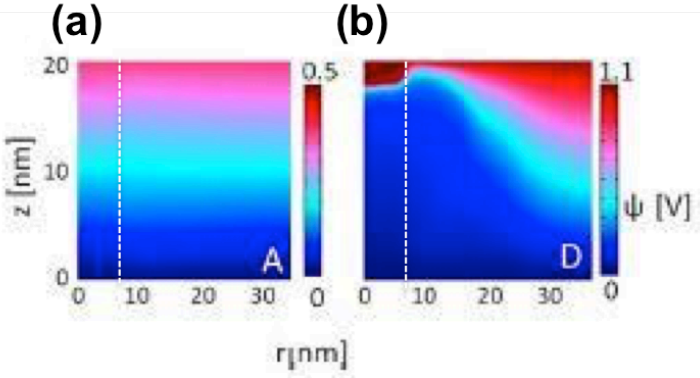

Figure 6.7 Calculated electrostatic potential distribution at (a) ON state and (b) OFF state. The dashed line indicates the half of the cylindrical filament. Reproduced from the reference [20].

This work has been pursued in collaboration with Prof. Fernando Ponce and his group at Arizona State University (ASU). All the specimen preparation and electrical testing have been conducted at CMU. The Protochips Aduro 300 system has been utilized for the experiments, which consists of a control console with power supply, double-tilt TEM holder with biasing capability, and electrical E-chips (specimen supports with pre-

patterned stationary electrical leads). *In situ* electron holography and a numerical calculation for the data conversion have been performed at ASU.

For the current study, cross-square type $HfAlO_x$-based RRAM devices were selected as shown in Figure 6.8. Active device region (85×85 nm^2) is defined where the top electrode (TE) and bottom electrode (BE) overlap. The TE and BE extending along the lift-out specimen (orientation is marked by a dashed box in Figure 6.8(b)) connects to electrical pads for *in situ* biasing with the Protochips Aduro 300 system.

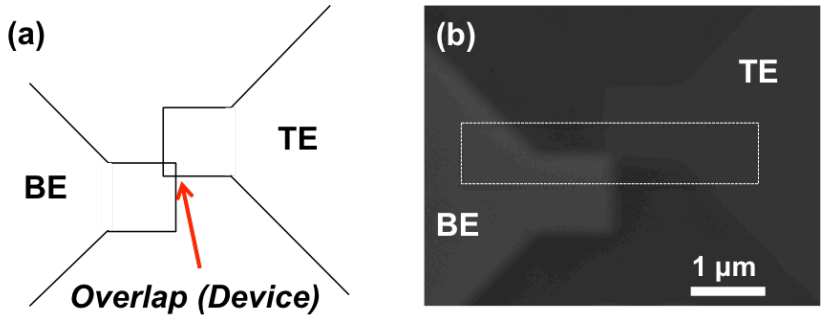

Figure 6.8 (a) A schematic showing a cross-square type $HfAlO_x$-based RRAM device. The active device area (85×85 nm^2) is defined by overlap of the top electrode (TE) and bottom electrode (BE). (b) SEM images of the actual device. The orientation of lift-out specimens is marked by a dashed box.

In order to test the phase and the spatial resolution of electron holography on the specimen, I have prepared a TEM specimen mounted on a conventional Omniprobe TEM grid by using FEI Nova FIB as seen in Figure 6.9. This specimen was also used to verify if the FIB-based sample preparation is suitable for the electron holography experiments at

ASU (i.e. thickness and orientation of the specimen, reference wave location, bi-prism orientation to the TEM specimen). Note that the FIB-based specimen preparation methods have been widely used for electron holography of semiconducting materials.[121–123] As mentioned above, the active device area is defined by the location where the bottom and top electrodes overlap and $HfAlO_x$ is the functional oxide layer where the electrostatic potential variation might be expected under an applied electrical bias. Note that the TiN top and bottom electrodes seen in Figure 6.9 are to be connected to the external voltage source for the actual *in situ* biasing experiments.

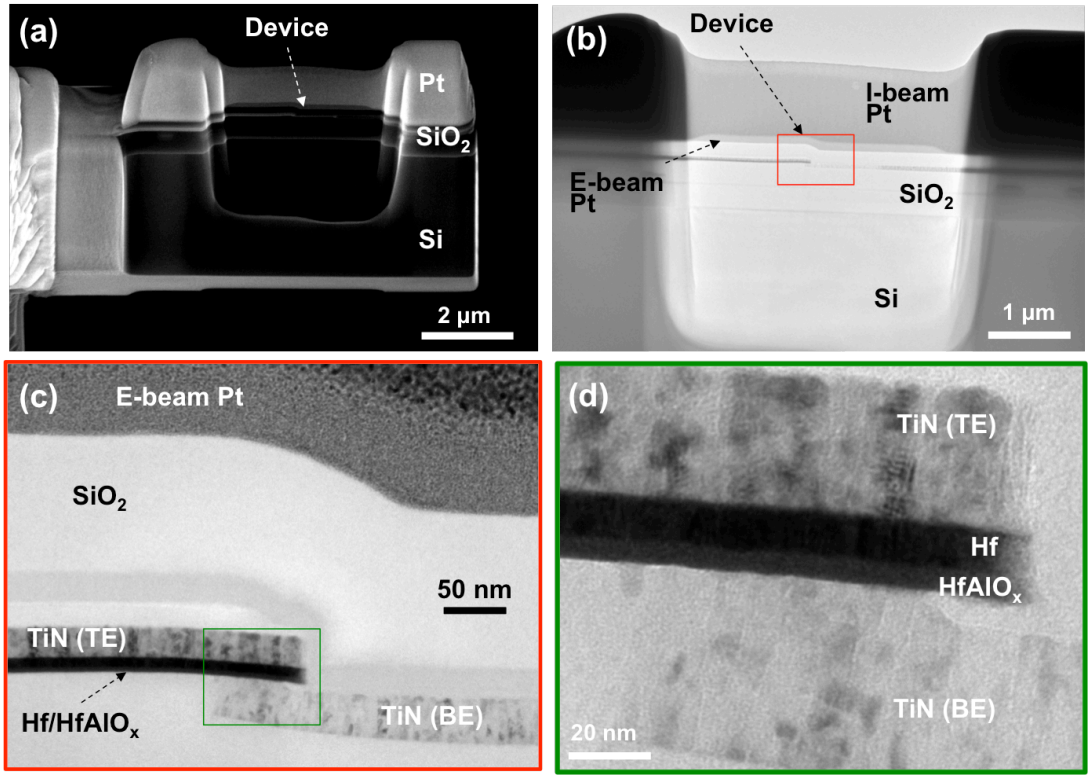

Figure 6.9 Micrographs of FIB-TEM specimen containing $HfAlO_x$-based RRAM. (a) SEM and (b) TEM image of the cross-sectional specimen. (c) Magnified view of red rectangle in (b). (d) Magnified view of green rectangle in (c). Note that the active device region is defined by the two TiN electrodes and the functional layer is $HfAlO_x$ film.

Figure 6.10 is the extracted phase map and electrostatic potential profile from an electron hologram. In order to obtain the electron hologram in this study, the SiO_2 layer was used as a reference wave (instead of vacuum reference wave) and the bi-prism position is then determined as seen in Figure 6.10(a). Since the RRAM device was surrounded by the SiO_2 passivation and there is FIB deposited Pt capping layer, the vacuum reference wave could not be obtained for the current specimen at the desired magnification. The electron hologram was successfully obtained with the SiO_2 reference wave as seen in Figure 6.10(a). The red dotted line indicates the bi-prism position with respect to the device. Figure 6.10(b) is the extracted phase map from the electron hologram in Figure 6.10(a) using a phase extraction algorithm built at ASU. [124] Since the SiO_2 layer was where the reference wave went through, SiO_2 has "0" phase change and the maximum phase change is "15" at the Hf layer. The color bar in Figure 6.10(b) has 256 levels, so that the maximum energy resolution is about 0.06 eV when the phase differences are converted to electrostatic potential. Figure 6.10(c) is the 1-D electrostatic potential profile along the white arrow in Figure 6.10(b). Clear potential differences are observed in different layers. The difference in phase changes between the top and bottom TiN electrodes is because of the TiN thickness different along the electron beam path. Since the device is pristine, the potential difference in the $HfAlO_x$ layer is expected to be uniform. However, ~1 V potential variation along the $HfAlO_x$ layer is observed, which determines the true phase detection resolution for current experiment. In other words, at least 1 V of external bias has to be applied to the device to identify the electrostatic potential drops across the filament for the actual *in situ* biasing electron holography experiment. From these preliminary results, I confirm that the specimen configuration is compatible with the

current electron holography setup, while also determining the required electrical biasing conditions.

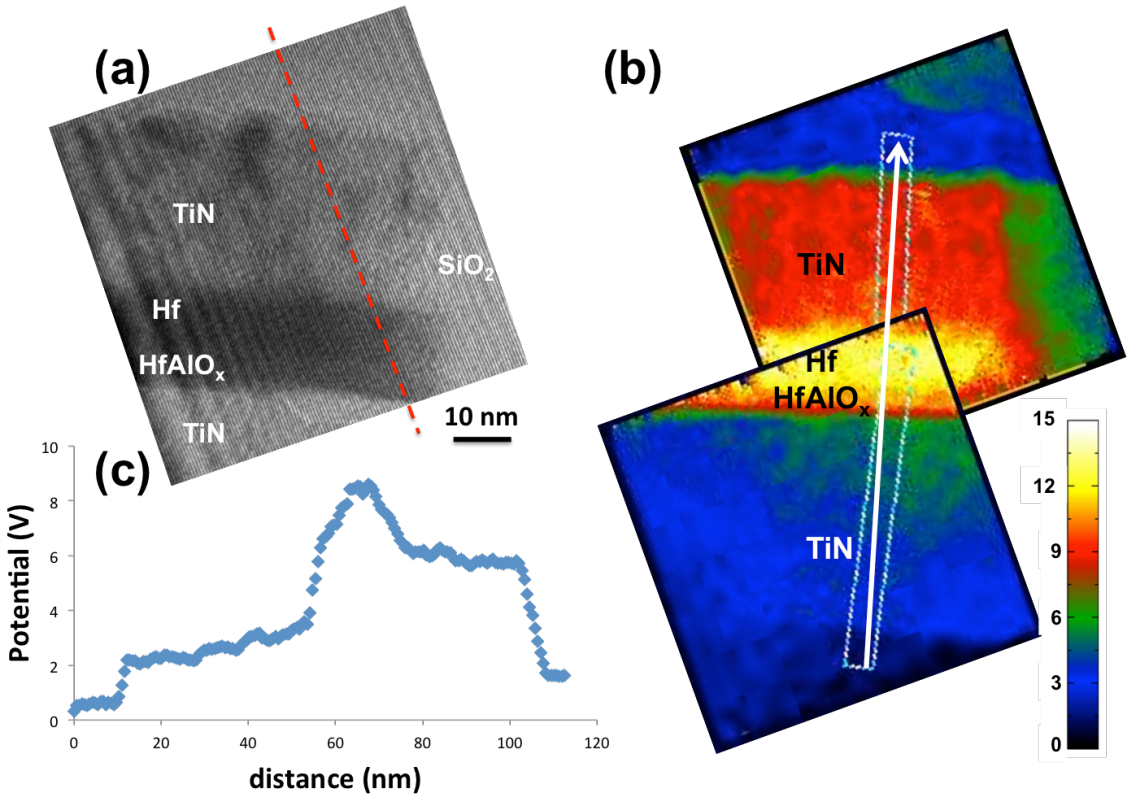

Figure 6.10 (a) A static electron hologram obtained from the specimen in Figure 6.9. The red dotted line indicates the bi-prism position with respect to the device, bisecting the device region (object wave) and SiO_2 passivation layer (reference wave). (b) An extracted phase map from (a) showing phase differences in different device stack. (c) A potential profile along the white arrow in (b).

The compatibility of the current holography setup with the Protochips Aduro 300 system is another concern before running the actual experiments. When the specimens are attached to the E-chip, one cannot rotate the specimens unlike the conventional FIB lift-

out specimens attached to the Omniprobe Cu grids in Figure 6.9 and 6.10. As mentioned above, the SiO_2 layer is used for the reference wave and it has only limited space, and because of this, the orientation of the specimen with respect to the bi-prism must be adjusted to obtain the electron hologram. In other words, the specimen and the bi-prism have to be aligned with respect to each other in a way that the bi-prism bisects the active device region and the SiO_2 layer as seen in Figure 6.10(a).

In order to accomplish this, FIB lift-out specimens were prepared and attached to the Protochips electrical E-chip by using both Ga^+ FIB and plasma FIB (see Figure 6.11).

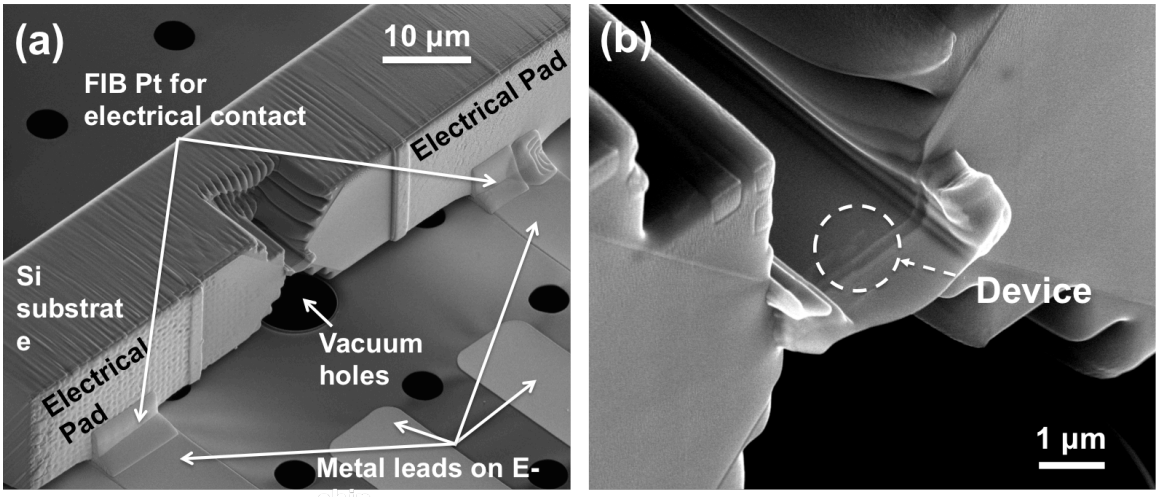

Figure 6.11 (a) SEM micrograph of the FIB lift-out specimen of $HfAlO_x$-based RRAM device. (b) Magnified view near the largest vacuum hole showing the active device region.

PFIB enabled to fabricate a very large sized lift-out specimen (~100×15×40 μm^3) within a reasonable time (few hours). By making this large device, I intended to avoid any FIB damage to the active device region during the sample preparation process, such as re-

deposition of sputtered species and spill over of the Pt deposition. The specimens were thinned down to ~100 nm only near the active device region (window thinning) by using Ga^+ FIB as shown in Figure 6.11(b). Figure 6.12 shows a BF TEM image of the active device region defined by overlap of the top and bottom electrodes. Note that the two TiN top and bottom electrodes extend to the electrical pads in Figure 6.11(a).

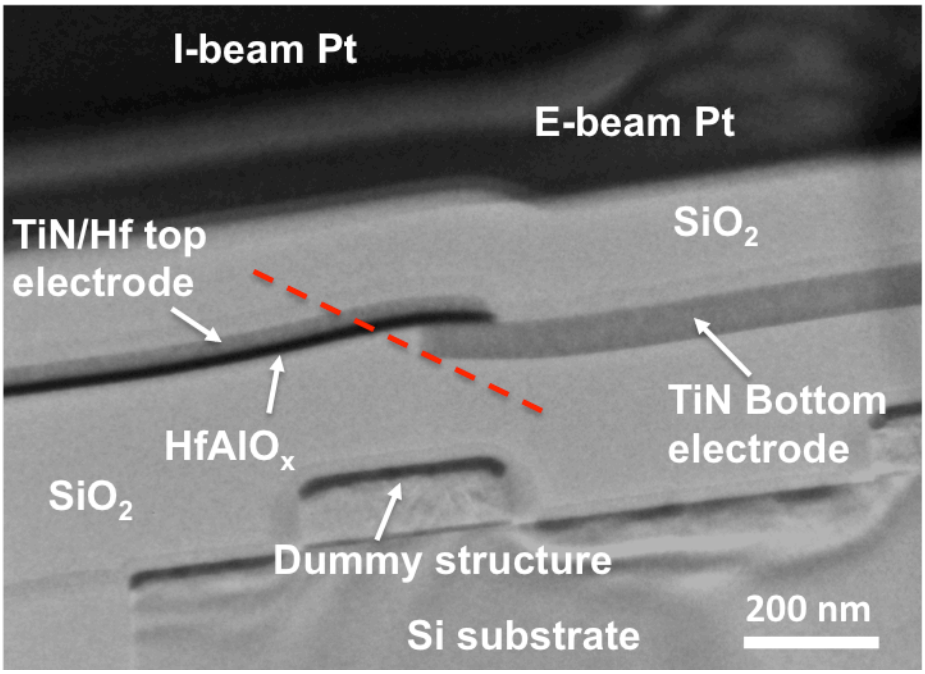

Figure 6.12 Bright field TEM image of the active device region showing the multiple device stacks. The active device region is where the top and bottom electrodes are overlapped. The red dotted line indicates the bi-prism location.

Similar electron holography experiments were conducted at ASU for the specimens mounted on the Protochips electrical E-chip (see Figure 6.11) using FEI Titan at 300 keV. The bi-prism location is marked as a red dashed line in Figure 6.12. Figure 6.13 shows the electron hologram and the extracted phase map in the active device region.

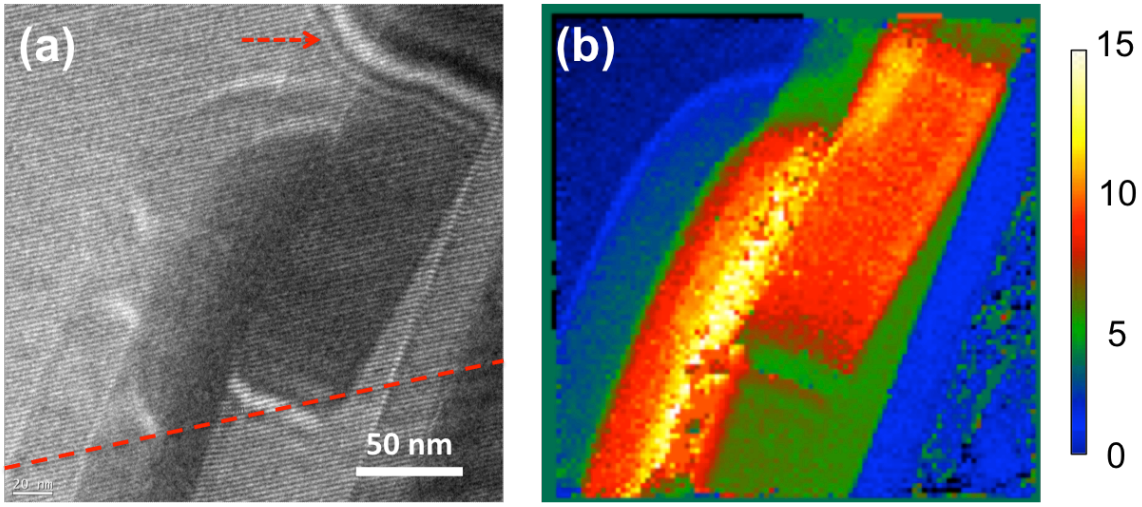

Figure 6.13 (a) The obtained electron hologram and (b) the extracted phase map of the specimen attached to the Protochips E-chip. The bi-prism location is marked with a red dotted line in (a). The color bar in (b) indicates the relative phase difference.

Similar to the previous results in Figure 6.10, the electron hologram was successfully produced for the specimen mounted on the E-chip. The SiO_2 layer shows 0 phase change and the maximum phase change is 15 at the Hf layer as shown in Figure 6.13(b). It appears that the phase resolution in $HfAlO_x$ layer is much poorer than the one in Figure 6.10. This is presumably because the specimen was thicker (~130 nm) than the previous sample. Similarly, one cannot clearly observe the $HfAlO_x$ layer in the BF TEM image as well in Figure 6.12. The area of the SiO_2 layer where the reference wave penetrates has very limited space due to the presence of dummy structures below the device as seen in Figure 6.12, and thereby when the hologram is formed (superposition of the object and reference wave by the bi-prism) the dummy structure can also be observed in the hologram in Figure 6.13(a) that is marked with a red dotted arrow.

The results confirm that the specimen mounted on a E-chip can be used for the electron holography experiments. In order to enhance the phase resolution, one can reduce the specimen thickness below 100 nm and use a vacuum reference wave instead of the SiO_2 by carefully removing the SiO_2 passivation and Pt capping layers with the FIB.

For the future work, the cross-square RRAM devices (80×80 nm^2) could be programmed to ON state and OFF state by applying quasi-DC sweeps. The expected SET and RESET voltages are ~ ±2.5 V. Once the devices are programmed, FIB lift-out specimens could be fabricated and attached onto the E-chips by FIB similar to the one in Figure 6.11. Then, the *in situ* biasing electron holography could be conducted with the prepared specimens (both ON and OFF state) to test the hypothesis (electrostatic potential distributions in the ON and OFF state devices as seen in Figure 6.7). It is important to note that the constant bias should be lower than the SET and RESET voltages (±2.5 V) to avoid a resistance state change.

7 Conclusion

Oxygen vacancy motion and agglomeration into conductive phases are often associated with resistive switching in RRAM devices. Extensive *ex situ* analysis has led to propose switching mechanisms that invoke defect formation/motion, but direct observations of defect evolution associated with switching are still lacking. Thus, I have reported direct monitoring of oxygen vacancy motion using observation of Wadsley defect (crystallographic shear faults) formation and evolution with *in situ* electrical testing of TiO_2-based devices inside the transmission electron microscope (TEM). This method enabled me to monitor structural transformations that accompany resistive switching. A model single-crystal TiO_2-based devices were used for this study. I have presented the first demonstration of electrical testing of the model device while observing oxygen vacancy migration under a TEM in real-time. This serves as the direct evidence of vacancy migration in the same device, at a specific spatial location during concurrent bias and TEM imaging. Resistive switching of the single-crystal TiO_2 devices was associated with Wadsley defects initiated from the TiO_2/TiN interface and observed to connect and disconnect during the SET and RESET processes within a 50 nm defect-free zone. The mechanism of resistance changes observed in the model TiO_2 device is unclear at this point. In other words, neither the filamentary nor the interfacial switching mechanisms describes the observed phenomena. Further extensive studies are necessary to fully correlate switching behaviors to defect dynamics in TiO_2.

The fundamental defect dynamics essential for resistive switching (creation, migration, reversible coalescence / dissociation of oxygen vacancy) with decoupling of temperature

effect on the defect dynamics was studied using an *in situ* biasing TEM approach. An appropriate biasing range was applied to a model single-crystal TiO_2 device. Gradual concurrent extension and contraction of Wadsley defects instead of abrupt changes in the microstructure observed in previous works. A finite element modeling estimated the peak temperature excursion of ~140 °C which is significantly lower than the TiO_2 thermal reduction temperature (~ 1000 °C). Two defect zones facing each other were created under maximum voltage of -1.35 V and +1.15V. Growth of the top defect zone was observed as well as dissociation of the bottom defect zone during negative bias and exactly the opposite behavior during positive bias. The observed defect motion implies that the relatively low value of electric field caused creation, drift, and coalescence of oxygen vacancies (~ 1×10^4 V/cm). A 10 mV *Read* pulse applied to a 10 nm thick oxide layer would induce fields well in excess of the fields used in my experiments. Therefore, the defect evolution reported here could be important under *Read Disturb* voltages for actual nano-scale resistive switching devices. Another important observation was residual dislocation loops (coffee bean-like contrast) near the end of the Wadsley defects. These dislocation loops represent incomplete retraction of the Wadsley defects caused by the field reversal, thus indicating a possible mechanism for RESET failures after endurance cycling.

Since resistive switching phenomena are directly connected to the characteristics of conductive filaments, estimating the filament size is critical and has been an active research topic. Knowing the filament size, one can have improved insight into controlling switching and can engineer superior devices. The important consequence of the filament

size is the filament temperature generated during switching (device scaling suggests the filament sizes are below 10 nm). In order to estimate the filament temperature reliably, controlling the current compliance is very critical. Thus, in my study, the devices were programmed with a low current compliance achieved by on-chip transistors and resistors as ballast to keep the dissipated power of 10 - 20 μW are likely to form a much smaller filament. And combining novel transient thermometry and high-resolution transmission electron microscopy (HRTEM), the conductive filament size, and the role of nanoscale temperature excursions were investigated. Using transient thermometry and HRTEM analysis, the filament size of ~1 nm was estimated with 7-15 nm crystalline region embedded in an amorphous matrix. Temperature excursions exceed 1600 K at the filament core and 850 K in the < 20 nm diameter hot zone. This makes the HRTEM analysis, thermometry and finite element simulation self-consistent and a powerful tool in understanding the temperature excursions during switching.

In order to further understand the filament configuration and its chemical nature, a plan-view EELS and *in situ* biasing electron holography experiments have been proposed and the plan for experiments have been developed. The on-going research combined with the previous results in this thesis will shed light on understanding the fundamental switching mechanisms in resistive switches.

Appendix A. HfO_x microstructure: Pristine vs. Switched Devices

As a control specimen, the microstructure of the pristine (unstressed) HfO_x-based device was characterized by HRTEM. Figure A.1 shows a HRTEM micrograph of a pristine HfO_x device (85×85 nm^2). Since the device was cut along the TiN (TE) of the crossbar device, the TE appears much longer in width than the TiN (BE). The region where the functional layer lies between the two electrodes is the active device area (~65 nm). The difference between the nominal (85 nm) and the actual device (~65 nm) size is presumably due to an etching process during device fabrication. The thickness of each layer was confirmed to be close to the nominal values. The two TiN electrodes are polycrystalline and exhibit a microstructural morphology consistent with columnar growth. The HfO_x functional layer exhibits slightly lighter contrast than the Hf oxygen getter layer by BF TEM because of the atomic mass/density difference. The roughness of the interface is about 1 nm. Recesses are observed at both edges of the active device area, which were likely created during an etching step during the device fabrication process. The lightest contrast surrounding the TiN BE is the SiO_2 passivation layer with speckle contrast indicative of deposited Ga^+ ions from the FIB specimen preparation process. Note that the speckle contrast is not seen in the device area and does not affect phase contrast imaging for HRTEM of the device layers.

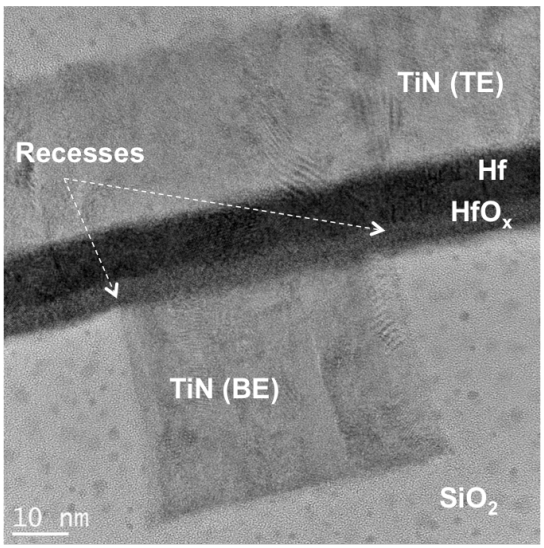

Figure A.1 HRTEM micrograph of the pristine HfO_x device.

Magnified views of the active device region are shown in Figure A.2. Figure A.2(a, b) and Figure A.2(c, d) are focusing series (changes in objective lens strength at the same field of view) of the left corner and right corner of the device, respectively (Δf=0 is assumed at the Gaussian focus[72]). The recesses in the bottom-left corner in Figure A.2(a, b) and in the bottom-left corner in Figure A.2(c, d) provide landmarks to confirm that the images were recorded at the same location. The TiN(BE)/HfO_x/Hf/TiN(TE) stacks from the bottom are seen and the lightest contrast near the recesses is SiO_2 passivation layer as seen in Figure A.2(a). As indicated by white arrows, multiple lattice fringes with different d-spacings are observed throughout the HfO_x layer. The crystallites are surrounded by an amorphous matrix with size from 3 to 10 nm. Thus, the microstructure of the pristine HfO_x is a mixture of polycrystalline and amorphous material. From the measured d-spacing, it can be deduced that the crystalline features correspond to a tetragonal HfO_x phase. The formation of tetragonal HfO_2 during annealing of HfO_2 thin films has been

previously reported.[125] It is seen that the both Hf and TiN layers are polycrystalline and their lattice fringes are marked in Figure A.2(d). The fringes of 0.26 nm spacing in Figure A.2(a) appear to be continuous across the HfO_x/Hf/TiN(TE) layers, which confirms that the as-deposited HfO_x layer contains crystallites. It was reported that the crystallization of HfO_x does not affect its resistivity or the leakage current in MIM structures.[125,126]

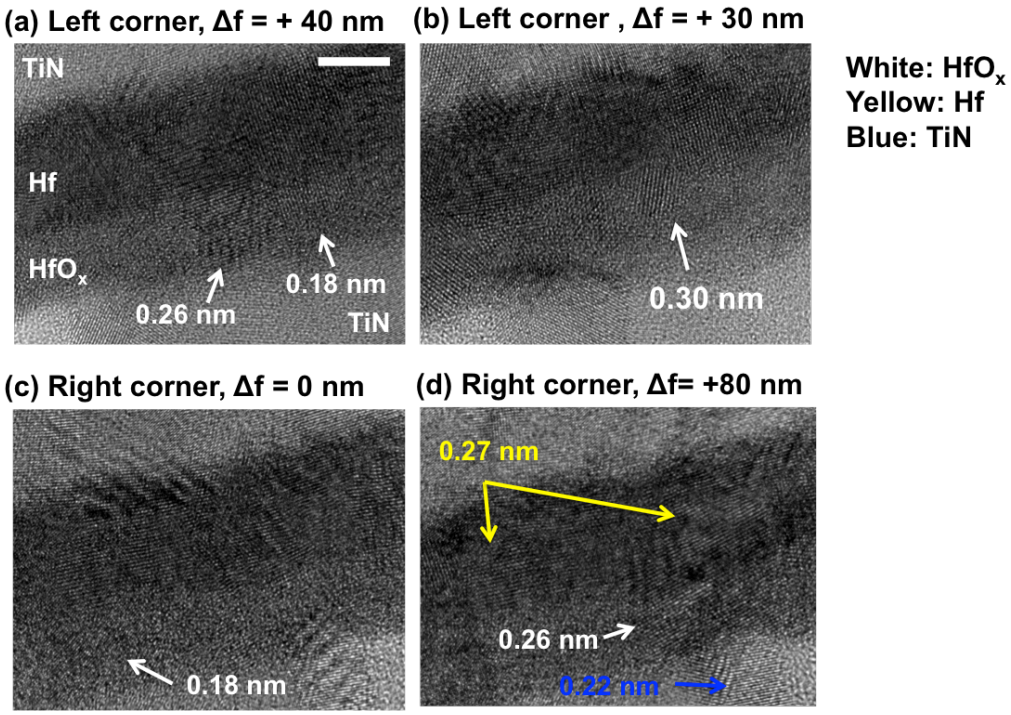

Figure A.2 Magnified views of the pristine HfO_x functional layers of the device in Figure A.1 where (a, b) the left and (c, d) right corners are imaged under different focusing conditions. The recesses at each corner indicate the images were obtained at the same locations. The scale bar is 5 nm.

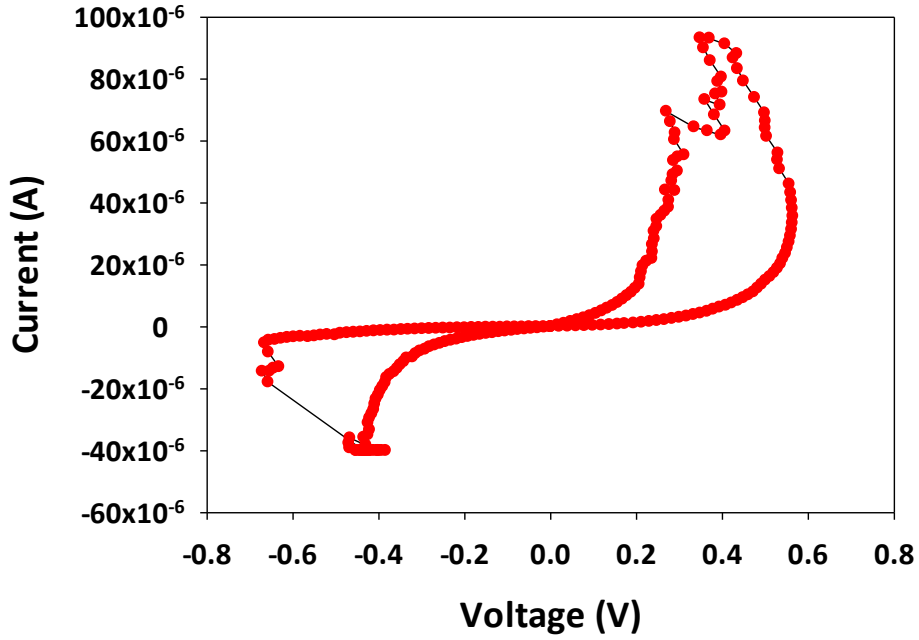

Figure A.3 A quasi-DC switching *I-V* curve of the HfO_x device.

Figure A.3 is the switching *I-V* curve of HfO_x device. Both SET and RESET transitions are clearly observed. The SET and RESET voltages are measured to be 0.58 V and 0.68 V, respectively. The maximum power dissipation is 27 μW. Figure A.4(a) shows the microstructure of the switched HfO_x device (85×85 nm^2) at a low magnification. Similar to the pristine specimen (Figure A.1), all the layers are visible with layer thicknesses close to expected values. Recesses at the both edges of the active device area are marked with dashed arrows. The inset is a HRTEM image of a different specimen cut along the BE showing a recessed region in BE due to an etching process during device fabrication. The lighter contrast between the HfO_x and the TiN (BE) is part of the TiN, originated from the recessed region as seen in inset. Since the switched HfO_x specimen is cut along TE and the specimen is thicker than the active device area, the slightly thinner TiN layer

exhibits lighter contrast compared to rest of the TiN. Note that the thinner TiN indicates the specimen contains the entire active device area.

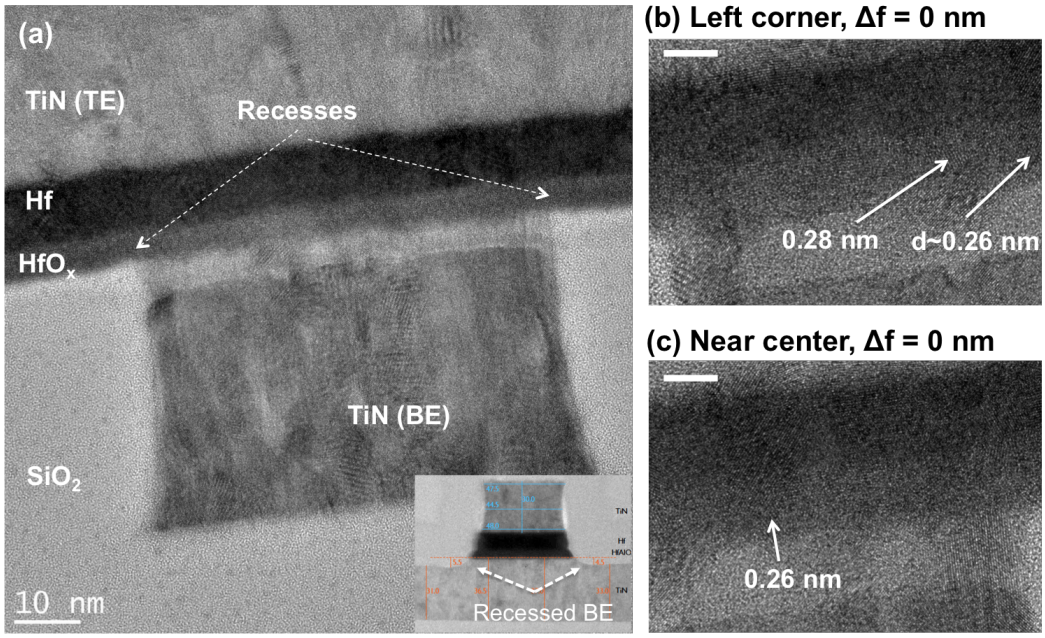

Figure A.4 HR TEM images of the switched HfO_x device. (a) Low magnification micrograph showing the entire device stack of TiN(TE)/Hf/HfO_x/TiN(BE). High magnification images of (b) the left corner and (b) the near center. Both the scale bars in (b, c) are 5 nm.

Comparing HRTEM results for the switched and pristine device indicate little difference in the structural features in the functional HfO_x layers. Figure A.4(b) and (c) are magnified views of the switched HfO_x device at the left corner and near the device center. Microstructure of the switched device is quite similar to the one in the pristine device. Except the lighter contrast of BE TiN (thinner TiN area), the device stack of TiN(BE)/HfO_x/Hf/TiN(TE) and the SiO_2 passivation layer are similar to the pristine

specimen. The roughness is also about 1nm. Multiple fringe patterns are observed in the HfO_x layer whose d-spacings correspond to tetragonal HfO_2. The size of the crystalline features are about 5-10 nm. Similar to the pristine specimen, continuous fringes across the HfO_x/Hf layers were observed, with one example case denoted by "0.26 nm" in Figure A.4(c). Only one focusing condition was used for HRTEM of the switched specimen, so more crystalline features may be present in other locations of the HfO_x layer. Comparing the microstructure of the pristine and the switched HfO_x device indicates no obvious structural differences; the measured d-spacing values are more or less identical (tetragonal HfO_2) and no additional secondary phases are observed. Interfaces of the layers appear to be the same as well.

References

[1] *International Technology Roadmap For Semiconductors 2011 Edition: Emerging Research Devices (ERD)*; 2011.

[2] P. C. Lacaze, J.-C. Lacroix, *Non-volatie Memories*; ISTE Ltd and John Wilely & Son, Inc., 2014.

[3] M.-J. Lee, C. B. Lee, D. Lee, S. R. Lee, M. Chang, J. H. Hur, Y.-B. Kim, C.-J. Kim, D. H. Seo, S. Seo, U.-I. Chung, I.-K. Yoo, K. Kim, *Nat. Mater.* **2011**, *10*, 625.

[4] N. Setter, D. Damjanovic, L. Eng, G. Fox, S. Gevorgian, S. Hong, A. Kingon, H. Kohlstedt, N. Y. Park, G. B. Stephenson, I. Stolitchnov, A. K. Taganstev, D. V. Taylor, T. Yamada, S. Streiffer, *J. Appl. Phys.* **2006**, *100*, 51606.

[5] H. Liu, D. Bedau, D. Backes, J. a. Katine, J. Langer, a. D. Kent, *Appl. Phys. Lett.* **2010**, *97*, 242510.

[6] H. F. Hamann, M. O'Boyle, Y. C. Martin, M. Rooks, H. K. Wickramasinghe, *Nat. Mater.* **2006**, *5*, 383.

[7] R. Waser, M. Aono, *Nat. Mater.* **2007**, *6*, 833.

[8] D. S. Jeong, R. Thomas, R. S. Katiyar, J. F. Scott, H. Kohlstedt, a Petraru, C. S. Hwang, *Rep. Prog. Phys.* **2012**, *75*, 76502.

[9] H.-S. P. Wong, H.-Y. Lee, S. Yu, Y.-S. Chen, Y. Wu, P.-S. Chen, B. Lee, F. T. Chen, M.-J. Tsai, *Proc. IEEE* **2012**, *100*, 1951.

[10] *International Technology Roadmap For Semiconductors 2010 Edition: Emerging*

Research Devices (ERD); 2010.

[11] A. A. Sharma, M. Noman, M. Abdelmoula, M. Skowronski, J. A. Bain, *Adv. Funct. Mater.* **2014**, *24*, 5522.

[12] K. M. Kim, D. S. Jeong, C. S. Hwang, *Nanotechnology* **2011**, *22*, 254002.

[13] R. Waser, R. Dittmann, G. Staikov, K. Szot, *Adv. Mater.* **2009**, *21*, 2632.

[14] K. Szot, M. Rogala, W. Speier, Z. Klusek, A. Besmehn, R. Waser, *Nanotechnology* **2011**, *22*, 254001.

[15] F. Nardi, S. Member, S. Larentis, S. Balatti, D. C. Gilmer, D. Ielmini, S. Member, *IEEE Trans. Electron Devices* **2012**, *59*, 2461.

[16] A. Fantini, D. J. Wouters, R. Degraeve, L. Goux, L. Pantisano, G. Kar, Y. Chen, B. Govoreanu, J. A. Kittl, L. Altimime, M. Jurczak, *Int. Mem. Work.* **2012**, 1.

[17] J. J. Yang, M. D. Pickett, X. Li, D. A. A. Ohlberg, D. R. Stewart, R. S. Williams, *Nat. Nanotechnol.* **2008**, *3*, 429.

[18] J. Borghetti, D. B. Strukov, M. D. Pickett, J. J. Yang, D. R. Stewart, R. S. Williams, *J. Appl. Phys.* **2009**, *106*, 124504.

[19] S. Menzel, M. Waters, A. Marchewka, U. Böttger, R. Dittmann, R. Waser, *Adv. Funct. Mater.* **2011**, *21*, 4487.

[20] R. Degraeve, A. Fantini, Y. Y. Chen, S. Clima, B. Govoreanu, L. Goux, D. J. Wouters, P. Roussel, G. S. Kar, G. Pourtois, S. Cosemans, G. Groeseneken, M. Jurczak, L. Altimime, *2012 IEEE Int. Integr. Reliab. Work. Final Rep.* **2012**, 3.

[21] S. Larentis, F. Nardi, S. Balatti, D. C. Gilmer, D. Ielmini, *IEEE Trans. Electron*

Devices **2012**, *59*, 2468.

[22] B. Govoreanu, S. Clima, I. P. Radu, Y. Chen, D. J. Wouters, M. Jurczak, *IEEE Trans. Electron Devices* **2013**, *60*, 2471.

[23] M. Noman, W. Jiang, P. A. Salvador, M. Skowronski, J. A. Bain, *Appl. Phys. A* **2011**, *102*, 877.

[24] D. S. Jeong, H. Schroeder, U. Breuer, R. Waser, *J. Appl. Phys.* **2008**, *104*, 123716.

[25] K. M. Kim, B. J. Choi, Y. C. Shin, S. Choi, C. S. Hwang, *Appl. Phys. Lett.* **2007**, *91*, 12907.

[26] D. Ielmini, R. Waser, *Resistive Switching: From Fundamentals of Nanoionic Redox Processes to Memrisitive Device Applications*; Wiley-VCH, 2016.

[27] J. Blanc, D. L. Staebler, *Phys. Rev. B* **1971**, *4*, 3548.

[28] W. Jiang, M. Noman, Y. M. Lu, J. A. Bain, P. A. Salvador, M. Skowronski, *J. Appl. Phys.* **2011**, *110*, 34509.

[29] D.-H. Kwon, K. M. Kim, J. H. Jang, J. M. Jeon, M. H. Lee, G. H. Kim, X.-S. Li, G.-S. Park, B. Lee, S. Han, M. Kim, C. S. Hwang, *Nat. Nanotechnol.* **2010**, *5*, 148.

[30] F. Miao, J. P. Strachan, J. J. Yang, M.-X. Zhang, I. Goldfarb, A. C. Torrezan, P. Eschbach, R. D. Kelley, G. Medeiros-Ribeiro, R. S. Williams, *Adv. Mater.* **2011**, *23*, 5633.

[31] J. P. Strachan, D. B. Strukov, J. Borghetti, J. J. Yang, G. Medeiros-Ribeiro, R. S. Williams, *Nanotechnology* **2011**, *22*, 254015.

[32] G.-S. Park, Y. B. Kim, S. Y. Park, X. S. Li, S. Heo, M.-J. Lee, M. Chang, J. H.

Kwon, M. Kim, U.-I. Chung, R. Dittmann, R. Waser, K. Kim, *Nat. Commun.* **2013**, *4*, 2382.

[33] E. Yalon, A. A. Sharma, M. Skowronski, J. A. Bain, D. Ritter, I. V Karpov, *IEEE Trans. Electron Devices* **2015**, *62*, 2972.

[34] A. Marchewka, D. Cooper, C. Lenser, S. Menzel, H. Du, R. Dittmann, R. E. Dunin-Borkowski, R. Waser, *Sci. Rep.* **2014**, *4*.

[35] N. Ikarashi, H. Takeda, K. Yako, M. Hane, *Appl. Phys. Lett.* **2012**, *100*, 1.

[36] B. J. Choi, D. S. Jeong, S. K. Kim, C. Rohde, S. Choi, J. H. Oh, H. J. Kim, C. S. Hwang, K. Szot, R. Waser, B. Reichenberg, S. Tiedke, *J. Appl. Phys.* **2005**, *98*, 33715.

[37] K. Szot, W. Speier, G. Bihlmayer, R. Waser, *Nat. Mater.* **2006**, *5*, 312.

[38] R. J. Kamaladasa, M. Noman, W. Chen, P. A. Salvador, J. A. Bain, M. Skowronski, Y. N. Picard, *J. Appl. Phys.* **2013**, *113*, 234510.

[39] S. Seo, M. J. Lee, D. H. Seo, E. J. Jeoung, D.-S. Suh, Y. S. Joung, I. K. Yoo, I. R. Hwang, S. H. Kim, I. S. Byun, J.-S. Kim, J. S. Choi, B. H. Park, *Appl. Phys. Lett.* **2004**, *85*, 5655.

[40] J. Chen, C. Hsin, C. Huang, C. Chiu, Y. Huang, *Nano Lett.* **2013**, *13*, 3671.

[41] A. Sawa, *Mater. Today* **2008**, *11*, 28.

[42] I. G. Baek, M. S. Lee, S. Seo, M. J. Lee, D. H. Seo, D. Suh, J. C. Park, S. O. Park, H. S. Kim, I. K. Yoo, U. Chung, J. T. Moon, *IEDM Tech. Dig.* **2004**, 587.

[43] B. Govoreanu, G. S. Kar, Y. Chen, V. Paraschiv, S. Kubicek, A. Fantini, I. P.

Radu, L. Goux, S. Clima, R. Degraeve, N. Jossart, O. Richard, T. Vandeweyer, K. Seo, P. Hendrickx, G. Pourtois, H. Bender, L. Altimime, D. J. Wouters, J. A. Kittl, M. Jurczak, B.- Leuven, K. U. Leuven, In *International Electron Devices Meeting*; IEEE, 2011; pp. 729–732.

[44] J. P. Strachan, J. Joshua Yang, R. Münstermann, A. Scholl, G. Medeiros-Ribeiro, D. R. Stewart, R. Stanley Williams, *Nanotechnology* **2009**, *20*, 485701.

[45] F. Miao, J. J. Yang, J. P. Strachan, D. Stewart, R. S. Williams, C. N. Lau, *Appl. Phys. Lett.* **2009**, *95*, 113503.

[46] U. Celano, Y. Yin Chen, D. J. Wouters, G. Groeseneken, M. Jurczak, W. Vandervorst, *Appl. Phys. Lett.* **2013**, *102*, 121602.

[47] J. P. Strachan, M. D. Pickett, J. J. Yang, S. Aloni, A. L. David Kilcoyne, G. Medeiros-Ribeiro, R. Stanley Williams, *Adv. Mater.* **2010**, *22*, 3573.

[48] J. Joshua Yang, F. Miao, M. D. Pickett, D. A. A. Ohlberg, D. R. Stewart, C. N. Lau, R. S. Williams, *Nanotechnology* **2009**, *20*, 215201.

[49] G. Sassine, S. La Barbera, N. Najjari, M. Minvielle, C. Dubourdieu, F. Alibart, *J. Vac. Sci. Technol. B, Nanotechnol. Microelectron. Mater. Process. Meas. Phenom.* **2016**, *34*, 12202.

[50] Y.-F. Wang, Y.-C. Lin, I.-T. Wang, T.-P. Lin, T.-H. Hou, *Sci. Rep.* **2015**, *5*, 10150.

[51] W. Lee, G. Jo, S. Lee, J. Park, M. Jo, J. Lee, S. Jung, S. Kim, J. Shin, S. Park, T. Lee, H. Hwang, *Appl. Phys. Lett.* **2011**, *98*, 32105.

[52] A. Sawa, T. Fujii, M. Kawasaki, Y. Tokura, *Appl. Phys. Lett.* **2006**, *88*, 232112.

[53] H. Sim, H. Choi, D. Lee, M. Chang, D. Choi, Y. Son, E.-H. Lee, W. Kim, Y. Park,

I.-K. Yoo, H. Hwang, In *IEDM Tech. Dig.*; 1005; pp. 758–761.

[54] A. Sawa, T. Fujii, M. Kawasaki, Y. Tokura, *Appl. Phys. Lett.* **2004**, *85*, 4073.

[55] C. Park, Y. Seo, J. Jung, D.-W. Kim, *J. Appl. Phys.* **2008**, *103*, 54106.

[56] J. Norpoth, S. Mildner, M. Scherff, J. Hoffmann, C. Jooss, *Nanoscale* **2014**, *6*, 9852.

[57] W.-Y. Chang, Y.-C. Lai, T.-B. Wu, S.-F. Wang, F. Chen, M.-J. Tsai, *Appl. Phys. Lett.* **2008**, *92*, 22110.

[58] H. Schroeder, V. V. Zhirnov, R. K. Cavin, R. Waser, *J. Appl. Phys.* **2010**, *107*, 54517.

[59] D. B. Strukov, R. S. Williams, *Appl. Phys. A Mater. Sci. Process.* **2009**, *94*, 515.

[60] J. J. Yang, D. B. Strukov, D. R. Stewart, *Nat. Nanotechnol.* **2013**, *8*, 13.

[61] L. A. Bursill, B. G. Hyde, O. Terasaki, D. Watanabe, *Philos. Mag.* **1969**, *20*, 347.

[62] S. Andersson, A. D. Wadsley, *Nature* **1966**, 581.

[63] J. Van Landuyt, *J. Phys. Colloq.* **1974**, *35*, C7 53.

[64] P. Kofstad, *Oxid. Met.* **1995**, *44*, 3.

[65] L. A. Bursill, B. G. Hyde, *Prog. Solid State Chem.* **1972**, *7*, 177.

[66] M. Bowker, R. A. Bennett, *J. Phys. Condens. Matter* **2010**, *22*, 59801.

[67] R. J. Kamaladasa, Electron microscopy investigation of extended defect influence on resistive switching in strontium titanate and rutile titania, Carnegie Mellon University, 2013.

[68] S. Privitera, G. Bersuker, B. Butcher, A. Kalantarian, S. Lombardo, C. Bongiorno,

R. Geer, D. C. Gilmer, P. D. Kirsch, *Microelectron. Eng.* **2013**, *109*, 75.

[69] U. Celano, L. Goux, R. Degraeve, A. Fantini, O. Richard, H. Bender, M. Jurczak, W. Vandervorst, *Nano Lett.* **2015**, *15*, 7970.

[70] R. J. Kamaladasa, A. A. Sharma, Y.-T. Lai, W. Chen, P. A. Salvador, J. A. Bain, M. Skowronski, Y. N. Picard, *Microsc. Microanal.* **2015**, *21*, 140.

[71] Y. M. Lu, M. Noman, W. Chen, P. A. Salvador, J. A. Bain, M. Skowronski, *J. Phys. D. Appl. Phys.* **2012**, *45*, 395101.

[72] D. B. Williams, C. B. Carter, *Transmission Electron Microscopy*; 2nd ed.; Springer, 2009.

[73] J. Kwon, A. a. Sharma, J. a. Bain, Y. N. Picard, M. Skowronski, *Adv. Funct. Mater.* **2015**, *25*, 2876.

[74] R. Waser, T. Baiatu, Karl-Heinz Hardtl, *J. Am. Ceram. Soc.* **1990**, *73*, 1654.

[75] S. Rodewald, J. Fleig, J. Maier, *J. Am. Ceram. Soc.* **2000**, *83*, 1969.

[76] M. Wojtyniak, K. Szot, R. Wrzalik, C. Rodenbücher, G. Roth, R. Waser, *J. Appl. Phys.* **2013**, *113*, 83713.

[77] W. D. Ohlsen, O. W. Johnson, *J. Appl. Phys.* **1973**, *44*, 1973.

[78] J. J. Yang, J. P. Strachan, Q. Xia, D. A. A. Ohlberg, P. J. Kuekes, R. D. Kelley, W. F. Stickle, D. R. Stewart, G. Medeiros-Ribeiro, R. S. Williams, *Adv. Mater.* **2010**, *22*, 4034.

[79] K. M. Kim, S. J. Song, G. H. Kim, J. Y. Seok, M. H. Lee, J. H. Yoon, J. Park, C. S. Hwang, *Adv. Funct. Mater.* **2011**, *21*, 1587.

[80] S. Andersson, B. Collén, G. Kruuse, U. Kuylenstierna, A. Magnéli, H. Pestmalis, S. Åsbrink, *Acta Chem. Scand.* **1957**, *11*, 1653.

[81] L. A. Bursill, B. G. Hyde, *Philos. Mag.* **1971**, *23*, 3.

[82] M. G. Blanchin, P. Faisant, C. Picard, M. Ezzo, G. Fontaine, *Phys. Status Solidi* **1980**, *60*, 357.

[83] M. G. Blanchin, L. A. Bursill, *Phys. Status Solidi* **1984**, *86*, 491.

[84] L. A. Bursill, S. G. Jun, D. J. Smith, M. G. Blanchin, *Ultramicroscopy* **1984**, *13*, 191.

[85] J. Kwon, A. A. Sharma, J. A. Bain, Y. N. Picard, M. Skowronski, In *Reliability Physics Symposium, 2014 IEEE International*; IEEE: Waikoloa, HI, 2014; p. 5E.5.1-5E.5.5.

[86] E. Yagi, R. R. Hasiguti, M. Aono, *Phys. Rev. B* **1996**, *54*, 7945.

[87] L. Pastewka, R. Salzer, A. Graff, F. Altmann, M. Moseler, *Nucl. Instruments Methods Phys. Res. Sect. B Beam Interact. with Mater. Atoms* **2009**, *267*, 3072.

[88] L. A. Bursill, B. G. Hyde, D. K. Philp, *Philos. Mag.* **1971**, *23*, 1501.

[89] Y. Meng Lu, M. Noman, Y. N. Picard, J. A. Bain, P. A. Salvador, M. Skowronski, *J. Appl. Phys.* **2013**, *113*, 163703.

[90] H. Sawatari, E. Iguchi, R. J. D. Tilley, *J. Phys. Chem. Solids* **1982**, *43*, 1147.

[91] J. S. Anderson, B. G. Hyde, *J. Phys. Chem. Solids* **1967**, *28*, 1393.

[92] M. G. Blanchin, L. A. Bursill, *Phys. Status Solidi* **1984**, *86*, 101.

[93] T. Suzuki, M. Ueno, Y. Nishi, M. Fujimoto, *J. Am. Ceram. Soc.* **2001**, *84*, 200.

[94] Y.-C. Wu, C.-Y. Chen, H.-Y. Lu, D. E. Mc Cauley, M. S. H. Chu, *J. Am. Ceram. Soc.* **2006**, *89*, 2213.

[95] P. Philipp, L. Bischoff, B. Schmidt, *Nanotechnology* **2012**, *23*, 475304.

[96] S. Kim, S. Choi, W. Lu, *ACS Nano* **2014**, *8*, 2369.

[97] M. G. Blanchin, L. A. Bursill, D. J. Smith, *Proc. R. Soc. Lond. A. Math. Phys. Sci.* **1984**, *391*, 351.

[98] Y. Yang, P. Gao, L. Li, X. Pan, S. Tappertzhofen, S. Choi, R. Waser, I. Valov, W. D. Lu, *Nat. Commun.* **2014**, *5*, 4232.

[99] M. Asheghi, M. N. Touzelbaev, K. E. Goodson, Y. K. Leung, S. S. Wong, *J. Heat Transf.* **1998**, *120*, 30.

[100] J. Kwon, A. A. Sharma, C.-Y. M. Chen, A. Fantini, M. Jurczak, A. A. Herzing, J. A. Bain, Y. N. Picard, M. Skowronski, *ACS Appl. Mater. Interfaces* **2016**, *8*, 20176.

[101] E. P. Gusev, D. A. Buchanan, E. Cartier, A. Kumar, D. DiMaria, S. Guha, A. Callegari, S. Zafar, P. C. Jamison, D. A. Neumayer, M. Copel, M. A. Gribelyuk, H. Okorn-Schmidt, C. D'Emic, P. Kozlowski, K. Chan, N. Bojarczuk, L.-A. Ragnarsson, P. Ronsheim, K. Rim, R. J. Fleming, A. Mocuta, A. Ajmera, In *International Electron Devices Meeting*; 2001; p. 20.1.1-20.1.4.

[102] B. H. Lee, L. Kang, W.-J. Qi, R. Nieh, Y. Jeon, K. Onishi, J. C. Lee, In *International Electron Devices Meeting*; 1999; pp. 133–136.

[103] L. K. L. Kang, B. H. L. B. H. Lee, W.-J. Q. W.-J. Qi, Y. J. Y. Jeon, R. Nieh, S. Gopalan, K. Onishi, J. C. Lee, *IEEE Electron Device Lett.* **2000**, *21*, 181.

[104] R. Degraeve, A. Fantini, S. Clima, B. Govoreanu, L. Goux, Y. Y. Chen, D. J. Wouters, P. Roussel, G. S. Kar, G. Pourtois, S. Cosemans, J. A. Kittl, G. Groeseneken, M. Jurczak, L. Altimime, *2012 Symp. VLSI Technol.* **2012**, 75.

[105] Y. M. Kim, J. S. Lee, *J. Appl. Phys.* **2008**, *104*, 114115.

[106] C.-Y. Huang, J.-H. Jieng, W.-Y. Jang, C.-H. Lin, T.-Y. Tseng, *ECS Solid State Lett.* **2013**, *2*, P63.

[107] S. Yu, B. Gao, H. Dai, B. Sun, L. Liu, X. Liu, R. Han, J. Kang, B. Yu, *Electrochem. Solid-State Lett.* **2010**, *13*, H36.

[108] L. Zhao, H.-Y. Chen, S.-C. Wu, Z. Jiang, S. Yu, T.-H. Hou, H.-S. P. Wong, Y. Nishi, *Nanoscale* **2014**, *6*, 5698.

[109] Y. Y. Chen, R. Degraeve, S. Clima, B. Govoreanu, L. Goux, A. Fantini, G. S. Kar, G. Pourtois, G. Groeseneken, D. J. Wouters, M. Jurczak, In *IEDM*; 2012; pp. 10–13.

[110] C. Y. Chen, L. Goux, A. Fantini, A. Redolfi, S. Clima, R. Degraeve, Y. Y. Chen, G. Groeseneken, M. Jurczak, *IEDM* **2014**, 355.

[111] J. A. Strickland, L. Gordon, *Time-domain reflectometry measurements*; Tektronix, 1970.

[112] N. W. Ashcroft, N. D. Mermin, *Solid state physics*; Rinehart and Winston: New York, 1976.

[113] G. Chen, *Nanoscale Energy Transport and Conversion: A Parallel Treatment of Electrons, Molecules, Phonons, and Photons*; Oxford University Press, 2005.

[114] M. G. Burzo, P. L. Komarov, P. E. Raad, *IEEE Trans. Components Packag.*

Technol. **2003**, *26*, 80.

[115] A. Delan, M. Rennau, S. E. Schulz, T. Gessner, *Microelectron. Eng.* **2003**, *70*, 280.

[116] Z.-Z. Yuan, X.-D. Chen, B.-X. Wang, Y.-J. Wang, *J. Alloys Compd.* **2006**, *407*, 163.

[117] R. F. Egerton, *Reports Prog. Phys.* **2009**, *72*, 16502.

[118] Q. Wei, Z. Wu, K. Sun, F. A. Ponce, J. Hertkorn, F. Scholz, *Appl. Phys. Express* **2009**, *2*.

[119] F. A. Ponce, *Ann. Phys.* **2011**, *523*, 75.

[120] M. R. McCartney, D. J. Smith, *Annu. Rev. Mater. Res.* **2007**, *37*, 729.

[121] Y. Yao, C. Li, Z. L. Huo, M. Liu, C. X. Zhu, C. Z. Gu, X. F. Duan, Y. G. Wang, L. Gu, R. C. Yu, *Nat. Commun.* **2013**, *4*, 2764.

[122] H. Sasaki, S. Otomo, R. Minato, K. Yamamoto, T. Hirayama, *Microscopy* **2014**, 1.

[123] A. C. Twitchett, R. E. Dunin-Borkowski, R. J. Hallifax, R. F. Broom, P. A. Midgley, *J. Microsc.* **2004**, *214*, 287.

[124] J. Cai, F. A. Ponce, *J. Appl. Phys.* **2002**, *91*, 9856.

[125] H. Kim, P. C. McIntyre, K. C. Saraswat, *Appl. Phys. Lett.* **2003**, *82*, 106.

[126] H. Kim, A. Marshall, P. C. McIntyre, K. C. Saraswat, *Appl. Phys. Lett.* **2004**, *84*, 2064.